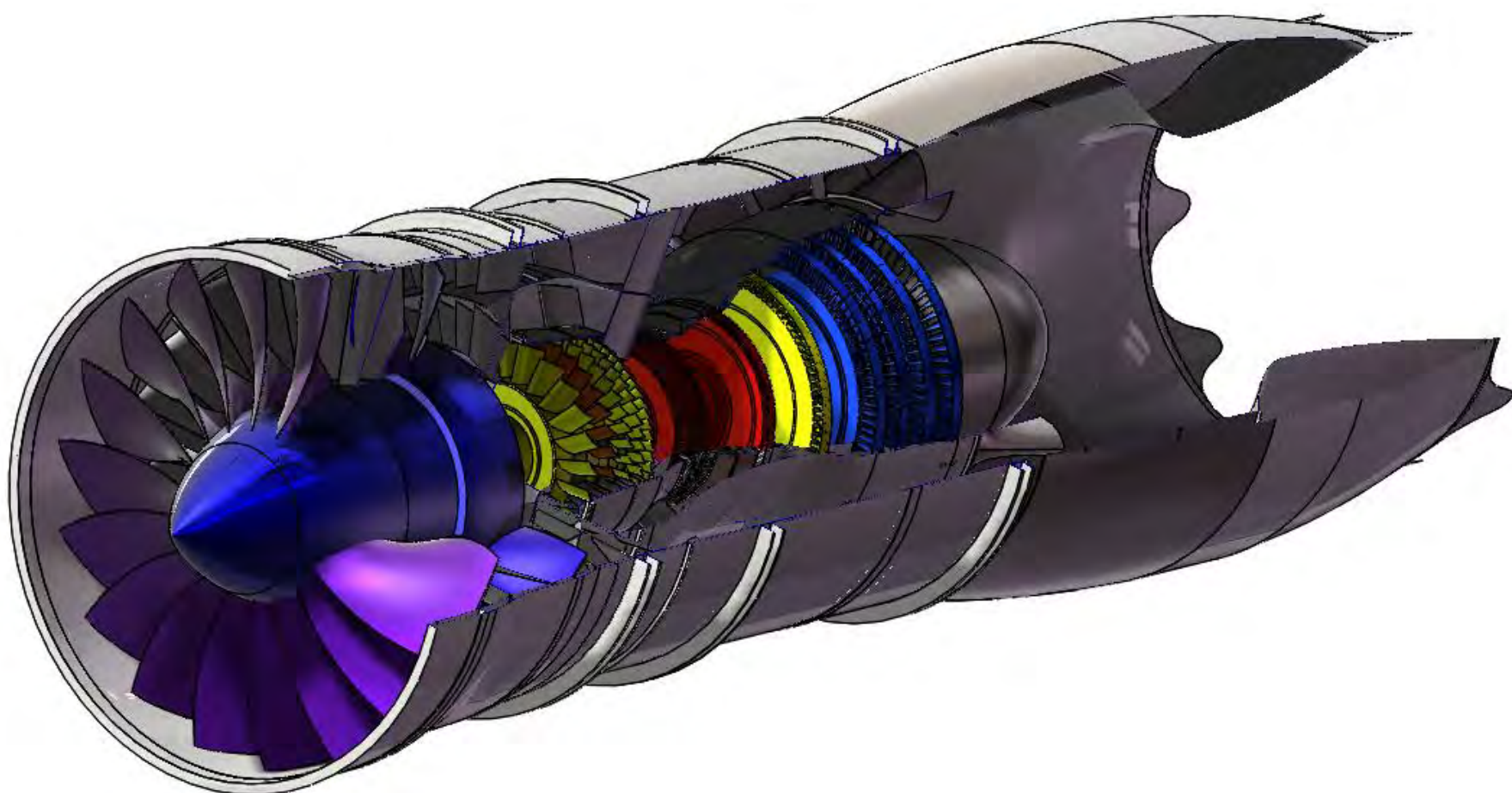# CJ-3000 Turbofan Engine Design Proposal

能源与动力工程学院
School of Energy and Power Engineering

Team Leader: Wang Yingjun

Team Member: Guo Minghao & Hu Yu

Faculty Advisor: Dr. Chen Min

SIGNATURE PAGE

Design Team:

Wang Yingjun:
#921794

Guo Mingha:
#921803

Hu Yu:
#921800

Acknowledgements

Abstract

The CJ 3000 is a triple-spool, mixed flow, middle bypass ratio turbofan engine designed as a candidate engine for the next generation supersonic transport. The performance of the CJ 3000 is shown to reach all requirements of the RFP.

The CJ 3000 offers great performance gains over the requirements and baseline engine, providing required thrust levels and a significantly lower TSFC for all four main flight conditions, less total engine weight, less fuel consumption and NOx emissions, and lower exhaust noise at takeoff. The practical and advanced technologies CJ 3000 employed are presented as follows.

Engine Component	Technologies Employed
Engine Configuration	Triple-Spool Engine
Inlet System	Two-Dimensional Mixed Compression Inlet
Transonic Fan	Polyimide Composites Fan Blades with Ti-6Al-4V Leading Edges
Internal-Pressure Compressor	TMMC Compressor Blades
High-Pressure Compressor	TMMC and Nickel-Base Super-Alloy Compressor Blades
Combustion Chamber	Hybrid Diffuser (Flat-Wall and Dump Diffuser)
	Lean Direct Injection (LDI) Combustor
	Convective Film Cooling via SiC/CMC with EBCs Liner
High-Pressure Turbine	SiC/CMC with EBCs Turbine Blades
Internal-Pressure Turbine	SiC/CMC with EBCs Turbine Blades
Low-Pressure Turbine	PST-TA and SiC/CMC with EBCs Turbine Blades
Mixer	Force Flow Lobed Mixer
Exhaust System	Variable Area Convergent-Divergent Nozzle
	Helmholtz Resonators and Sawtooth Trailing Edge Nozzle for Noise Suppression

The charts required by RFP will be shown next as parts of the content.

Table RFP-1 Performance Requirements Matrix

Parameter	Required Value	Design Value	Margin Relative to Requirement
Takeoff Thrust (lb)	64625	64754.3	0.20%
Max Thrust at Transonic Pinch Point (lb)	14278	14287.03	0.06%
TSFC at Transonic Pinch Point (lbm/lbf/hr)	0.950	0.8276	12.88%
Max Thrust at Supersonic Cruise (lb)	14685	15010.70	2.22%
TSFC at Supersonic Cruise (lbm/lbf/hr)	1.091	0.9874	9.50%
Fan Diameter (in)	98.6	94.5	8.10%
Bare Engine Weight (excl. inlet) (lb)	13000	11252	13.45%
Takeoff Exhaust Jet Velocity (ft/s)	1375	1327.92	3.42%
LTO NOx (g)	154	30.81	80.00%
Supersonic Cruise NOx (g/kg fuel)	5	1.27	74.60%

Table RFP-2 Compliance Matrix

General characteristics	
Wing area (ft^2)	3804.65
Max. take-off weight (lb)	312282
Takeoff-Thrust (lb)	2 ×56210
Design Thrust (lb)	2 ×64754 each @ SLS; 2 ×56582 each @ Hot Day
Performance	
Maximum speed (ft/s)	1742.76
Cruise speed (ft/s)	1549.11
Mission Fuel Burn (lb)	125983.18
Cruise TSFC (lbm/lbf/hr)	0.9132
Takeoff TSFC (lbm/lbf/hr)	0.4185
Engine Weight (lb)	11252
Fan Diameter (in)	94.5
Required Trade Studies	
Aircraft Constraint Diagram Page #	10
Engine Cycle Design Space Carpet Plots Page #	6
In-Depth Cycle Summary Page #	7
Final engine flow path (Page #)	48
Final cycle study using chosen cycle program (Page #)	III & IV
Detailed stage-by-stage turbomachinery design information and velocity triangles (page # for each component)	Fan: V, IPC: VI, HPC: VIII HPT: X, IPT: XI, LPT: XII
Detailed inlet and nozzle performance characteristics (Page #)	Inlet: 16, Nozzle: 35

Table RFP-3 Engine Summary Table

Summary Data	
Design MN	1.6
Design Altitude (ft)	52500
Design Fan Mass Flow (lb)	661.94
Design Gross Thrust (lb)	47872.9
Design Bypass Ratio	2.75
Design Net Thrust (lb)	15010.7
Design TSFC (lbm/lbf/hr)	0.9268
Design Overall Pressure Ratio	45
Design T4.1 (°R)	3282.5
Design Engine Pressure Ratio	2.13
Design Fan / LPC Pressure Ratio	2.44
Design Chargeable Cooling Flow (%@25)	3
Design Non-Chargeable Cooling Flow (%@25)	2
Design Adiabatic Efficiency for Each Turbine	HPT: 0.9200, IPT: 0.9200, LPT: 0.9200
Design Polytropic Efficiency for Each Compressor	Fan:0.8939, IPC: 0.9023, HPC: 0.8984
Design HP/IP/LP Shaft RPM	12000/7800/4000
Flow Station Data (List for Each Engine Component at Design Condition)	
Inflow	
Corrected Inflow	
Inflow Total Pressure	
Inflow Total Temperature	Refer to Appendix A: Simulation Validation of Engine by GasTurb 13
Inflow Fuel-air-Ratio	
Inflow Mach #	
Inflow Area	
Pressure Loss/Rise Across Component	
Additional Information	
Design HP/LP Shaft Off-take Power	100 hp @ HP
Design Customer Bleed Flow	1% @25

Table RFP-4 Required Detailed Stage and Component Information

Compressor		Turbine	
Lieblein Diffusion Factor		Zweifel Coefficient	
De Haller Number		AN^2	
Stage Pressure Ratio		Stage Pressure Ratio	
Work Coefficient		Work Coefficient	
Flow Coefficient		Flow Coefficient	
Hub-to-Tip Ratio		Hub-to-Tip Ratio	
Mean radius		Mean radius	
Number of Blades (Rotor & Stator)	Refer to Section 6: Aerodynamic Design of Turbomachinery System & 12.1.6 Blade Structure Analysis	Number of Blades (Rotor & Stator)	Refer to Section 6: Aerodynamic Design of Turbomachinery System & 12.1.6 Blade Structure Analysis
Aspect Ratio		Aspect Ratio	
Taper Ratio		Taper Ratio	
Tip Speed		Tip Speed	
Stagger Angle		Stagger Angle	
Velocity Triangles (hub, mean, & tip)		Velocity Triangles (hub, mean, & tip)	
Blade chord		Blade chord	
Degree of Reaction		Degree of Reaction	
Mach Numbers (absolute & relative)		Mach Numbers (absolute & relative)	

Table of Contents

1 Introduction

This report presents the preliminary design of the mixed flow, triple spools, middle bypass ratio turbofan engine, designated the CJ 3000. The CJ 3000 is a candidate engine for the proposed next generation supersonic transport as per the Request for Proposal (RFP). Currently, there is no supersonic transport in operation. The baseline engine model is based on engine modeled in NASA/CR-2010-216842. The candidate engines must demonstrate at least 5% improvement in TSFC at specified thrust levels and substantiate weight savings. Furthermore, both cruise emissions goal and noise constraint, represented by exit jet velocity limited below 1375 ft/s, are imposed.

The engine shall meet or exceed the thrust levels shown in Table 1.1 at four key flight conditions. In addition, the thrust specific fuel consumption (TSFC) at each condition shall be at least 5% lower than the values shown in the table. The analysis of Sec 2 would basis on the uninstalled engine performance (with zero customer bleed and zero customer horsepower extraction, and MIL-E-5007D inlet pressure recovery [1]), while the check of installed engine performance will be discussed in detail in Sec 10.

Table 1 Uninstalled Engine Thrust and TSFC Requirements [1]

Flight Condition	Altitude (ft)	Mach	dTamb (°F)	Net Thrust (lbf)	TSFC (lbm/hr/lbf)
SLS Takeoff	0	0	0	70551	0.494
Hot Day Takeoff	0	0.25	27	61190	0.620
Transonic pinch point	40550	1.129	0	17197	0.804
Supersonic cruise	52500	1.6	0	16471	0.993

The design requirements and characteristics for the next generation supersonic transport in the RFP are shown in Table 1.2.

Table 1.2 General Characteristics of the Next Generation Supersonic Transport [1]

General characteristics	
Max. take-off weight	317,499 lb
Payload weight	21,000 lb
Operating empty weight	146,420 lb
Wing loading (takeoff)	77.5 psf
Power plant	2 × mixed-flow turbofans; 61,000 lbf each @ SLS
Performance	
Maximum speed	Mach 1.8 at 55,000 feet
Cruise speed	Mach 1.6 at 50,000-55,000 feet
Range	4000 nmi
Cruise L/D	9.2

Subsequent sections demonstrate the cycle analysis and optimization of the CJ 3000 at design and off-design conditions. The new aircraft engine performance results are compared with the baseline engine and requirements. Furthermore, a detailed engine component design is also presented, which demonstrates and provides justification for the use of advanced technologies in the CJ 3000. Then, the installed performance will be checked by the design of components. Finally, this report presents a detail structure analysis such as material choice, bearing arrangement, critical speed and detailed CAD model of the next generation supersonic transport, as well as a number of technological advances that will be used as noise suppression measures and Subsystems.

2 Cycle Analysis

This chapter describes the basic structure of the CJ 3000 engine and documents the cycle analysis program that was used to aid in the design of the middle bypass ratio turbofan. The optimal cycle design is presented in this chapter. The analysis code used to complete the cycle analysis was the gas turbine simulation software GasTurb 13, and the simulation of the CJ 3000 is available from the authors upon request.

2.1 Advanced Engine Cycle Concepts for the CJ 3000

2.1.1 Conventional Dual-spool Turbofan Engine

The first step in developing the optimal cycle for the CJ 3000 is to consider a number of different, but promising cycle concepts and determine which cycle concept will provide the optimal combination of performance, complexity, technology readiness level (TRL), and cost. To this end, a number of different novel cycles were considered. The first of these novel concepts is a dual-spool turbofan engine in a mixed-flow turbofan configuration, which is shown in Figure 2.1.
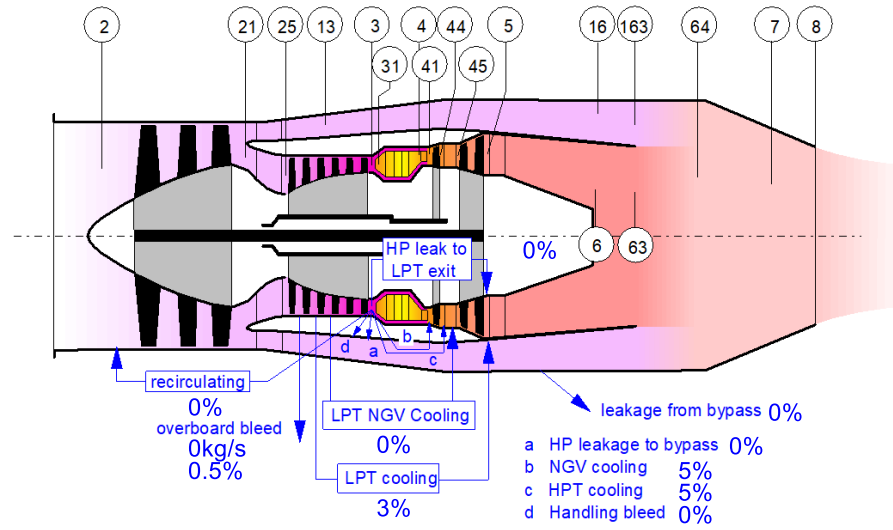
Figure 2.1 Dual-spool Mixed-flow Turbofan Engine

This dual-spool turbofan engine configuration is a conventional turbofan engine with high construction reliability. With emphasis on technological advances, the engine is relatively inexpensive. However, this concept seriously would have many limitations in practical design, especially with high overall pressure ratio (OPR) and big difference in pressure ratio between inner fan and outer fan, leading to difficulties in aerodynamic design of turbomachinery.

2.1.2 Dual-spool Turbofan Engine with CCA System

In addition to the dual-spool concept, another novel engine cycle considered was a mixed-flow turbofan engine with the addition of cooled cooling air (CCA) technology [2]. This CCA concept is shown in Figure 2.2.
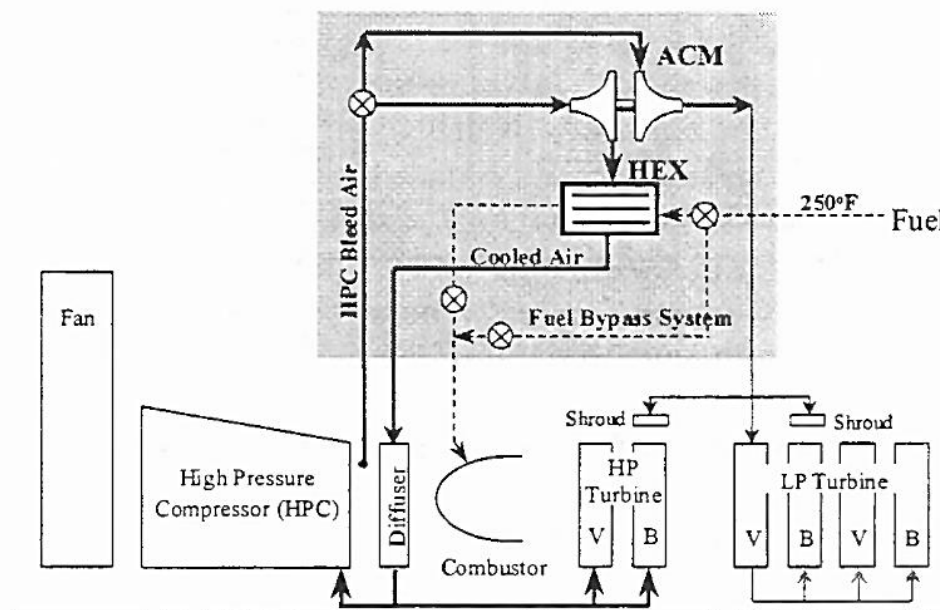
Figure 2.2 Mixed-flow Turbofan Engine with CCA [3]

This novel turbofan engine would apply an air-to-air or a fuel-to-air heat exchanger to cool the compressor bleed air normally used for cooling turbine machinery. Each approach assumes a CCA system capable of reducing the compressor bleed air temperature by as much as 400°F at the maximum T_3, and T_{41} operating condition [3], which would improve the cooling efficiency and make a positive impact on overall engine performance. However, this concept would also decrease the performance of the engine, as the CCA technology demand an extra air cycle machine (ACM) to increase the pressure of bleed air to guarantee that the cooled air flow would have adequate pressure margin to enter back into the core flow through the vane cooling holes, and thus some of the energy would be consumed, thrust would be reduced, and fuel consumption would be increased. A second consideration against the HEX module of ACM would set off pressure losses in the bypass and increase engine weight, with advanced material, such as CMC could decrease the amount of cooling as well. Due to the inherent drawbacks of both the dual-spool concept and the CCA concept, the engine design team decided that a triple-spool mixed-flow turbofan engine would best suit the needs of the next generation supersonic transport.

2.1.3 Triple -spool Turbofan Engine

While the dual-spool concept would offer the lowest costs and the CCA concept would reduce bleed air while generating the required levels of thrust and offering low TSFC, a triple-spool mixed-flow turbofan engine design would increase the pressure ratio and surging margin of compressors through adopting more spools. The advantages of the triple-spool turbofan engine will be analyzed separately In pneumatic and structural aspects as follows.

Fig. 2.3 shows the comparison of the flow path of dual-spool engine and triple engine. Dual spool booster stage flow path is significantly higher than triple spool internal -pressure compressor flow path. Although the GEnx boost stage flow path radius has been raised to be similar to that of a low-pressure turbine, its tip speed is only 65% of Trent1000, and its compression capacity is still limited. There is a large gap between the booster stage flow path and the inlet of the HPC. In order to achieve the connection of the flow path and ensure that the air flow does not separate, a longer, larger transfer flow path is used here. Similarly, the same problem exists between high and low-pressure turbines. In the triple-spool structure, internal pressure rotor rotates at a much higher speed than the LP rotor, so its flow path radius is lower, and the internal pressure compressor uses a flow path that is similar to constant hub diameter, and the last two stages

further reduce the flow path. Therefore, the transfer paths between the fan and internal pressure compressor, the internal pressure compressor and the HPC are all in a gentler transition. Although there is one more internal -pressure turbine in the triple spool structure, the transition flow path is one more than the dual-spool structure, the total axial length of the flow path is even smaller than that of the dual-spool. This flow design leads to the very small space of the structure design, which puts forward higher requirements for the structural strength design of the first stage rotor.
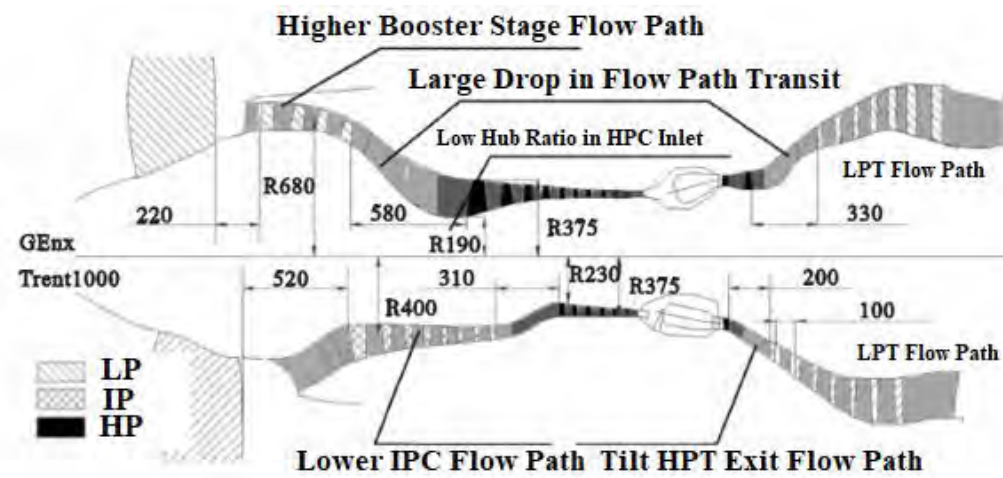
Figure 3.3 Flow Path Comparison Diagram

Fig. 2.4 shows the comparison of the rotor fulcrum of dual-spool engine and triple engine. The most obvious difference between the three rotors and the two rotors is the design of the bearing frame. The pivot span of the LPT shaft of dual spool structure is longer. And the entire HPC of triple-spool structure has fewer stages, is very compact, low weight, and the moment of inertia and pneumatic load are both small. In summary, in pursuit of a high-efficiency engine architecture, the design team opted for triple-spool structure in the CJ 3000.
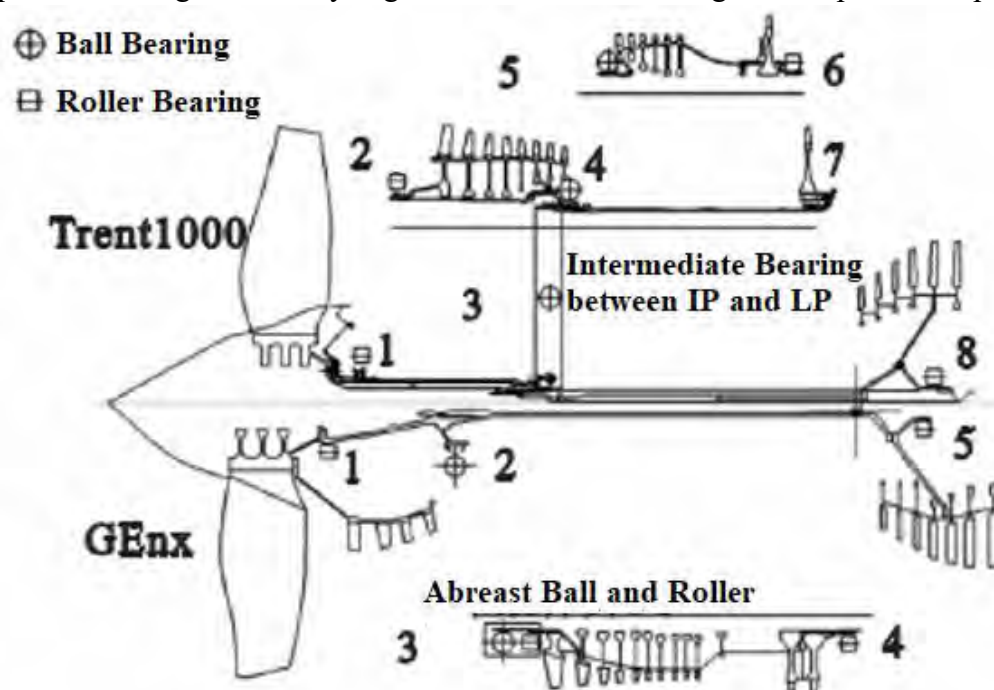
Figure 4.4 Rotor Fulcrum Comparison

By increasing the pressure ratio and efficiency, a higher overall pressure ratio (OPR) could be used with limited compressor stages. Hence the required the requests of thrust and TSFC would be met more neatly with acceptable costs. Since the CJ 3000 is being utilized on a supersonic transport aircraft, the most sensible option is to produce a triple-spool mixed-flow turbofan engine with emphasis on technological advances that will be proven ready by 2025. To this end, we have adopted promising technologies with TRL $\geq$ 6.

2.2 Engine Components and Diagrams

The CJ 3000 is a middle bypass ratio, mixed-flow, triple-spool turbofan engine composed of the following ten main components:
1. Air Intake System   2. Transonic Fan   3. Internal-Pressure Compressor
4. High-Pressure Compressor   5. LDI Combustor & Fuel System
6. High-Pressure Turbine   7. Internal-Pressure Turbine
8. Low-Pressure Turbine   9. Lobed Mixer   10. Exhaust System

In addition to these ten main components, engine auxiliary systems (e.g., APU, FADEC, anti-icing) are fully designed and integrated in the aircraft. The location of these engine components is indicated in Figure 2.5 (from GasTurb 13 Analysis Code). As stated in the RFP, one of the major requirements for the CJ 3000 is the ability to fit within the required engine envelope, which allows for a maximum fan area of less than 7630 in^2 [1]. With this geometrical constraint in hand, then the engine components are designed and the detailed flow through the CJ 3000 is determined. The CJ 3000 performance superiority over the conventional turbofan engine is that it has super-cruise capabilities, and as such there is no afterburner installed in the CJ 3000, which drastically reduces fuel consumption, exhaust noise and engine weight.
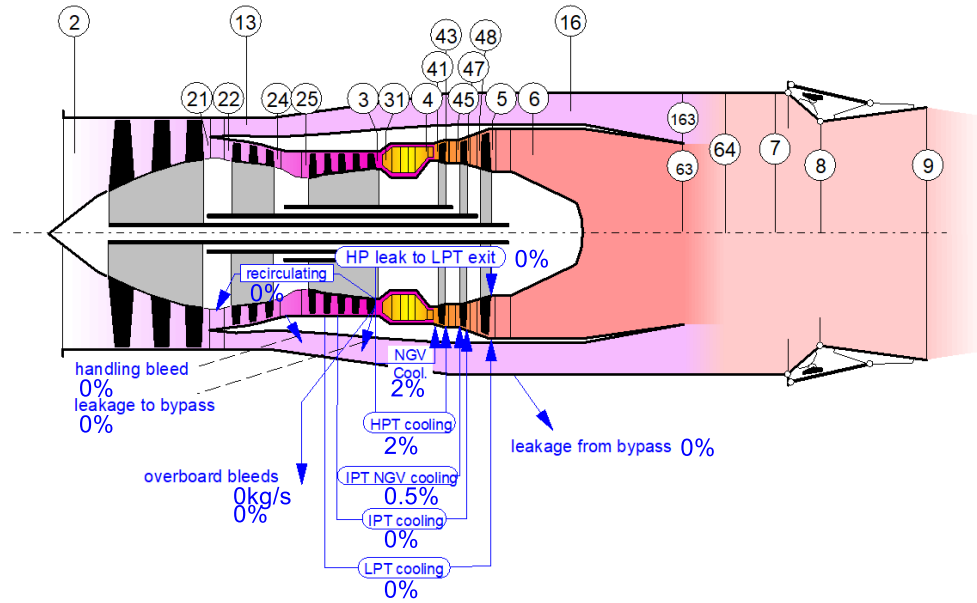
Figure 2.5 Station Numbers for the CJ 3000 – A Mixed-Flow Turbofan Engine [4]

2.3 On-Design Analysis and Simulation Validation of Baseline Engine

This section briefly describes the on-design cycle analysis and validation of the baseline engine in the selected analysis code, GasTurb 13 [4] to provide a valid comparison of weights and performance for the new concept.

Figure Appendix-A1 (see details at Appendix A) presents the baseline engine characteristics of the RFP at the supersonic cruise condition. The exact cycle parameters for the supersonic cruise condition are provided in the RFP and are verified by the team through usage of the gas turbine engine simulation software GasTurb 13. GasTurb 13 will serve as the primary design code for the cycle analysis of the CJ 3000. Table 2.1 shows the error percentage of the baseline engine performance between the RFP and the simulation.

Table 2.1 Performance Simulation Comparison - Simulation vs RFP

Condition	Cycle Parameter	Simulation	RFP	Error (%)
Supersonic Cruise	Thrust (lbm)	15893	15850.8	0.27
	TSFC (lbm/lbf/h)	1.0092	1.0111	0.19

The error percentage is below maximum 0.27. The GasTurb 13 is feasible to make cycle analyses for the CJ 3000.

2.4 CJ 3000 Cycle Analysis: New Engine Optimization

As we have established parametric validation of the baseline engine using GasTurb 13, we proceed to develop a model for the CJ 3000. The CJ 3000 is a mixed- flow, triple-spool, middle bypass ratio turbofan engine. The cycle analysis of the CJ 3000 aims to reduce specific fuel consumption (TSFC) and reach thrust levels at all flight conditions, as well as to reduce the weight of the powerplant using advanced technology component design utilizing advanced materials and manufacturing techniques. To minimize the TSFC of the CJ 3000, trade studies are conducted to determine the optimal combination of bypass ratio, fan pressure ratio, turbine entry temperature, and overall pressure ratio, while the distribution of pressure ratio between internal compressor and high compressor are mainly decided by the aerodynamic design of compressors for its faint effect on the performance. One of the most important design limits implemented in this cycle analysis is a maximum turbine entry temperature of 3290 °R. The basis for this design limit is that silicon carbide (SiC) ceramic-matrix-composite (CMC) material has been tested by GE Aviation to be able to withstand service temperatures upwards of 2400 °F [5] without the need for traditional cooling techniques [6]. This represents a breakthrough technology in future gas turbine engine designs, in which turbines are uncooled. The prospect of using an uncooled turbine and the corresponding performance gains are validated at GE Aviation, and the design team has rated this technology with a TRL of 9 for the entry-into-service date of 2025 [7]. In addition, because the rotating turbine blades made from CMCs are one-third the weight of conventional nickel alloys used in the high-stress turbine, they allow GE to reduce the size and weight of the metal disks to which the CMCs system is connected [7].

Furthermore, through the use of advanced environmental barrier coatings (EBCs) that also perform as thermal barrier coatings (TBCs), the CMCs components could have surface temperature capability to 2700ºF. The EBCs also provide reduced erosion rates to enhance durability and prolong component life. The design team has rated this technology with a TRL of 6 [8].

Therefore, turbine cooling might not be needed if our turbine inlet temperature is lower than the dangerous values of Carbon Fiber Reinforced SiC CMC (2700 ºF). However, on this condition, low amount of cooling air seems feasible to ensure the sustainability of turbine stage [8], especially on the leading edges of HPT vane and rotor. Cooling air value of 3% in total seems appropriate [9]. Besides, to cool turbine discs and seal rim, for HP and IP turbines around 0.5% of flow per disc face is required. For LP or power turbines the disc sealing requirement reduces to 0.25% [10]. Hence the max turbine entry temperature would grow to 3290 °R [2]. This estimate was taken into account when Tt4 might rise 300 ºF due to performance degradation to adapt to a longer engine life.

2.4.1 On-Design Parametric Analysis of the CJ 3000

Generally speaking, engines with supersonic capabilities are normally sized at "top-of-climb" conditions, rather than at takeoff, and the CJ 3000 follows this practice [1]. Hence the on-design condition for the next generation trainer is defined as "top-of-climb," which is at Mach 1.6 and 52500 feet, the supersonic cruise condition. To begin this analysis, a few constraints and assumptions were made. First, the fan inlet area of the new engine is limited to 7630 in^2 by the existing engine envelope. This limits the cross-sectional area at the engine face (station 2), which thus limits the corrected mass flow rate at the engine face with a reasonable axial Mach number, i.e., ~0.5-0.6. For this reason, the corrected mass flow rate at all flight conditions (on-design and off-design points) was chosen to be held below 1714 lbm/s,

to ensure that the fan area did not exceed the limit of fan inlet area.

A pre-analysis will be conducted in turn to determine the preferred scope of turbine entry temperature, overall pressure ratio, bypass ratio, and fan pressure ratio. Firstly, the turbine entry temperature of baseline engine, 3273.6 °R, is close to the limit (3290 °R). So, it may be chosen between 3273.6 °R and 3290 °R, and would not be greatly changed from the baseline. Secondly, the core thermal efficiency of the baseline engine is too low and the TSFC is too high to reach the limit of performance requirement. With a basically determined temperature, the most economical overall pressure ratio that leads to the lowest TSFC could be found. Fig 2.6 shows the relationship between TSFC and OPR, indicating that the most economical OPR≈51. However, the design limit of OPR was limited to 45 due to the design level of compressor stages and efficiency. Hence, the OPR may be selected between 36.8 and 45. Thirdly, according to RFP [1], the exhaust jet velocity of baseline engine at takeoff is 1544.9 ft/s, which greatly exceeds the limit of 1375 ft/s. To lower the exhaust jet velocity, a higher BPR with mixed exhaust could be used. With A9/A8 equal to 1.011 and Mach number at A8 equal to 1, the V9-to-V8 ratio is equal to 1.119 [1]. Therefore, the constraints on V9 can be converted into constraints on V8. Fig 2.7 shows the relationship between V8 and BPR with a stable A9/A8 equal to 1.011, which shows that the BPR should be at least higher than 2.5 to reach the limit of V9. Fourthly, as the OPR increases and T4 changing little with BPR increasing, the value of the optimal fan pressure ratio is complicated. According to Ref [12], when the BPR of mixed exhaust engine is 2.5 to 3.5, the FPR is generally between 2.25 and 2.5. Additionally, in order to ensure that the number of fan stages is not greater than 2 to ensure a low engine weight, and that the single stage fan pressure ratio is not more than 1.7 to ensure a high fan efficiency, the FPR is limited to less than 2.89. The distribution of pressure ratio between IPC and HPC are mainly decided by the aerodynamic design of compressors for its faint effect on the performance. Hence, the ratio of IPR to HPR is temporarily taken as 1.25, a convenient value for aerodynamic design. The initially determined range of cycle parameters is listed in Table 2.2.

Table 2.2 The Pre-Analysis Range of Cycle Parameters

Cycle Parameter	Baseline Engine	Pre-Analysis Range
T4 (°R)	3273.6	3273.6~3290
OPR	36.8	36.8~45
BPR	1.91	2.5~3.5
FPR	2.276	2.25 ~2.5

In order to reduce the weight and ensure the excellent performance of the engine, the number of stages of each turbomachine is limited to be or less than that of the 19-stage baseline engine, that is, 2 stages for the fan, 9 stages in total for IP and HP compressor, 2 stages in total for HP and IP turbines and 4 stages for LP turbine. In detail, 5-stage is designed for IP compressor and 4-stage is designed for HP compressor to adapt to the ratio of IPR to HPR, 1.25. Since the FPR is probably higher than the baseline engine was achieved while using the same 2-stage fan as the baseline, the isentropic efficiency of the fan was selected to be 0.88, which is about 1% lower than the baseline. By using both IP and HP rotors to achieve the pressure increase of the original single rotor, both IPC and HPC can achieve significant improvements in efficiency, even if the pressure increase task is more difficult. Hence, the isentropic efficiency of IPC and HPC was selected to be 0.88. Due to similar reasons as IPC and HPC, the isentropic efficiency of HPT and IPT has also been improved, and both are determined to be 0.92. Due to the optimization of the HPT and IPT in the expansion performance and the pneumatic flow path, the efficiency design of LPT can also be improved. Its isentropic efficiency is selected to be 0.92, which will be verified in the turbine design section.

HP Compressor Pressure Ratio = 16 ... 25
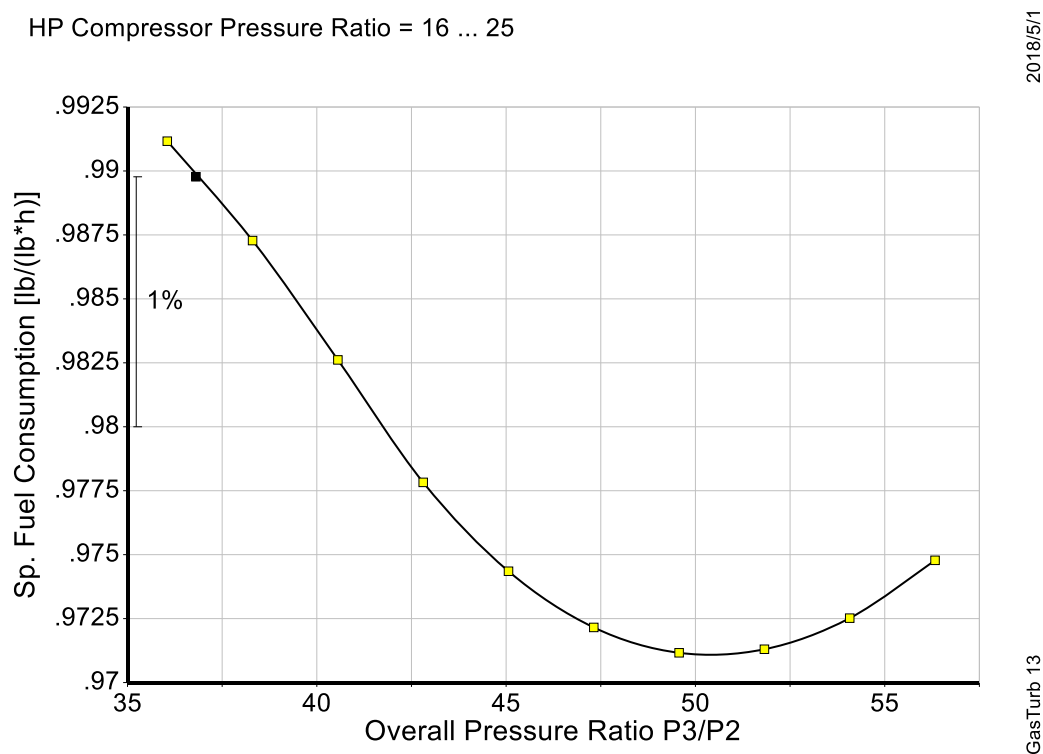
2018/5/1

GasTurb 13

Figure 2.6 Initial Parametric Study of TSFC and OPR
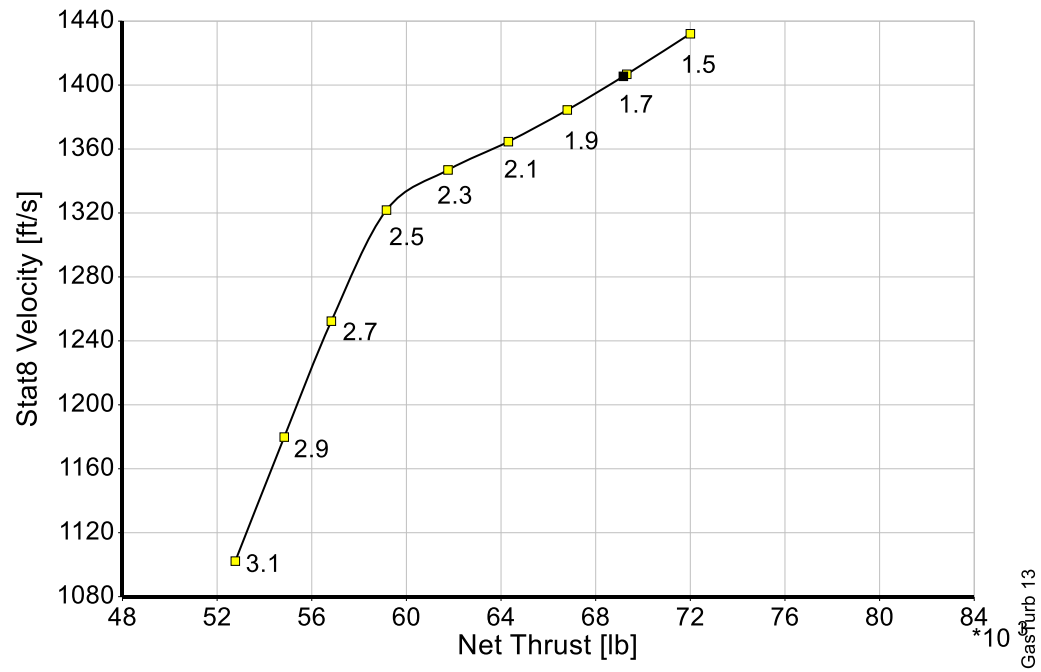
Figure 2.7 Initial Parametric Study of V8 and BPR

From here, we then used the optimization program featured in GasTurb 13 to address the impact of T4, OPR, BPR, and FPR on TSFC. Some of the most critical trade studies to determine the optimal parameters for the on-design condition of the CJ 3000 are shown in Figure 2.9. The black square shown in the carpet plots of Figure 2.8 represents the location of the overall optimization.
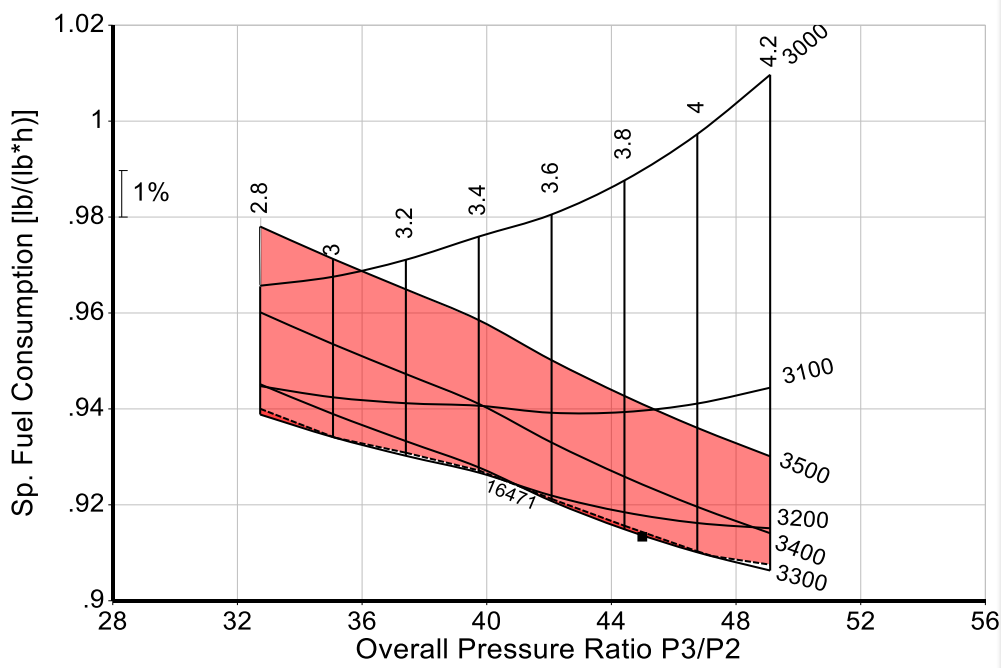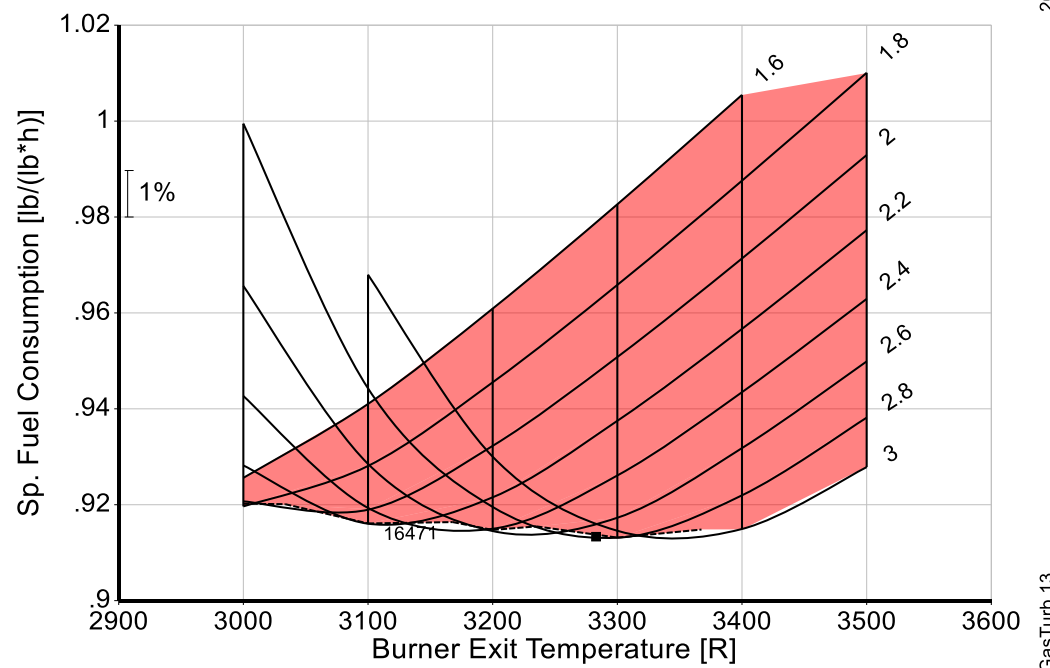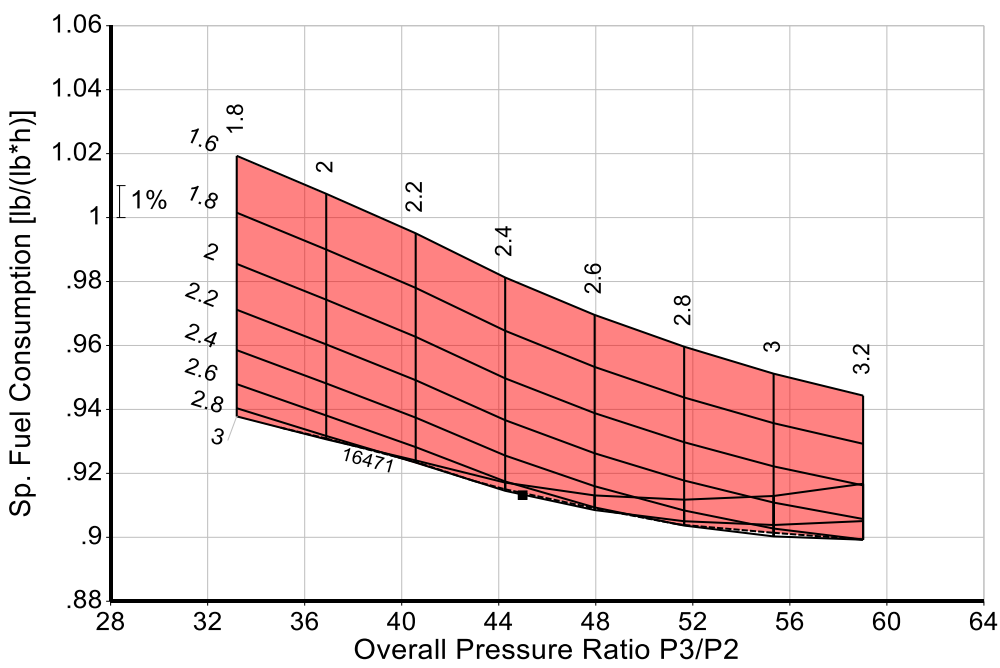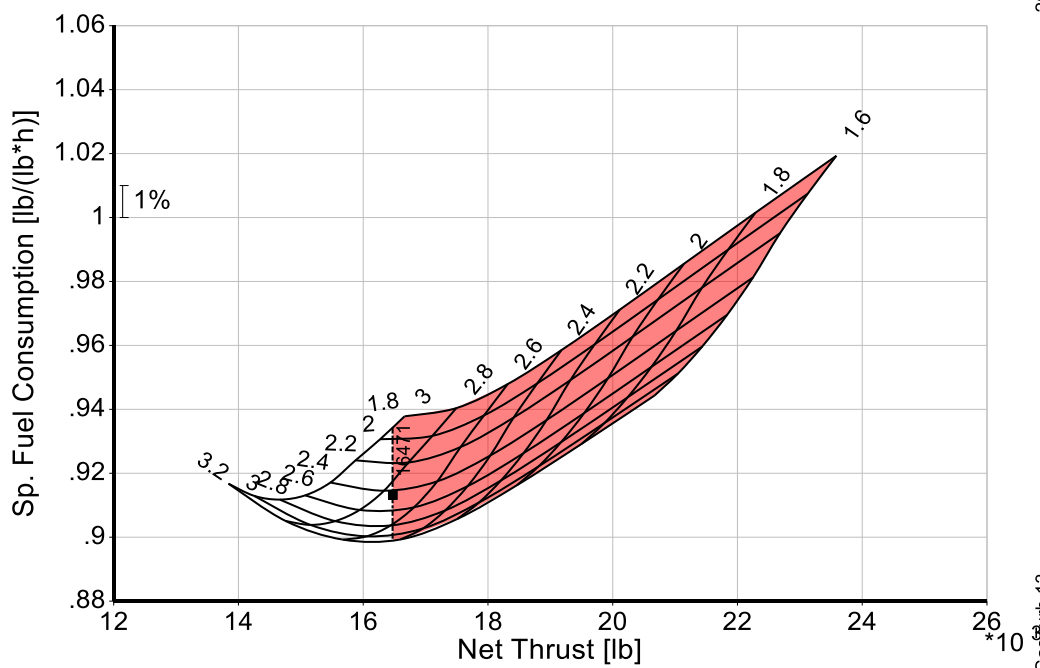
Figure 2.8 Trade Studies of Cruise T4, BPR, FPR, OPR, and TSFC for the CJ 3000 [4]

We note in Figure 2.8 that as OPR increases, by choosing proper turbine entry temperature (T4), the TSFC would decrease.

Furthermore, with the maximum OPR of 45 to provide convenience for compressor aerodynamic design, the lowest TSFC could be found as the T4 is between 3200°R and 3300°R. Considering the lower T4 has a limit of 3290°R, T4 was chosen as 3282.5°R. Hence BPR was chosen as 2.75. Besides, TSFC decreases as fan pressure ratio increases (and thus overall pressure ratio increases) with an appropriate bypass ratio. It is also necessary to focus on the thrust limit. Thus, for the design point of supersonic cruise a TSFC of 0.9132 lbm/lbf/h was selected, as well as a bypass ratio of 2.75 and T4 of 3282.5 °R. The choice of design bypass ratio is a function of maximum turbine entry temperature and the variation of TSFC at all four of the main flight conditions and will be explained in more depth in Section 2.4.2. Figure Appendix-A2 (see details at Appendix A) presents the performance of CJ 3000 at the supersonic cruise condition. The cycle parameters for the CJ 3000 at supersonic cruise are described in Table 2.3, and Table 2.4 shows a comparison of important cycle parameters for both the CJ 3000 and the requirement at supersonic cruise.

Table 2.3 Optimized Performance of the CJ 3000 at Supersonic Cruise

Cycle Parameter	Baseline	CJ 3000
BPR	1.91	2.75
T4 (°R)	3273.6	3282.5
OPR	36.8	45.0
FPR	2.276	2.440
IPR	/	4.84

Table 2.4 Comparison of Important Performance Parameters at Supersonic Cruise

Performance Parameter	Requirement	CJ 3000	Margin (%)
Thrust (lbm)	16471	16471.16	Match
TSFC (lbm/lbf/h)	0.993	0.9132	8.04
Core Thermal Efficiency	0.608	0.664	9.21

From this comparison of performance parameters at supersonic cruise between the CJ 3000 and the requirement, we note that the CJ 3000 improves fuel efficiency over 8%, which is a remarkable result. The other most notable feature of the design for the CJ 3000 is the notable rise in overall pressure ratio (nearly 45), which increases the core thermal efficiency of the engine significantly as it is compared to the core efficiency of baseline engine.

2.4.2 Off-Design Analysis of the CJ 3000

With the cycle parameters at the on-design point of supersonic cruise determined, it is necessary to assess the performance of the CJ 3000 at major off-design conditions as well. The RFP states that the next generation trainer must takeoff at the standard sea level static day and the hot day with +27°F. It could also fly through transonic pinch point at Mach 1.129 and 40550 feet. To conduct the off-design analysis, a series of mission points were defined in GasTurb 13, corresponding to the three above listed flight conditions. For the CJ 3000 at off-design conditions, the goal was to obtain the required thrusts while achieving improved fuel efficiency from the baseline engine model. Figure 2.9, Figure 2.10, Figure 2.111 and Figure 2.12 present four critical trade studies that dictate the off-design cycle parameters for the CJ 3000: Figure 2.9 showing the relationship between cruise bypass ratio and the turbine entry temperature required at cruise to generate 16471 lbf of thrust, Figure 2.10 showing the relationship between cruise bypass ratio and the exhaust jet velocity (V_9) required at SLS and hot day takeoff to generate 70551 lbf or 61190 lbf of thrust, Figure 2.11 showing the relationship between cruise bypass ratio and TSFC while meeting the thrust levels at each of the four main flight conditions, and Figure 2.12 showing the relationship between cruise bypass ratio and the estimated weight (see Sec 2.4.3 for details).
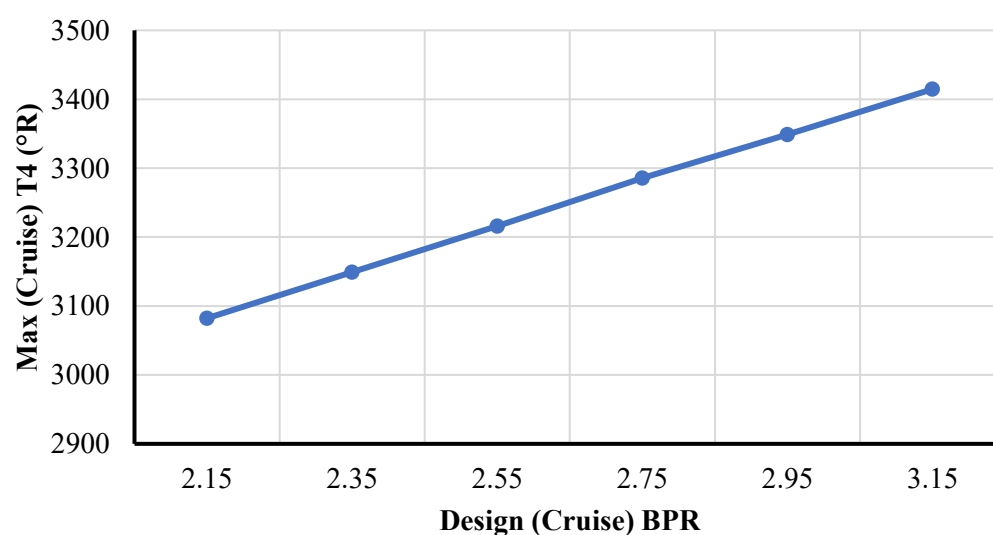
Figure 2.9 Off-Design Cycle Parameters Trade Studies for the CJ 3000 – Cruise BPR vs Max T4
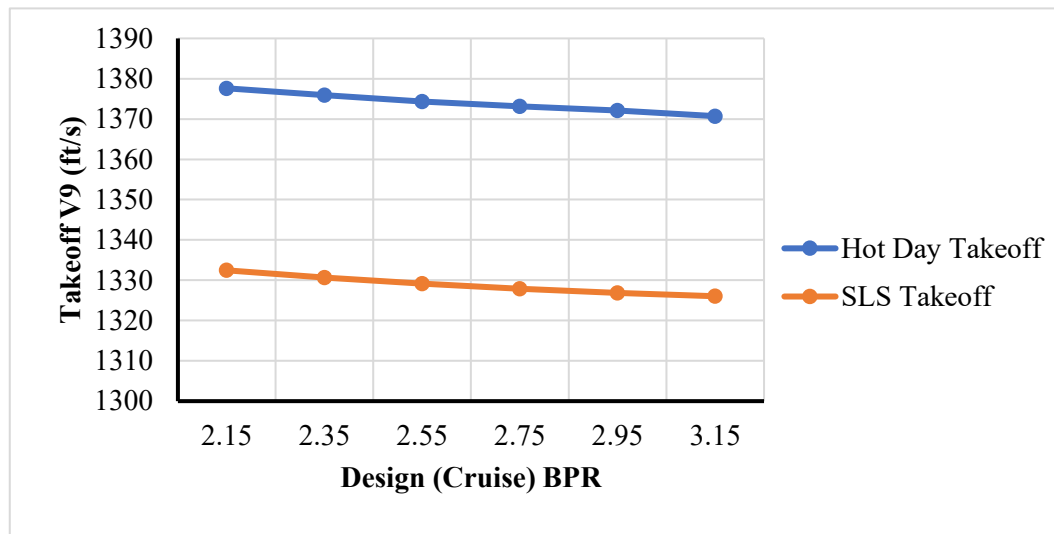
Figure 2.10 Off-Design Cycle Parameters Trade Studies for the CJ 3000 – Cruise BPR vs Take-off V9
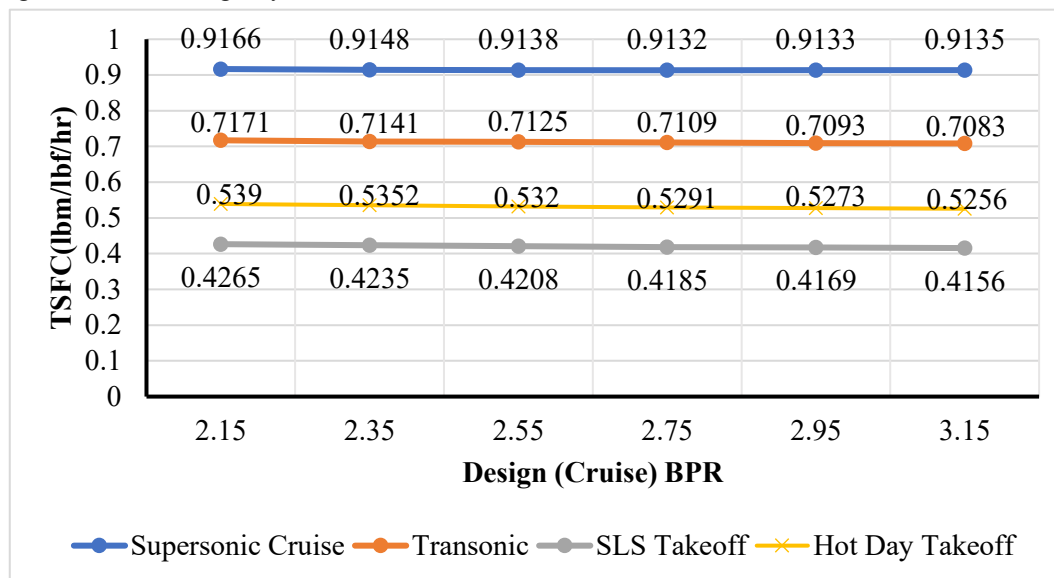
Figure 2.11 Off-Design Cycle Parameters Trade Studies for the CJ 3000 – Cruise BPR vs TSFC
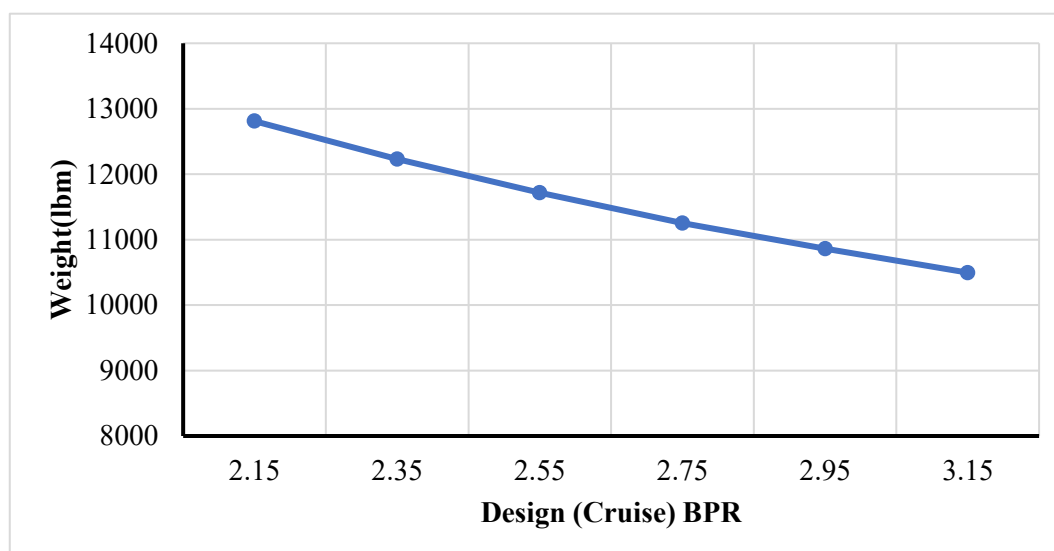
Figure 2.12 Off-Design Cycle Parameters Trade Studies for the CJ 3000 – Cruise BPR vs Weight

From Figure 2.9, we find that the max T4 increases while the on-design bypass ratio (BPR) increases. From Figure 2.10, we find that V9 at both SLS and hot day decreases, which would reduce takeoff noise while the on-design BPR increases. From Figure 2.11, we note that the TSFC at cruise meet the lowest value when on-design BPR equals 2.75. And the TSFC at transonic pinch point, SLS takeoff and hot day takeoff decreases as BPR increases. At the meanwhile, the weight of engine decreases rapidly while BPR increases. The final on-design bypass ratio chosen was 2.75, as this value was the largest cruise bypass ratio in which the maximum turbine entry temperature across all flight conditions was held below 3290 °R and V9 at take-off was held below 1375 ft/s with low enough weight. This is a compromise choice to make sure that no more cooling air is demanded, the noise at take-off would be easily controlled and the fuel cost during cruise would be minimal, while the engine weight would not be nicely reduced. Besides, the choice would also lead to the lowest TSFC at supersonic cruise, which would maximize the reduction of the fuel cost during the whole mission (see Sec 4.1 for details). From this iterative cycle analysis relating on-design parameters to off-design performance, it was possible to generate the final cycle characteristics for each off-design condition. The key parameters of the CJ 3000 off-design performance are summarized in Table 2.5.

Table 2.5 Performance of the CJ 3000 at Four Conditions

Mach Number	0	0.25	1.129	1.6
Altitude (ft)	0	0	40550	52500
Thrust (lbf)	70579.63	61208.17	17207.34	16471.16
TSFC (lbm/lbf/h)	0.4185	0.5291	0.7109	0.9132
T4 (°R)	2773.0	2938.80	2708.06	3282.5
OPR	43.697	43.740	45.036	45.003
FPR	2.421	2.428	2.471	2.440
IPR	4.855	4.844	4.840	4.839
BPR	2.607	2.600	2.594	2.750
A9/A8	1	1	1.35	1.80
V9 (ft/s)	1327.92	1373.13	/	/

According to Table 2.5, all performance cycles at all work points meets the requirements of margins in RFP. The details of margin analysis will be shown in Sec. 2.5.

2.4.3 Engine Weight Analysis

In order to analysis the engine weight, a wide range of research is made about the methods and ways. Among the numerous applications and experiments that have been worked upon, one significant method seems to provide the most accurate results, which is WATE++ program that has been developed by NASA in collaboration with Boeing. Since this entire program is not publicly available, a basic version has been found from the referenced MIT report [11]. In this simpler version, the variables that effect directly the engine weight are OPR, BPR and mass flow. The engine weight can be estimated by Eq. (2.1).

$$W_{engine} = a * \left(\frac{\dot{m}_{core}}{100}\right)^b * \left(\frac{OPR}{40}\right)^c \tag{2.1}$$

While use advanced materials (including carbon composites, CMC, MMC, and TiAl) to make engines, the parameters of Eq. (2.1) can be estimated as Eq. (2.2) shows:

$$\begin{cases} a = (-6.204 \times 10^{-1}) \, BPR^2 + (2.373 \times 10^2)) \, BPR + 1702 \\ b = (5.845 \times 10^{-5}) \, BPR^2 - (5.866 \times 10^{-3}) \, BPR + 1.045 \\ c = (-1.918 \times 10^{-3}) \, BPR + 0.0677 \end{cases} \tag{2.2}$$

This version of the estimation is used for geared turbofan engines. Since the ideology of this formula and method is similar, we are going to measure the accuracy of the function with the baseline engine model, which is shown in Table 2.6.

Table 2.6 Weight Estimation Comparison – The Baseline Engine

Engine Name	Baseline Engine
Airflow$_{core}$ (lbm/s)	571.17
OPR	35.0
BPR	1.71
W$_{real}$ (lbm)	13000
W$_{estimation}$ (lbm)	12679
Error $(\%)$	2.469

It can be seen that the error percentage is only 2.469. Besides, by measuring the accuracy of the function with similar mixed flow turbofan engines, the error percentage is usually below maximum 3 [9]. The basic formula from WATE++ and MIT report seems to be feasible to make analyses and implement for the new designed engine. Therefore, we are going to estimate the weight of the CJ 3000.

Table 2.7 Weight Estimation - The CJ 3000

Engine Name	CJ 3000
Airflow$_{core}$ (lbm/s)	450.523
OPR	43.697
BPR	2.607
W$_{estimation}$ (lbm)	10981

With the new engine design parameters preference, new engine weight is approximately calculated in Table 10. With the 2.469% error margin that was measured from baseline model weight estimations comparison, new engine weight is calculated in Table 2.8.

Table 2.8 Weight Comparison - Baseline Engine vs CJ 3000

Engine Name	CJ 3000	Baseline Engine
Weight (lbm)	11252	13000
Weight (kg)	5103.82	5896.70

According to Table 2.8, the weight of CJ 3000 has been greatly reduced while compared to the baseline engine. The details of weight comparison will be shown in Sec. 2.5.

2.5 Performance Comparison with the Baseline Engine Model and Requirements

Upon comparison of the on-design performance (supersonic cruise) of the requirement and the CJ 3000 as shown in Table 2.5, we note that the TSFC is reduced by 8.04%, a remarkable increase in engine fuel efficiency. Table 2.9 shows a comparison of the most important cycle parameters at takeoff, transonic pinch point and supersonic cruise for both the requirements and the CJ 3000.

Table 2.9 Comparison of Engine Performance between the Requirements and the CJ 3000

Flight Condition	Cycle Parameter	Requirements	CJ 3000	Margin (%)
SLS Takeoff	Thrust (lbf)	70551	70579.63	0.04
	TSFC (lbm/lbf/h)	0.494	0.4185	15.28
	V9 (ft/s)	1375.0	1327.92	3.42
Hot Day Takeoff	Thrust (lbf)	61190	61208.17	0.03
	TSFC (lbm/lbf/h)	0.620	0.5291	14.66
	V9 (ft/s)	1375	1373.13	0.14
Transonic Pinch Point	Thrust (lbf)	17197	17207.34	0.06
	TSFC (lbm/lbf/h)	0.804	0.7109	11.58
Supersonic Cruise	Thrust (lbf)	16471	16417.16	Match
	TSFC (lbm/lbf/h)	0.993	0.9132	8.04

From Table 2.9, we note that fuel efficiency of the CJ 3000 meets the requirements at every operating point with the margin over 8 %. For SLS take-off, the CJ 3000 not only decreases fuel consumption by over 15% of the requirement, but also decreases exhaust jet velocity by over 3% of the requirement, which seriously would be helpful to control the noise of taking off. For hot day take-off, the CJ 3000 decreases fuel consumption by over 14% of the requirement and exhaust jet velocity by 0.14% of the requirement, which would satisfy the noise of taking off at some bad conditions. For transonic pinch point, the CJ 3000 decreases fuel consumption by over 11% of the requirement. For supersonic cruise, the CJ 3000 decreases fuel consumption by over 8% of the requirement. These fuel reductions grant the next generation supersonic transport the ability to supersonic cruise very efficiently. These impressive performance gains are functions of the major design selections of the CJ 3000, namely the lack of an afterburner (which enables supersonic cruise) and SiC/SiC CMC turbine blades with EACs (which decreases cooling of the turbine blades). In addition to the gains in fuel efficiency of the CJ 3000 over the requirements, the total weight of the CJ 3000 is also less than that of the baseline engine. Table 2.10 presents a comparison of major geometric parameters between the two engines.

Table 2.10 Comparison of Geometric Parameters between the Baseline Engine and the CJ 3000

Geometric Parameter	Baseline Engine	CJ 3000	Difference (%)
Fan Area (in^2)	7630.10	7012.05	8.10
Weight (lb)	13000	11252	13.45

Based on these considerations, the CJ 3000 reaches the uninstalled requirements in terms of both fuel efficiency and thrusts, while also drastically reducing the overall weight.

3 Constraint Analysis

The objective of the constraint analysis is to lead to the fortunate discovery that several of the leading performance requirements of the Request for Proposal (RFP) can be translated into functional relationships between the minimum thrust-to-weight or thrust loading at sea-level takeoff (T_{SL}/W_{TO}) and wing loading at takeoff (W_{TO}/S). Thrust loading and wing loading for each segment is then plotted in a constraint diagram to find the solution space for the aircraft [12]. This then sizes an aircraft for all modes of operation. The constraining equations are developed from the following performance constraints: takeoff distance constraints, landing distance constraints, climb constraints, and cruise constraints.

3.1 Determination of Mission Weights

For the next generation supersonic transport, it is necessary to determine the empty and takeoff weights corresponding to the mission. To determine the mission weights, an iteration approach would be summarized with the following procedure:

1) According to the RFP [1], the max take-off weight (W_{TO}) is 317499 lb and the operating empty weight (W_E) is 146420 lb.

2) According to Sec 2.4, the CJ 3000 saves 1748 lb from the baseline engine.

3) Hence the new max take-off weight is 314003 lb and new operating empty weight is 142924 lb. Then the take-off weight to operating empty weight ratio (Gt) could be calculated.

$$Gt = \frac{W_{TO}}{W_E} \qquad (3.1)$$

4) According to the Eq. (3.2) [12], for passenger aircraft, the take-off weight to operating empty weight ratio (Ge) and W_{TO} have the following relationship:

$$Ge = 1.02 * W_{TO}^{-0.06} \qquad (3.2)$$

5) By using W_{TO}, Ge can be calculated. Secondly assign the value of Ge to Gt and get a new W_{TO} by using Gt and W_E. Thirdly a new Ge can be calculated by new W_{TO}.

6) Compare the Ge to Gt, and then iterate about the guessed W_{TO} to bring the absolute value of the difference between Ge and Gt to within 0.01%.

7) In addition, to ensure the airplane can respond to unexpected situations during the flight mission, we think the mission of the aircraft could loiter at 15000 ft with Ma 0.5 for 45 minutes should be added by convention. Hence, the fuel weight converted by the iteration W_{TO} and W_E will be increased by 10% to adapt to this extra requirement.

After the iteration, the take-off weight of the next supersonic transport was determined to be 312282 lb.

3.2 Drag Polar Estimation

For nearly all of the performance constraints, the drag polar for every flight configuration must be known to proceed. There is a total of five main flight configurations for the next generation supersonic transport, including the clean configuration (cruise), takeoff with landing gear up or down, and landing with landing gear up or down. Using the takeoff weight estimated in Sec 3.1, the drag polar for each of the five main flight configurations of the next generation trainer can be determined using the techniques outlined in Ref [13]. The drag polar for every flight configuration of the next generation trainer can be seen in Table 3.1.

Table 3.1 Drag Polar Estimation for Next General Supersonic Transport

Flight Configuration	Drag Polar Estimation
Low Speed, Clean	$CD = 0.0154 + 0.0374CL^2$
Takeoff, Gear Up	$CD = 0.0304 + 0.0398CL^2$
Takeoff, Gear Down	$CD = 0.0474 + 0.0398CL^2$
Landing, Gear Up	$CD = 0.0754 + 0.0424CL^2$
Landing, Gear Down	$CD = 0.0924 + 0.0424CL^2$

3.3 Takeoff Distance Constraint

One of the most important performance constraints to consider is takeoff distance. The takeoff criterion used for the next generation supersonic transport was selected to be a minimum runway length of 7200 ft according to the conventional runway length of passenger airports. Thus, the following equation, which is rearranged form of Equation (3.3) [13] can be utilized to describe the takeoff performance constraint of the next generation supersonic transport:

$$\left(\frac{T}{W}\right)_{TO} = \frac{4(4+\lambda)}{3(5+\lambda)} + \left[\frac{\left(\frac{0.0447\left(\frac{W}{S}\right)_{TO}}{s_{TOG}\rho}\right) + 0.72C_{D0}}{C_{L_{max,TO}}} + \mu_g\right] \tag{3.3}$$

where λ is the bypass ratio of the engine at takeoff, $C_{L_{max,TO}}$ is the maximum lift coefficient at takeoff (selected from Ref [13], Table 3.1, supersonic cruise airplanes), μ_g is the ground friction coefficient (value selected to be 0.03 from Ref [13], page 91), s_{TOG} is the ground run takeoff distance (runway length of 7200 ft), ρ is the density at sea level on the standard day, and C_{D0} is the parasite drag coefficient for the takeoff, gears down flight configuration [13].

3.4 Landing Distance Constraint

Another one of the most important performance constraints to consider is landing distance. The landing criterion used for the next generation supersonic cruise was selected to be a minimum runway length of 7200 ft as well. The landing distance performance constraint is a single value that the wing loading cannot exceed. This landing constraint can be formulated from a form of Equation (3.4) [13], and is as follows:

$$\frac{W}{S} = \frac{\rho V_{SL}^2 C_{L_{max,L}}}{2\left(\frac{W_L}{W_{TO}}\right)} \tag{3.4}$$

where ρ is the density at sea level on the standard day, V_{SL} is the stall speed during landing, $C_{L_{max,L}}$ is the maximum lift coefficient during landing (selected from Table 3.1 of Ref [13]), and W_L/W_{TO} is the ratio of landing weight to takeoff weight (selected as 0.63 from Table 3.3 of Ref [13]) .

3.5 Climb Constraint

Another performance constraints to consider is climb. Specifically, the next generation supersonic transport is sized for climb by FAR 25.121 (OEI), which is a balked landing climb with one engine inoperative [13]. For FAR 25.121 (OEI), the climb gradient (CGR) is constrained as 0.021 [13]. With this information, the next generation trainer climb constraint from FAR 25.121 (OEI) can be described using Equation (3.5) [13] as follows:

$$\frac{T}{W} = \frac{N}{N-1} * \left(\frac{1}{L/D} + CGR\right) \tag{3.5}$$

where N is the number of engines on the aircraft (N=2), L/D is the lift-to-drag ratio in the approach position (L/D=9.2, according to RFP), and CGR is the climb gradient [6].

3.6 Supersonic Cruise Constraint

Another one of the most important performance constraints to consider is supersonic cruise. The supersonic cruise condition is at Mach 1.6 and 52500 feet, where α, the thrust ratio is calculated as 0.2735 and β, the weight ratio is estimated as 0.95 [12]. Thus, this supersonic cruise constraint can be formulated from a form of Equation (3.6) [12], and is as follows:

$$\left(\frac{T}{W}\right)_{TO} = \frac{\beta}{\alpha}\left[K_1\frac{\beta}{q}\left(\frac{W}{S}\right)_{TO} + \frac{C_{D0}}{\frac{\beta}{q}\left(\frac{W}{S}\right)_{TO}}\right] \tag{3.6}$$

where α is the thrust ratio, β is the weight ratio, q is the dynamic pressure, K_1 is the viscous drag coefficient and C_{D0} is the parasite drag coefficient for the clean configuration according to the drag polar in Sec 3.2.

3.7 Determination of Takeoff Wing Loading and Takeoff Thrust-to-Weight

We noted that high wing loading will reduce wing size while low thrust loading will allow reduced engine thrust [12]. Thus, with the performance constraint analysis for all flight conditions performed, then the highest possible wing loading and lowest possible thrust-to-weight ratio that aircraft can safely achieve are selected from the constraint diagram presented in Figure 3.1.
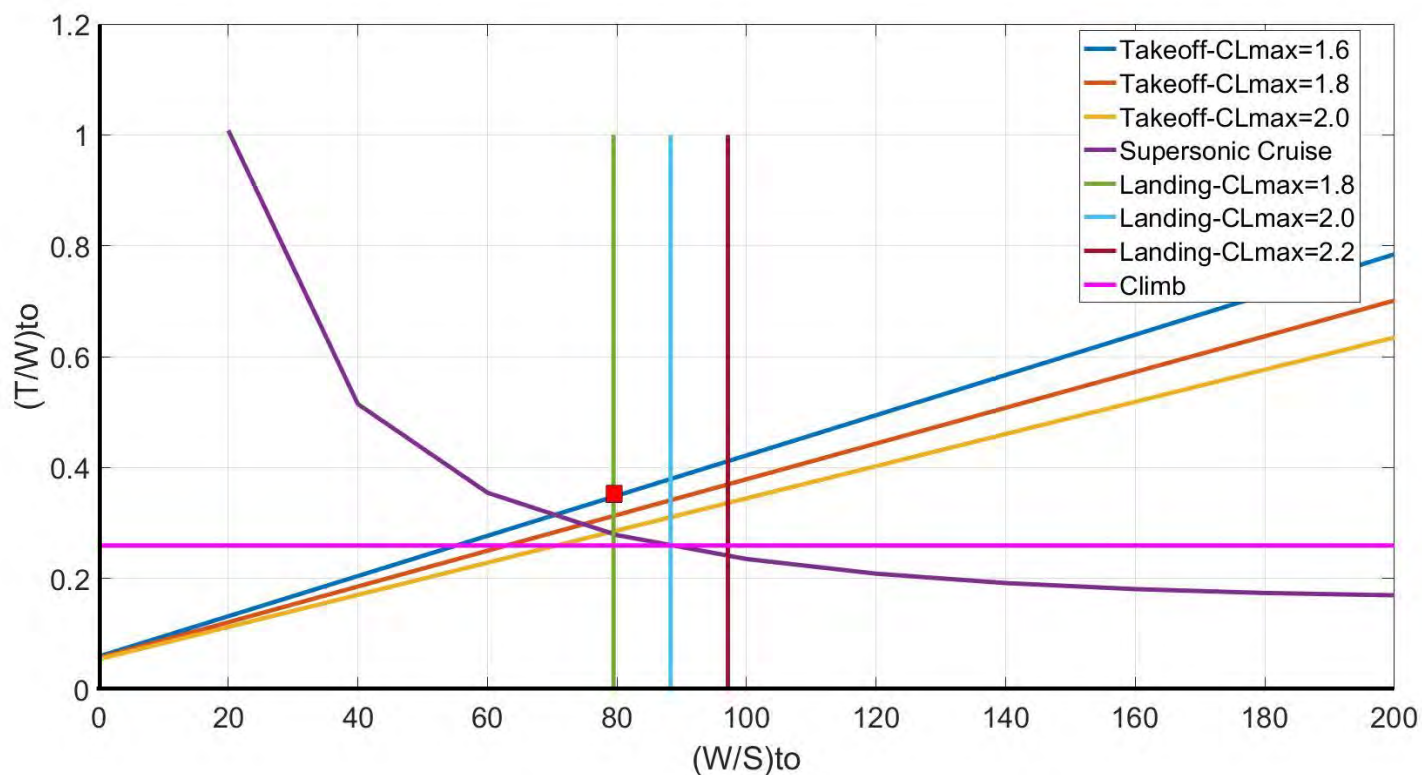
Figure 3.1 Aircraft Constraint Diagram for the Next Generation Supersonic Transport

From the constraint diagram, the next generation supersonic transport has a takeoff thrust-to-weight ratio of 0.36 and a wing loading of 79.5 lbf/ft^2, while the baseline aircraft of RFP has a takeoff thrust-to-weight ratio of 0.38 and a wing loading of 77.5 lbf/ft^2. It seems that the difference between the diagram and RFP is acceptable.

4 Mission Specification and Profile

This chapter describes the assumed mission for the next generation supersonic transport to approximate the total fuel cost required for the mission. The main mission assumed is a full-load passenger transport mission. In addition, the NOx emission of the LTO cycle and cruise would also be presented.

4.1 Mission Fuel Burn Analysis

The full-load passenger transport that the next generation supersonic transport equipped with two CJ 3000 will fly is summarized as follows:

Table 4.1 Missions of The Full-Load Passenger Transport [1]

Mission Segment	Starting Height (ft)	End Height (ft)	Time (hr)
Warm-up and Taxi	0	0	0.15
Takeoff and Climb	0	35000	/
Transonic Climb	35000	52500	/
Supersonic Cruise	52500	52500	4.36
Descend and Landing	52500	0	/

In addition, to ensure the airplane can respond to unexpected situations during the flight mission, we think the mission of the aircraft could loiter at 15000 ft with Ma 0.5 for 45 minutes should be added as mentioned above.

We begin by considering the rate at which aircraft weight is diminishing as a result of the consumption of fuel, after being rewritten and integrated, Eq. (4.1) can be applied to calculate the fuel cost [12]:

$$\frac{W_f}{W_i} = exp\{-\frac{TSFC}{V(1-u)}\left[(h_f - h_i) + \frac{V_f^2 - V_i^2}{2g_0}\right]\} \tag{4.1}$$

where g_0 is the standard conditional gravity acceleration and u is the drag-to-thrust ratio, while $TSFC$ is the installed performance. The TSFC not included in four main conditions could be estimated using Equation (4.2) [12] as follows:

$$TSFC = (0.45 + 0.54M)\sqrt{\theta} \tag{4.2}$$

where M is the Mach number and θ is dimensionless static temperature ratio of atmosphere.

While the airplane climbs ($dh \geq 0$) and accelerates ($dV \geq 0$), Eq. (4.1) will result in Eq. (4.3) to calculate the fuel cost [12].

$$\frac{W_f}{W_i} = exp\{-\frac{C_1/M + C_2}{a_{std}}[\frac{(h_f - h_i) + \frac{V_f^2 - V_i^2}{2g_0}}{1 - (C_D/C_L)(\beta/\alpha)(T/W)_{TO}}]\} \tag{4.3}$$

where a_{std} is the standard conditional sound velocity at sea level, C_1 equals 0.45 and C_2 equals 0.54 due to Eq. 4.2.

While the airplane takes off, Eq. (4.1) will result in Eq. (4.4) to calculate the fuel cost [12].

$$\frac{W_f}{W_i} = exp\{-\frac{C_1 + C_2 M}{g_0}\left(\frac{V_{TO}}{1-u}\right)\} \tag{4.4}$$

where

$$u = [\xi_{TO}\left(\frac{q}{\beta}\right)\frac{1}{(W/S)_{TO}} + \mu_{TO}]\frac{\beta}{\alpha}\frac{1}{(T/W)_{TO}} \tag{4.5}$$

where ξ_{TO} equals 0.137 due to the constraint analysis and μ_{TO} equals μ_g in Sec. 3.3.

While the airplane cruises with constant speed and altitude, Eq. (4.1) will result in Eq. (4.6) to calculate the fuel cost [12].

$$\frac{W_f}{W_i} = exp\{-\frac{C_1/M + C_2}{a_{std}}\frac{C_D}{C_L}\Delta s\} \tag{4.6}$$

where Δs is the cruise range.

While the airplane warms up engines, Eq. (4.1) will result in Eq. (4.7) to calculate the fuel cost [12].

$$\frac{W_f}{W_i} = 1 - C_1\sqrt{\theta}\frac{\alpha}{\beta}\left(\frac{T}{W}\right)_{TO}\Delta t \tag{4.7}$$

where Δt is the time of warm-up.

The additional parameters and assumptions are listed as follows:

1. The next generation supersonic transport will have a takeoff weight of 312282 lbm according to Sec. 3.1.

2. The W_f/W_i resulting from the descent from supersonic cruise altitude to loiter altitude is assumed to be ignored, which is a convention;

3. The TSFC for the landing condition is the same as for takeoff conditions, which is a conservative estimate.

From these parameters, assumptions, and the equations listed previously, the fuel consumption for the full-load passenger transport mission of the next generation supersonic transport may be calculated. The fuel consumption of the aircraft using two CJ 3000 is shown in Table 4.2 and Fig 4.1.

Table 4.2 Full-load Passenger Transport Mission Fuel Weight for CJ 3000

Segment Number	Name	Estimated Weight after Segment(lbm)	Estimated Fuel Usage(lbm)	Fuel Percent Usage	beta	Wf/Wi	Fuel Left(lbm)
0	Initial	312282	0	0	1	1	150940
1	Warm-up and Takeoff	302416.15	9865.85	6.54%	0.968407	0.968	141074.15
2	Subsonic Climb	294859.72	7556.43	5.01%	0.94421	0.975	133517.72
3	Transonic Climb	280728.44	14131.28	9.36%	0.898958	0.952	119386.44
4	Supersonic Cruise	175839.63	104888.82	69.49%	0.56308	0.626	14497.63
5	Loiter	169298.39	6541.23	4.33%	0.542133	0.963	7956.39
6	Land	164558.04	4740.35	3.14%	0.526953	0.972	3216.04
Total			147723.96	97.87%			
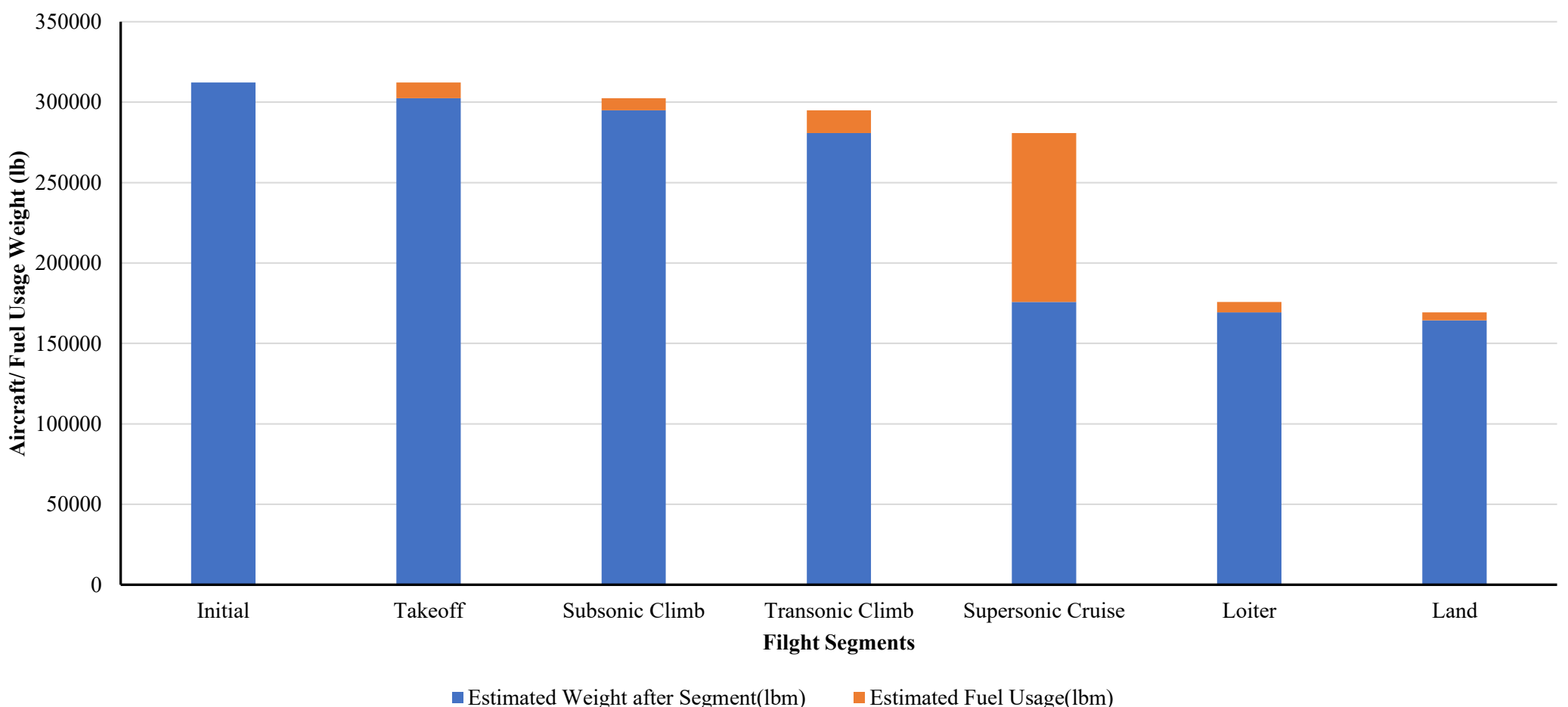
Figure 4.1 Full-load Passenger Transport Mission Fuel Weight for CJ 3000

From Table 4.2, even if adding an extra mission of loiter for 45 min, the fuel cost is still acceptable. And in general condition without loiter, the final calculated result of fuel cost is 141183 lb, saving nearly 10000 lb of fuel compared to the baseline engine. It seems that the

supersonic cruise results in the greatest fuel consumption. Hence it is sensible to choose the supersonic cruise point as the design point to ensure that the maximum fuel consumption section could have the minimum possible TSFC.

4.2 Mission NOx Emission Analysis

The RFP sets strict limits on the NOx emission of the LTO cycle and EI_{NOx} of the cruise for the next generation supersonic transport, while the NOx is known to poison mucosa of respiratory organs, result in acid rain, delete ozone and form ozone hole [14]. The emission index of NOx (EI_{NOx}) is needed to calculated NOx emissions. The EI_{NOx} could be estimated by correlation method, using Eq. (4.8) for single ring combustors [15], Eq. (4.9) for double ring combustors [16] and Eq. (4.10) for lean direct injection combustors (LDI) [17] as follows:

For single ring combustors:

$$EI_{NOx} = 0.068 \left(\frac{P_{t,in}}{6894.8}\right)^{0.5} * exp\left(\frac{T_{t,in} - 459.67}{345} + 0.0063 * 0.0027114\right) \tag{4.8}$$

For double ring combustors:

$$EI_{NOx} = 0.00754938 \left(\frac{P_{t,in}}{6894.8 * 439}\right)^{0.5} * exp\left(\frac{1.8T_{t,in} - 1471}{345}\right) * T_{t,out} \tag{4.9}$$

For LDI combustors:

$$EI_{NOx} = 1.539 \, exp\left(\frac{T_{t,in}}{194}\right) * (far_{out})^{1.69} * \left(\frac{P_{t,in}}{1000}\right)^{0.595} * \left(\frac{\Delta P_t}{P_{t,in}}\right)^{-0.565} \tag{4.10}$$

where $P_{t,in}$ is the inlet total pressure of combustor, $T_{t,in}$ is the inlet total temperature of combustor, $T_{t,out}$ is the outlet total temperature of combustor, far_{out} is the outlet fuel-to-air ratio of the combustor and $\frac{\Delta P_t}{P_{t,in}}$ is the total pressure loss coefficient of the combustor. It should be noted that the units used in Eq. (4.8), Eq. (4.9) and Eq. (4.10) follow the international system of units rather than imperial units.

After estimating the EI_{NOx} of the LTO cycle and cruise by previous equations, the NOx emission of LTO cycle could be calculated using Eq. (4.11) [1] as follows:

$$Emission \; Mass \; per \; unit \; of \; Thrust \left(\frac{g}{kN}\right) = \sum \left[EI_{NOx} \left(\frac{g}{kg \; fuel}\right) * TSFC \left(\frac{kg \; fuel}{kN \; hr}\right) * Time \; in \; Mode \; (hr)\right] \tag{4.11}$$

where $TSFC$ could be estimated by Equation (4.2) and $Time \; in \; Mode$ could be found in Table 4.3 [1] as follows:

Table 4.3 LTO Cycle Definitions

Operating Mode	Subsonic Engines		Supersonic Engines	
	Power (%)	Time in Mode (min)	Power (%)	Time in Mode (min)
Takeoff	100	0.7	100	1.2
Climb out	85	2.2	65	2.0
Descent	N/A	N/A	15	1.2
Approach	30	4.0	34	2.3
Taxi/Idle	7	26.0	3.8	26.0

The upper limit of LTO NOx emission could be calculated by Eq. (4.12) [1] as follows:

$$Allowed \; Emission \; Mass \; per \; unit \; of \; Thrust \left(\frac{g}{kN}\right) = 36.0 + 2.42OPR \tag{4.12}$$

From these parameters and the equations listed previously, the NOx emission for the LTO cycle and EI_{NOx} for the cruise of the next generation supersonic transport may be calculated. The NOx parameters about the aircraft using two CJ 3000 is shown in Table 4.4.

Table 4.4 NOx Emission of LTO Cycle and EI_{NOx} of Cruise

NOx Generating Section	Combustor Type	NOx Emission/Index	Upper Limit	Margin
NOx emission of LTO Cycle (g/kN)	Single Ring Combustor	151.46		-1.65%
	Double Ring Combustor	516.72	154	+235.53%
	LDI Combustor	30.81		-80.00%
EI_{NOx} of cruise (g/kg)	Single Ring Combustor	5.99		+19.8%
	Double Ring Combustor	36.34	5	+626.8%
	LDI Combustor	1.27		-74.6%

It can be seen that by using LDI combustor, great margins over 74% of NOx emission/index would be obtained, which would allow CJ 3000 to serve longer while the international limit of NOx emission/index would be more and more strict. More reasons of choosing LDI as the combustor of CJ 3000 will be discussed in section 7.3 in detail.

5 Engine Inlet Design

The inlet of a gas turbine engine is used to inhale the air from the outside, supply the air to the engine and decelerate and pressurized the airstream at a higher Maher number. The inlet must complete the deceleration and pressurization of the free air flow with the smallest total pressure loss. In all flight conditions and engine working conditions, the pressurization process of the intake port should avoid

excessive time and air inhomogeneity in order to reduce the risk of fan or compressor surge and blade flutter. In addition, the inlet resistance should be as small as possible. To enable efficient supersonic cruise, a preliminary design of the inlet is necessary.

5.1 Inlet Form selection

When the Mach number of the supersonic aircraft is large, the subsonic inlet will have a strong bowing shock wave, which will lead to the low recovery coefficient of the total pressure and the great loss of the thrust of the engine. The Maher number of the CJ 3000 is 1.6. Therefore, the supersonic inlet should be adopted. The supersonic inlet can be roughly divided into three types: external compression inlet, internal compression inlet and mixed compression inlet.

The supersonic compression process of the external compression inlet is carried out outside the inlet, and a normal shock wave is generated at the inlet. As the flight Mach number increases, in order to ensure high total pressure recovery coefficient, the number of oblique shock waves increases and the corresponding turning angle of the airflow increases, which makes the windward area of the inlet increases and causes greater resistance.

The internal compression inlet, in the ideal condition, causes the supersonic flow to flow directly into the inlet, decelerate in the contraction section, reach the sound speed in the throat, and become subsonic in the expansion section, like a reverse convergent-divergent nozzle. However, the internal compression inlet has serious starting problems

The mixed compression inlet has external compression process and internal compression process. Compared with the external compression inlet, the inlet resistance decreases. Compared with the internal compression inlet, the serious starting problem has been improved. Therefore, according to the above analysis, CJ3000 should use mixed compression inlet.
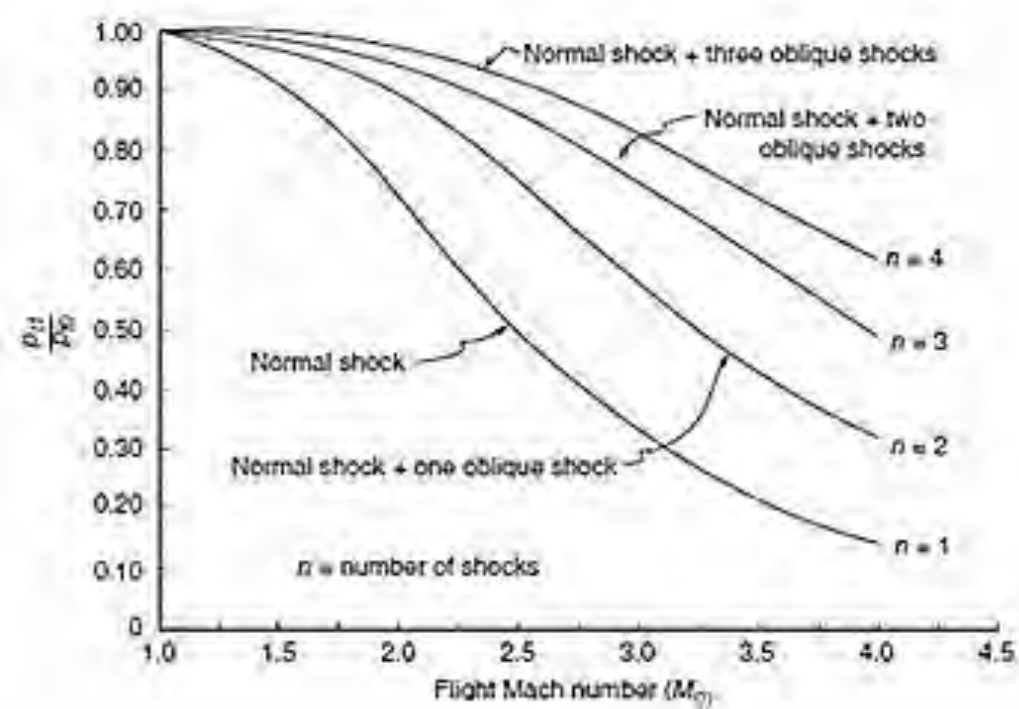
Figure 5.1 Total Pressure Recovery Coefficient

| Figure 5.2 external compression inlet | Figure 5.3 Internal compression | Figure 5.4 Inlet Mixed compression inlet |
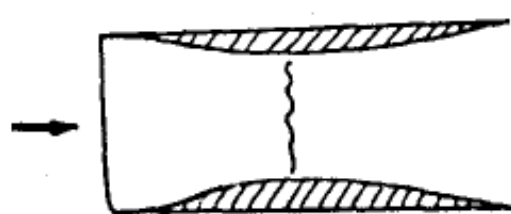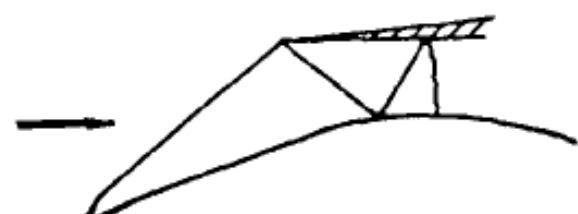
5.2 Inlet Conditions

Table 5.1 Inlet Conditions of Inlet

Parameter	Transonic Point	Supersonic Cruise
Engine Mass Flow(lb/s)	674.317	664.65
Atmospheric Pressure (psia)	2.649	1.492
Atmospheric Pressure ($°R$)	389.97	389.97

5.3 Inlet Sizing and Performance

The structure of the intake port is shown in Figure 5.5.
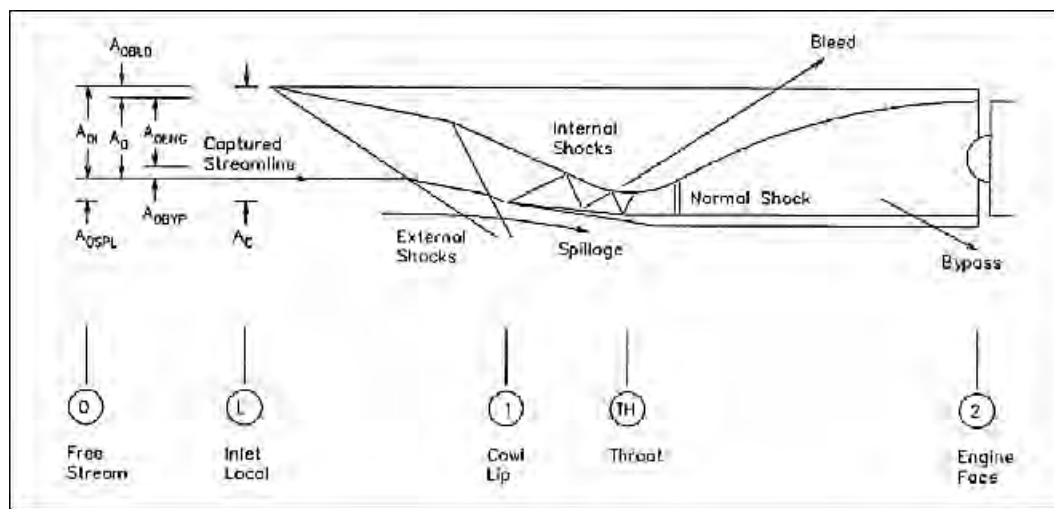
Figure 5.5 Inlet Airflow Accounting

5.3.1 Main calculation procedure

(1) Supersonic Cruise

The initial calculation of intake port is based on the calculation method mentioned in RFP.

Read the matched (design) mass flow ratio $(\frac{A_0}{A_C})_{des}$ from Table 5.5, $(\frac{A_0}{A_C})_{des} = 0.8175$

There is no bypass air at the design point. $A_{0,des} = \frac{W_{ENG}}{\rho V} = 3.836 \ m^2$

Compute the required capture area, $A_C = \frac{A_{0,des}}{(\frac{A_0}{A_C})_{des}} = 4.6923 \ m^2$

Read the matched inlet recovery from Table 5.4. Inlet recovery is 0.9543.

Read the matched bleed flow ratio from Table 5.9. $\frac{A_{OBLD}}{A_C} = 0.029$

Compute the inlet demand flow. $W_{0I} = \rho V \left(\frac{A_0}{A_C} + \frac{A_{OBLD}}{A_C}\right) A_C = 312.174 \ \text{kg/s}$

Read the coefficients of spillage drag, bleed drag, and bypass drag from Tables 5.6, 5.7, and 5.8, respectively. At design point, $C_{d,spill}$ and $C_{d,bypass}$ are equal to 0.

Compute the inlet drag $D_{inlet} = \left(C_{d,spill} + C_{d,bleed} + C_{d,bypass}\right)\frac{1}{2}\rho V^2 A_C = 2350.4 \ N$

(2) Transonic Point

Once the capture area is known, the inlet transonic performance may be calculated as follows

Calculate the capture mass flow, $W_C = \rho V A_C = 459.065 \ \text{kg/s}$

Calculate the engine area ratio, $\frac{A_{0ENG}}{A_C} = \frac{W_{ENG}}{W_C} = 0.6663$

Read the bypass area ratio from Table 10, $\frac{A_{0bypass}}{A_C} = 0.04$

Calculate the bypass mass flow, $W_{BYP} = \frac{A_{0ENG}}{A_C}W_C = 18.363 \text{kg/s}$

Calculate the mass flow at the inlet throat, $W_0 = W_{ENG} + W_{BYP} = 324.228 \ \text{kg/s}$

Calculate the area ratio, $\frac{A_0}{A_C} = \frac{W_0}{W_C} = 0.7063$

Read the inlet recovery from Table 5.3

Read the bleed area ratio from Table 5.9, $\frac{A_{0BLD}}{A_C} = 0.022$

Calculate the bleed mass flow, $W_{BLD} = 10.099 \ \text{kg/s}$
Calculate the inlet demand mass flow, $W_I = W_0 + W_{BLD} = 334.327 \ \text{kg/s}$

Calculate the inlet demand area ratio, $\frac{A_{0I}}{A_C} = \frac{W_I}{W_C}$

Read the coefficients of spillage drag, bleed drag, and bypass drag from Tables 5.6, 5.7, and 5.8, respectively. $C_{d,spill} = 0.005$ and $C_{d,bleed} = 0.0255$ and $C_{d,bypass} = 0.038$

Compute the inlet drag $D_{inlet} = \left(C_{d,spill} + C_{d,bleed} + C_{d,bypass}\right)\frac{1}{2}\rho V^2 A_C = 5237.9 \ N$

Table 5.2 Ramp Angles & Inlet Output

Mix Compression Inlet			
M1		1.6	
1st Oblique Shock		2nd Oblique Shock	
$\theta 1$	4.0	$\theta 2$	8
$\beta 1$	42.93	$\beta 2$	55.52
M2	1.464	M3	1.146
Pt1 / Pt0	0.9992	Pt2 / Pt1	0.9928

Since the speed of flight at takeoff is low, the inlet resistance at takeoff is ignored. CJ 3000 inlet is selected as a 2-dimensional which

more suitable for supersonic and more easily to produce. There are two oblique shock waves in the external compression process of the mixed compression inlet. There are a series of oblique shock waves in the internal compression process of the mixed compression inlet. Then a normal shock occurs in downstream of the throat. After the normal shock, air goes through the transition section.
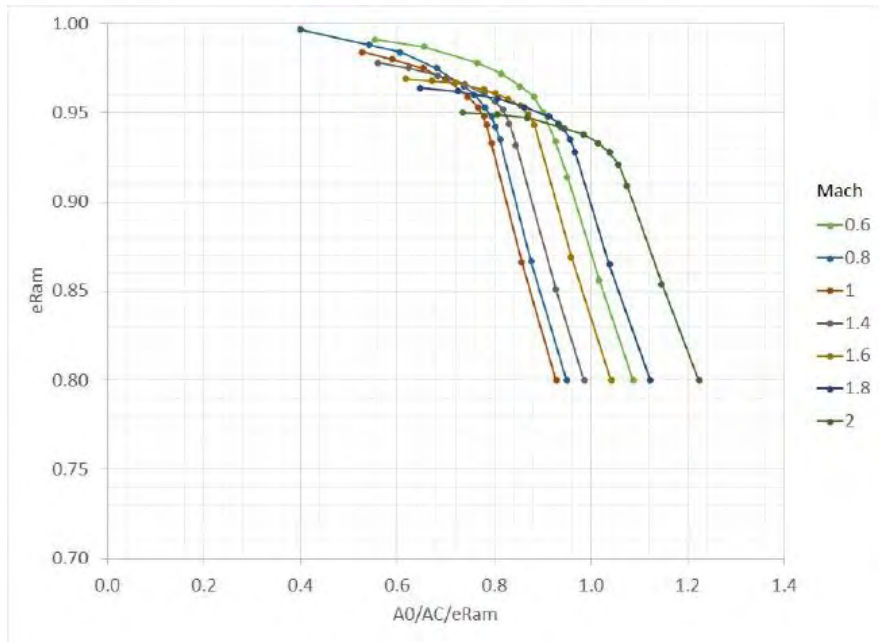
Table 5.3 Inlet Recovery
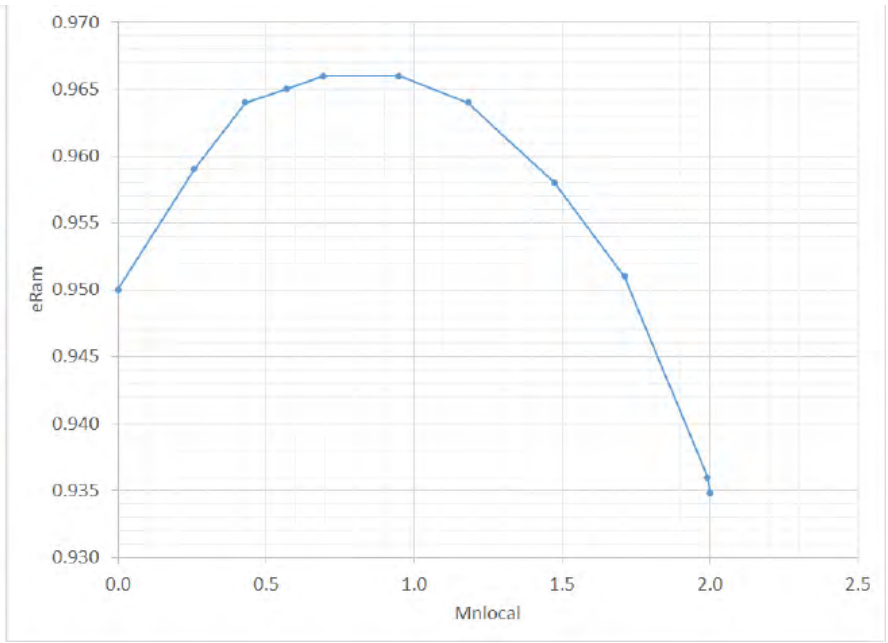
Table 5.4 Matched Inlet Recovery
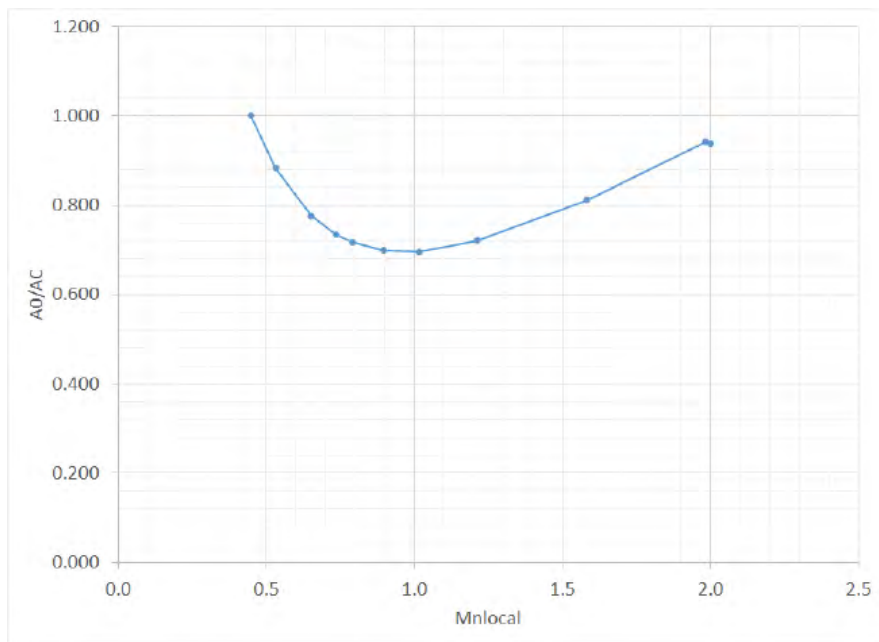
Table 5.5 Matched Inlet Mass Flow Ratio
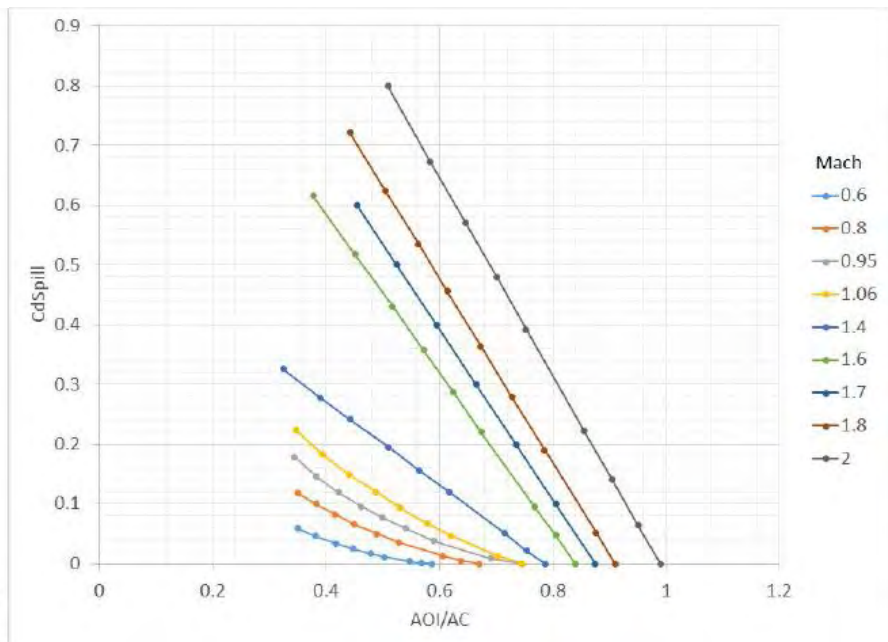
Table 5.6 Spillage Drag Coefficient
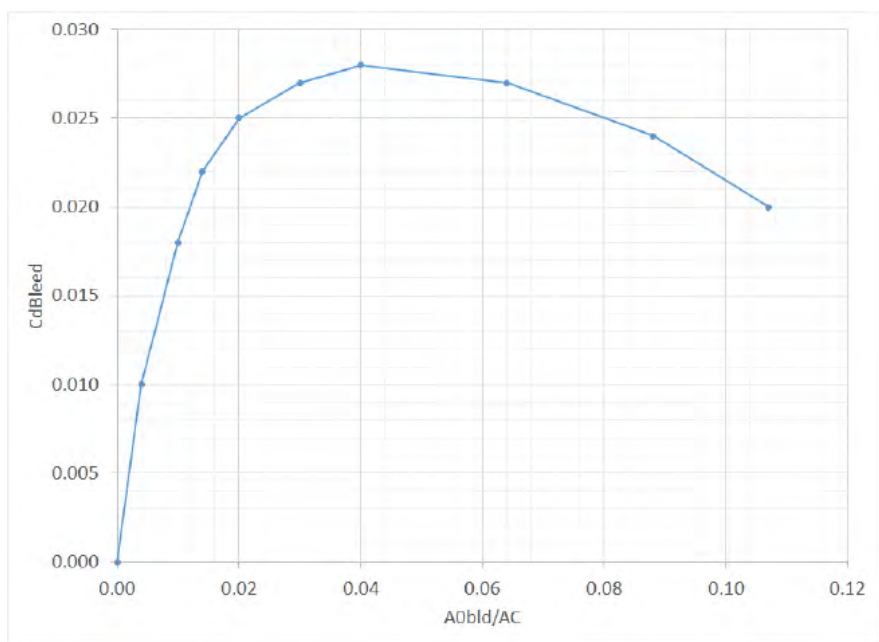
Table 5.7 Inlet Bleed Drag Coefficient
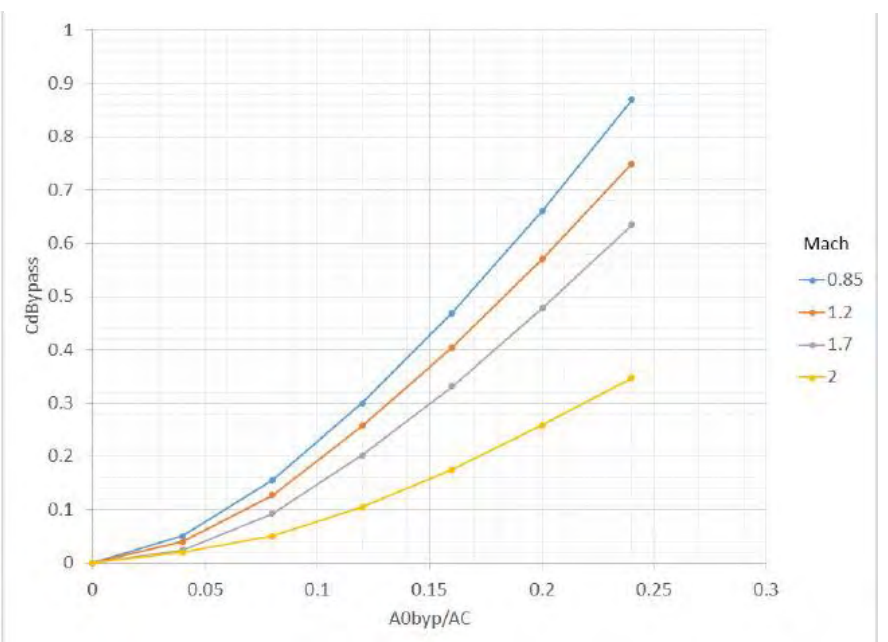
Table 5.8 Inlet Bypass Drag Coefficient
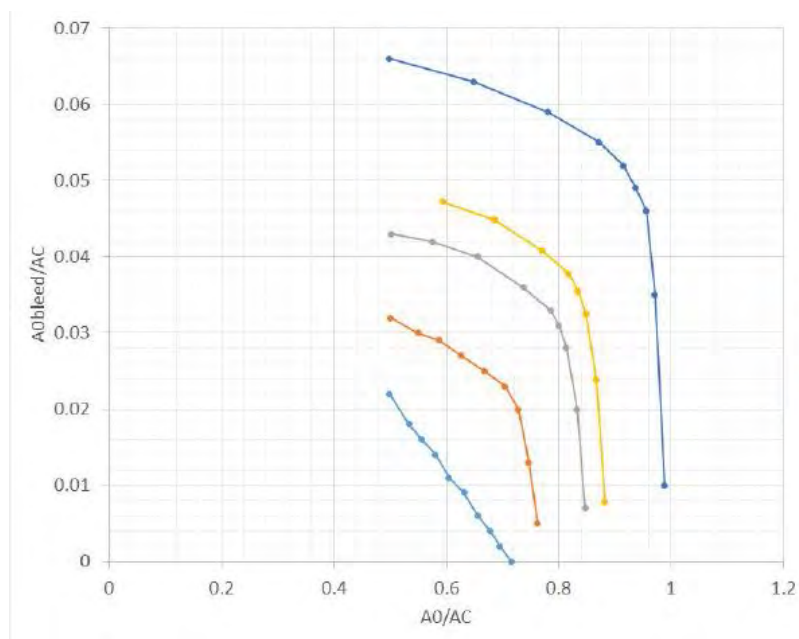
| Table 5.9 Inlet Bleed Mass Flow Ratio | Table 5.10 Inlet Bypass Mass Flow Ration |
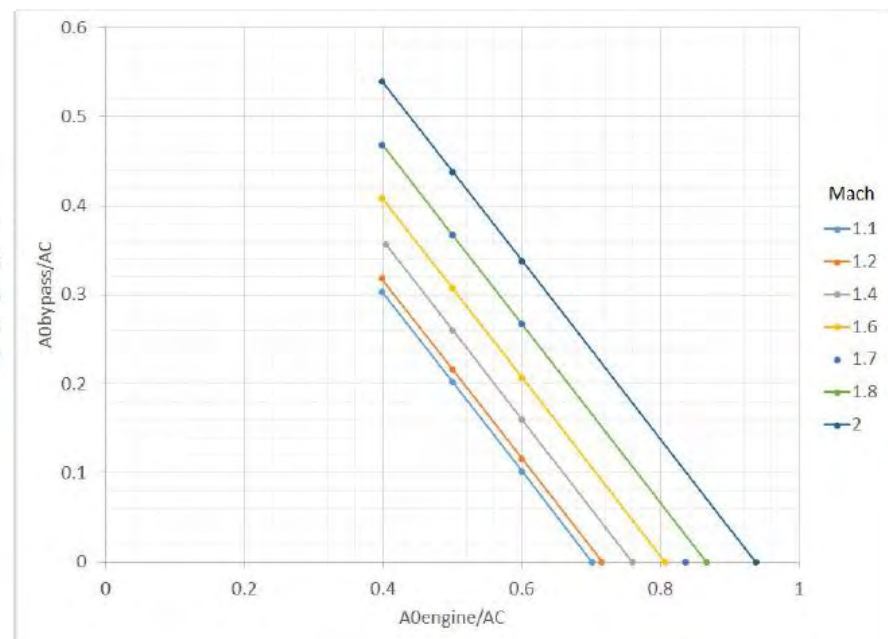
5.3.2 Two-dimensional sketches of the inlet

Draw the following two-dimensional inlet sketches in Fig. 5.6 based on the calculated data. The unit of length in Fig. 5.6 is millimeter. The three-dimensional model is shown in Figure 13.
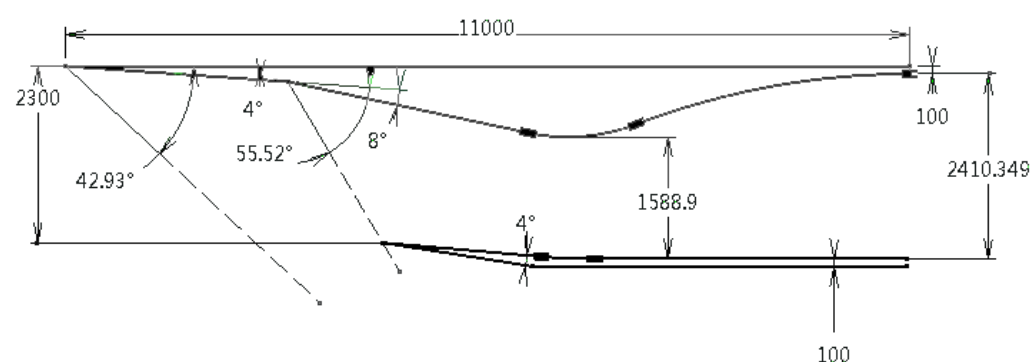
Figure 5.6 2D Sketches of the Inlet
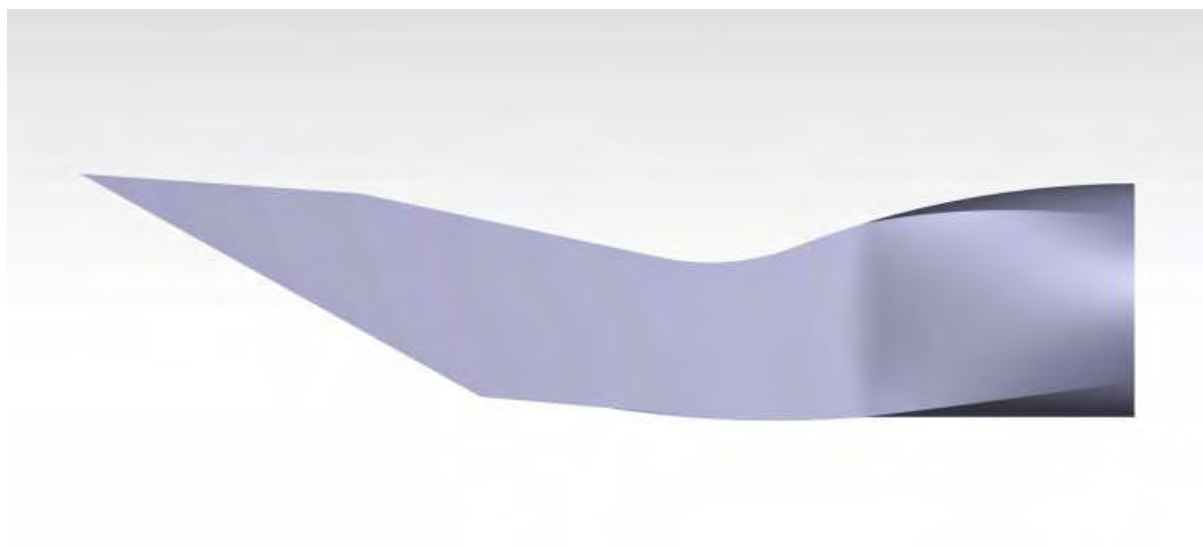
Figure 5.7 3D Sketches of the Inlet

6 Aerodynamic Design of Turbomachinery System

A turbomachinery design system generally consists of the following steps. Firstly, specify overall parameters such as mass flow rate, mean diameter, rotational speed, inlet flow conditions, exit pressure. Secondly, perform a one-dimensional mean-line calculation to obtain the annulus shape and mid-span blade angles. Thirdly perform a 2D axisymmetric throughflow calculation in the inverse (design) mode to obtain the variation of flow angles along the span. Then, repeat the throughflow calculation in the analysis mode to predict the blade losses, machine efficiency and stream surface thickness distributions. After that, perform quasi-3D (Q3D) blade-to-blade calculations at several spanwise sections on each blade row to design the blade shapes. Finally, perform more detailed 3D calculations to include the effects of leakage flows endwall bleeds and cavities and coolant flows. These will give the final prediction of machine overall performance.

In fact, this process is relatively slow and complicated. So, in this case, we use the AXIAL software in the Concepts-NREC engineering design system. Due to time constraints, three-dimensional numerical calculation is not possible. However, one dimensional calculation results largely determine the final performance of the compressor, so the one-dimensional efficiency is reasonable as a prediction.

6.1. Fan Design Requirement

The inlet conditions corresponding to the fan design are as follows. The design point is supersonic cruise state.

Table 6.1 Inlet Condition of Fan

Parameter	Value
Total Pressure, P_{t1} (psia)	6.078
Total Temperature, T_{t1} (°R)	589.81
Static Pressure, P_1 (psia)	5.0365
Static Temperature, T_1 (°R)	559.24

The specific requirements for the fan are as follows:

Table 6.2 Requirements of Fan

Parameter	Value
Total pressure ratio, πf	2.44
Adiabatic efficiency, ηf	88%
Air Mass Flow, m (lb/s)	664.647

6.1.1 Selection of Parameters

Table 6.3 Design parameters of Fan

Parameter	Value
Number of stage	2
Average flow coefficient	0.5
Total to static pressure ratio, PRts	2.11
Air Mass Flow (lb/s)	664.647
Shaft rotational speed	4000
Total Temperature (°R)	589.91
Total Pressure (psia)	6.078
Inlet angle	0
Outlet angle	0
Flow path	Constant mean diameter
Blade configuration features	Various Sections

According to the results of thermodynamic cycle analysis, the total pressure ratio of the fan is 2.44. A multistage fan is taken to satisfy the high efficiency. Considering the development of fan design technology, two stage fans are selected. The recommended average flow coefficient value of high performance compressor is between 0.4 and 0.6. In this case, 0.5 is reasonable. The fan speed of Trent1000 is about 3000 rpm. Because of the increase of the average stage pressure ratio, the fan of CJ 3000 increases the speed to 4000 rpm. For civil aircraft, the flight environment is relatively stable. Therefore, there is no fan inlet guide vane. Taking into account the high average stage pressure ratio and high efficiency, the constant mean diameter is selected. Because of the long blade, it is necessary to adapt to different directions at different heights.

6.1.2 Fan Design Output

Table 6.4 Guidelines on the Range of Turbomachinery Parameters [27]

Parameter	Range of Values	Typical Value
Flow Coefficient, φ	$0.3 \leq \varphi \leq 0.9$	0.6
D-Factor	$D \leq 0.6$	0.45
Axial Mach Number, M_z	$0.3 \leq M_z \leq 0.6$	0.55
Tip Tangential Mach Number, M_T	$1.0 \leq M_T \leq 1.5$	1.3
Degree of Reaction, $\mathbb{R}$	$0.1 \leq °R \leq 0.9$	0.5 (for M < 1)
Reynolds Number Based on Chord	$300,000 \leq Re_c$	> 500,000
Tip Relative Mach Number (1st Stage)	$(M_{1r})_{tin} \leq 1.7$	1.3-1.5
Stage Average Solidity	$1.0 \leq \sigma \leq 2.0$	1.4
Stage Average Aspect Ratio	$1.0 \leq AR \leq 4.0$	< 2.0
Polytropic Efficiency, e_c	$0.85 \leq e_c \leq 0.92$	0.9
Loading Coefficient, ψ	$0.2 \leq \psi \leq 0.5$	0.35
DCA Blade (Range)	$0.8 \leq M \leq 1.2$	Same
NACA-65 Series (Range)	$M \leq 0.8$	Same
De Haller Criterion	$W_2/W_1 \geq 0.72$	0.75
Blade Leading-Edge Radius	r_{LE} ~5-10% of t_{max}	5% t_{max}
Compressor Pressure Ratio per Spool	$\pi_c \leq 20$	Up to 20
Axial Gap Between Blade Rows	$0.23c_z$ to $0.25c_z$	$0.25c_z$
Aspect Ratio, Fan	~2-5	< 1.5
Aspect Ratio, Compressor	~1-4	~2

The output results and velocity triangles are detailed in Appendix B. Comparing the output results with the design criteria, most of all parameters are within the recommended range. Among them, De Haller is slightly lower than the lower limits of the recommended range. Efficiency meets the requirements. Therefore, the design of the fan is acceptable.

6.1.3 Fan Flow Path
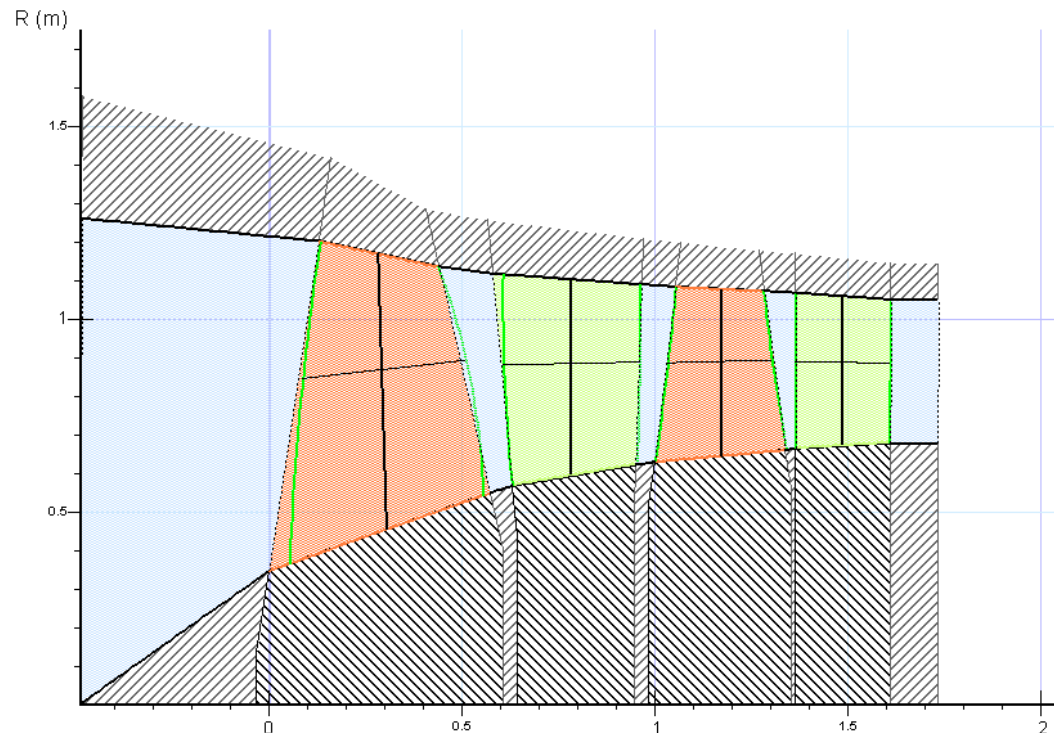
Figure 6.1 2D Sketches of the Fan

6.2. IPC Design Requirement

The inlet conditions corresponding to the IPC design are as follows. The design point is supersonic cruise state.

Table 6.5 Inlet Condition of IPC

Parameter	Value
Total Pressure, P_{t1} (psia)	14.831
Total Temperature, T_{t1} (°R)	782.82
Static Pressure, P_1 (psia)	12.9380
Static Temperature, T_1 (°R)	753.14

The specific requirements for the IPC are as follows

Table 6.6 Requirements of IPC

Parameter	Value
Total pressure ratio, πf	4.839
Adiabatic efficiency, ηf	88%
Air Mass Flow, m (lb/s)	177.238

6.2.1 Selection of Parameters

Table 6.7 Design parameters of IPC

Parameter	Value
Number of stage	5
Average flow coefficient	0.48
Total to static pressure ratio, PRts	4.45
Air Mass Flow (lb/s)	177.238
Shaft rotational speed	7800
Total Temperature (°R)	782.82
Total Pressure (psia)	14.831
Inlet angle	0
Outlet angle	0
Flow path	Constant mean diameter
Blade configuration features	Various Sections

According to the results of thermodynamic cycle analysis, the total pressure ratio of IPC is 4.839. The initial estimate of the number of stages is five. In this case, average stage pressure ratio is 1.37, which is acceptable. The recommended average flow coefficient value of high performance compressor is between 0.4 and 0.6. In this case, 0.48 is reasonable. IPC speed reference Trent 1000, set for 7800 rpm. Taking into account the high average stage pressure ratio and high efficiency, the constant mean diameter is selected. And it is necessary to adapt to different directions at different heights.

6.2.2 IPC Design Output

The output results and velocity triangles are detailed in Appendix B. Comparing the output results with the design criteria, most of all parameters are within the recommended range. Among them, De Haller in some locations is slightly lower than the lower limits of the recommended range. Efficiency meets the requirements. Therefore, the design of IPC is acceptable.

6.2.3 IPC Flow Path
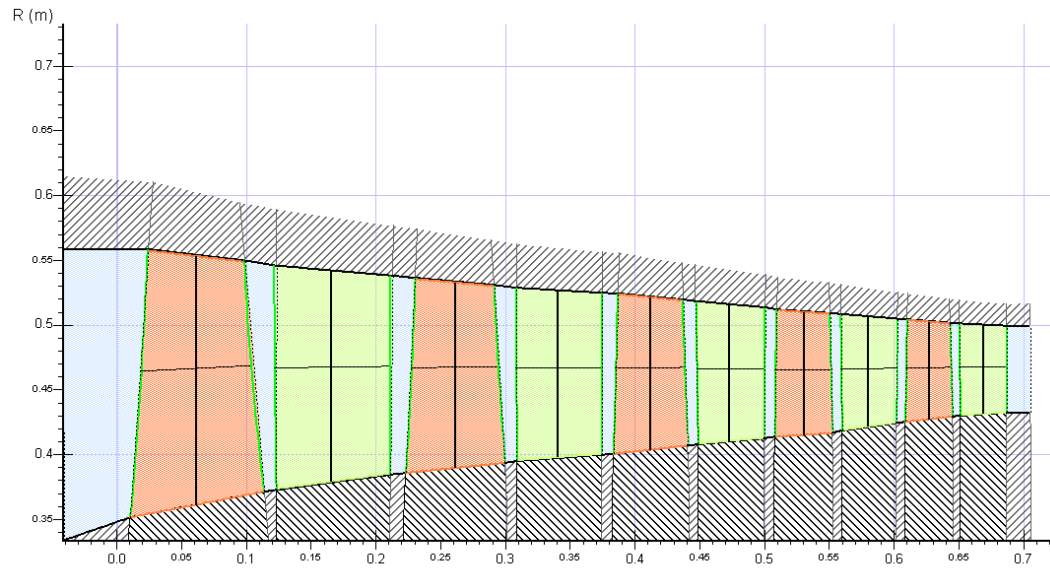
Figure 6.2 2D Sketches of the IPC

6.3 HPC Design Requirement

The inlet conditions corresponding to the HPC design are as follows. The design point is supersonic cruise state.

Table 6.8 Inlet Condition of HPC

Parameter	Value
Total Pressure, P_{t1} (psia)	71.048
Total Temperature, T_{t1} (°R)	1266.84
Static Pressure, P_1 (psia)	64.179
Static Temperature, T_1 (°R)	1230.89

The specific requirements for the HPC are as follows

Table 6.9 Requirements of HPC

Parameter	Value
Total pressure ratio, πf	3.85
Adiabatic efficiency, ηf	88%
Air Mass Flow, m (lb/s)	177.238

6.3.1 Selection of Parameters

Table 6.10 Design parameters of HPC

Parameter	Value
Number of stage	4
Average flow coefficient	0.4
Total to static pressure ratio,PRts	3.6
Air Mass Flow (lb/s)	177.238
Shaft rotational speed	12000
Total Temperature (°R)	1266.84
Total Pressure (psia)	71.048
Inlet angle	0
Outlet angle	0
Flow path	Constant mean diameter
Blade configuration features	Various Sections

According to the results of thermodynamic cycle analysis, the total pressure ratio of HPC is 3.85. The initial estimate of the number of stages is four. In this case, average stage pressure ratio is 1.4, which is acceptable. The recommended average flow coefficient value of high performance compressor is between 0.4 and 0.6. In this case, 0.4 is reasonable. HPC speed reference Trent 1000, set for 12000 rpm. Taking into account the high average stage pressure ratio and high efficiency, the constant mean diameter is selected. And it is necessary to adapt to different directions at different height.

6.3.2 HPC Design Output

The output results are detailed in Appendix B. Comparing the output results with the design criteria, most of all parameters are within the recommended range. Among them, De Haller in some locations is slightly lower than the lower limits of the recommended range. Efficiency meets the requirements. Therefore, the design of the HPC is acceptable.

6.3.3 HPC Flow Path
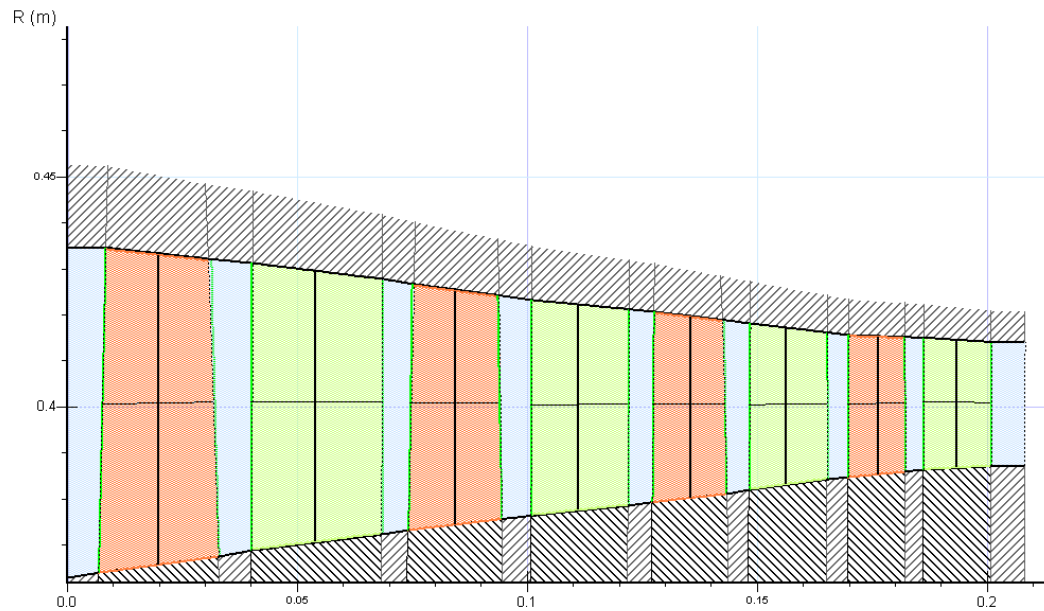
Figure 6.3 2D Sketches of the HPC

6.4. HPT Design Requirement

The inlet conditions corresponding to the HPT design are as follows. The design point is supersonic cruise state.

Table 6.11 Inlet Condition of HPT

Parameter	Value
Total Pressure, P_{t1} (psia)	262.019
Total Temperature, T_{t1} (°R)	3273.62
Static Pressure, P_1 (psia)	245.807
Static Temperature, T_1 (°R)	3214.96

The specific requirements for the HPT are as follows

Table 6.12 Requirements of HPT

Parameter	Value
Total pressure ratio, πf	2.339
Adiabatic efficiency, ηf	92%
Air Mass Flow, m (lb/s)	177.044

6.4.1 Selection of Parameters

Table 6.13 Design parameters of HPT

Parameter	Value
Number of stage	1
Average flow coefficient	0.6
Total to static pressure ratio, PRts	2.75
Air Mass Flow (lb/s)	177.044
Shaft rotational speed	12000
Total Temperature (°R)	3273.62
Total Pressure (psia)	262.019
Inlet angle	0
Outlet angle	0
Flow path	Constant mean diameter
Blade configuration features	Various Sections

According to the results of thermodynamic cycle analysis, the total pressure ratio of the HPT is 2.339. Because high pressure turbine has strong working ability and turbine technology is mature, single stage high pressure turbine is selected. The recommended average flow coefficient value of high performance compressor is between 0.5 and 0.65. In this case, 0.6 is reasonable. The speed of HPT is the same as that of HPC. Taking into account the high efficiency, the constant mean diameter is selected. And it is necessary to adapt to different directions at different height.

6.4.2 HPT Design Output

The output results and velocity triangles are detailed in Appendix B. Comparing the output results with the design criteria, most of all parameters are within the recommended range. Efficiency meets the requirements. Therefore, the design of the HPT is acceptable.

6.4.3 HPT Flow Path
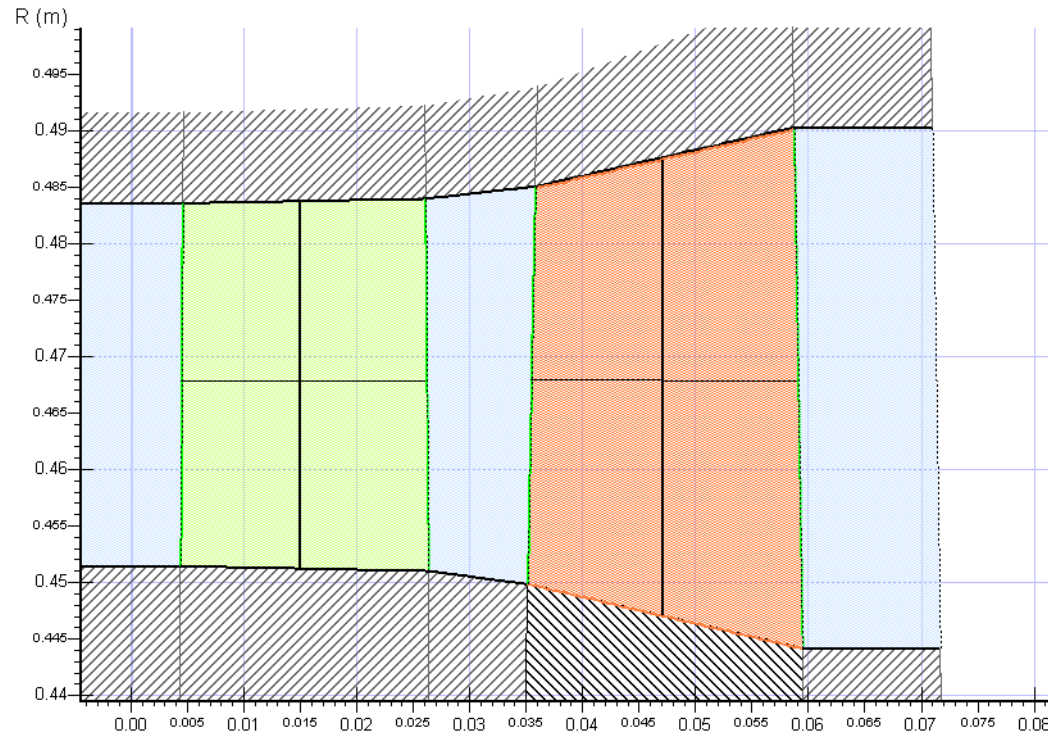
Figure 6.4 2D Sketches of the HPT

6.5. IPT Design Requirement

The inlet conditions corresponding to the IPT design are as follows. The design point is supersonic cruise state.

Table 6.14 Inlet Condition of IPT

Parameter	Value
Total Pressure, P_{t1} (psia)	111.411
Total Temperature, T_{t1} (°R)	2714.33
Static Pressure, P1 (psia)	102.003
Static Temperature, T_1 (°R)	2647.37

The specific requirements for the IPT are as follows

Table 6.15 Requirements of IPT

Parameter	Value
Total pressure ratio, πf	2.106
Adiabatic efficiency, ηf	92%
Air Mass Flow, m (lb/s)	181.418

6.5.1 Selection of Parameters

Table 6.16 Design parameters of IPT

Parameter	Value
Number of stage	1
Average flow coefficient	0.77
Total to static pressure ratio,PRts	2.11
Air Mass Flow (lb/s)	181.418
Shaft rotational speed	7800
Total Temperature (°R)	2714.33
Total Pressure (psia)	111.411
Inlet angle	0
Outlet angle	0
Flow path	customized diameter
Blade configuration features	Various Sections

According to the results of thermodynamic cycle analysis, the total pressure ratio of the HPT is 2.11. Single stage IPT is selected. The recommended average flow coefficient value of high performance compressor is between 0.65 and 0.9. In this case, 0.77 is reasonable. The speed of IPT is the same as that of IPC. Taking into account flow path transition, the customized diameter is selected. And it is necessary to adapt to different directions at different height.

6.5.2 IPT Design Output

The output results and velocity triangles are detailed in Appendix B. Comparing the output results with the design criteria, most of all parameters are within the recommended range. Efficiency meets the requirements. Therefore, the design of the IPT is acceptable.

6.5.3 IPT Flow Path
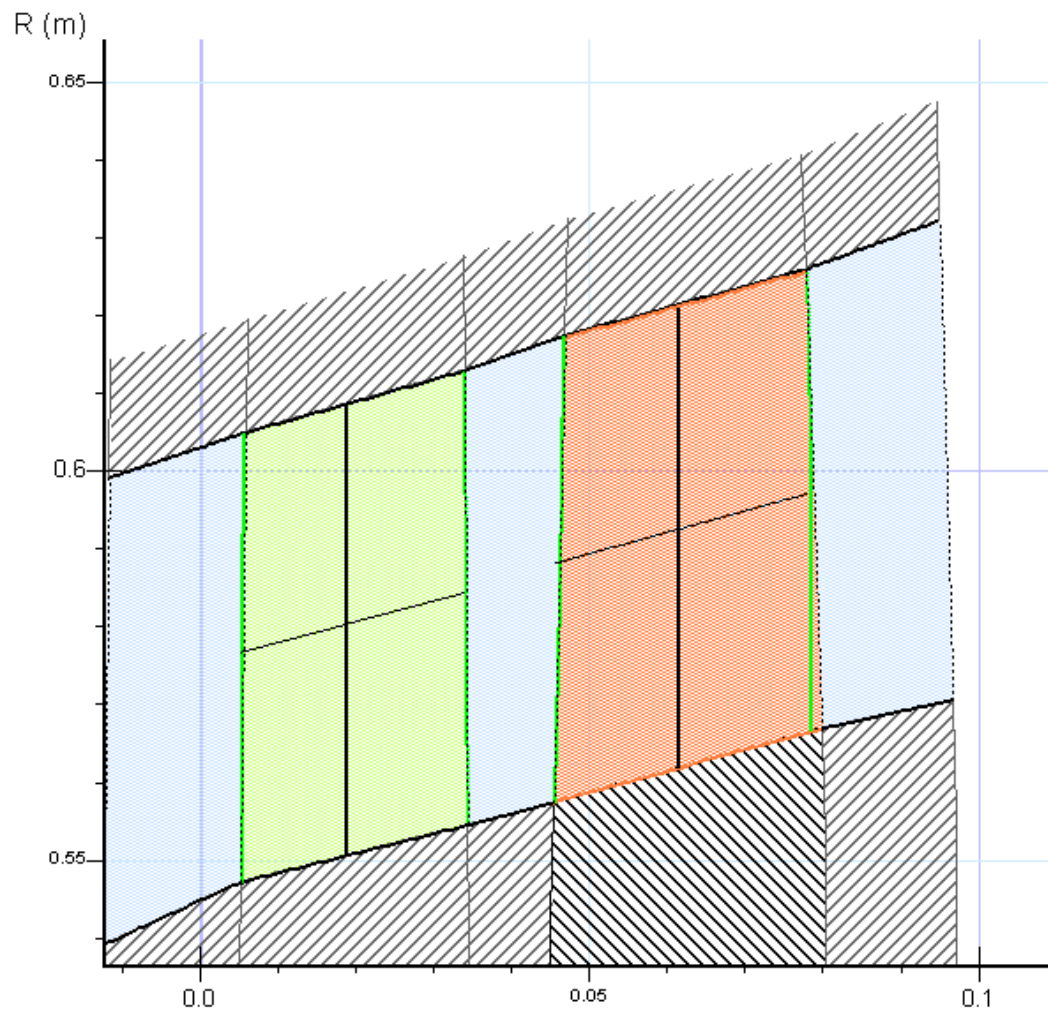
Figure 6.5 2D Sketches of the IPT

6.6 LPT Design Requirement

The inlet conditions corresponding to the LPT design are as follows. The design point is supersonic cruise state.

Table 6.17 Inlet Condition of LPT

Parameter	Value
Total Pressure, P_{t1} (psia)	52.593
Total Temperature, T_{t1} (°R)	2318.87
Static Pressure, P_1 (psia)	49.590
Static Temperature, T_1 (°R)	1828.17

The specific requirements for the LPT are as follows

Table 6.18 Requirements of LPT

Parameter	Value
Total pressure ratio, πf	3.935
Adiabatic efficiency, ηf	92%
Air Mass Flow, m (lb/s)	181.418

6.6.1 Selection of Parameters

Table 6.19 Design parameters of LPT

Parameter	Value
Number of stage	4
Average flow coefficient	0.9
Total to static pressure ratio, PRts	4.52
Air Mass Flow (lb/s)	181.418
Shaft rotational speed	4000
Total Temperature (°R)	2318.87
Total Pressure (psia)	52.593
Inlet angle	0
Outlet angle	0
Flow path	Constant mean diameter
Blade configuration features	Various Sections

According to the results of thermodynamic cycle analysis, the total pressure ratio of the LPT is 3.935. Because of low speed, multistage low-pressure turbine is chosen. The recommended average flow coefficient value of high performance compressor is between 0.9 and 1.0. In this case, 0.90 is reasonable. The speed of LPT is the same as that of Fan. Taking into account the high efficiency, the constant mean diameter is selected. And it is necessary to adapt to different directions at different height.

6.6.2 LPT Design Output

The output results and velocity triangles are detailed in Appendix B. Comparing the output results with the design criteria, most of all parameters are within the recommended range. Efficiency meets the requirements. Therefore, the design of the LPT is acceptable.

6.6.3 LPT Flow Path
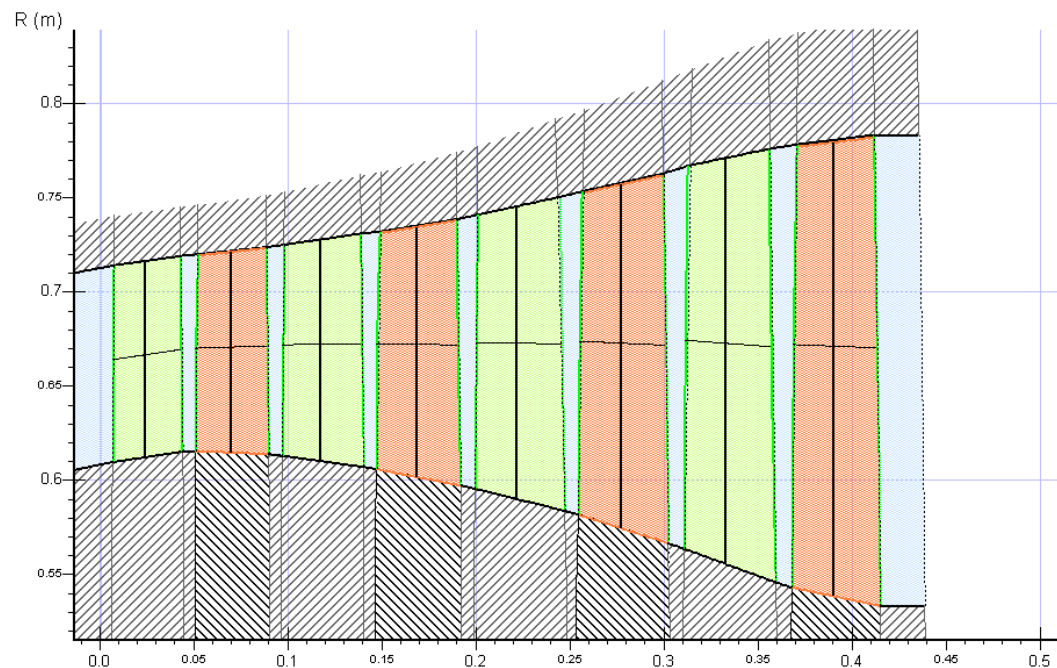
Figure 6.6 2D Sketches of the LPT

6.7 Turbomachinery Flow Path and 3D model

The Figures of turbomachinery flow path and 3D model are too huge to be placed here. Hence, the flow path and 3D model placed in Appendix B. See details.

7 Combustor System Design

The CJ 3000 utilizes an annular combustion chamber to easily match the aerodynamic layout with the outlet flow of the compressor and reduce pressure loss [14], which also follows the practices of modern commercial aircraft engines such as the GE90, CFM-56, GEnx and Trent900.

In addition to annular design, the CJ 3000 will use the Lean Direct Injection (LDI) combustor configuration to address the issue of NOx emissions. The LDI concept is a reliable approach with many advantages in meeting the combustion system requirements, such as short length, little smoke production, no spontaneous combustion and backfiring. The performance advantages of this concept will be discussed in detail in Section 7.3.

7.1 Design Point Selection

The design point of cycle analysis (supersonic cruise) is chosen as the design point of combustor as well for the turbine entry temperature of the point is the highest of all the mission. Combustor inlet condition of the design point is quoted from the cycle design and compressor design and listed in Table 7.1.

Table 7.1 Combustor Inlet Condition

Parameter	Symbols	Value	Units	Source
Total Temperature at Inlet	$T_{t,3}$	1866.31	°R	Cycle Design
Static Temperature at Inlet	$T_{s,3}$	1828.43	°R	Compressor Design
Total Pressure at Inlet	$P_{t,3}$	273.54	psia	Cycle Design
Static Pressure at Inlet	$P_{s,3}$	256.51	psia	Compressor Design
Velocity at Inlet	V_3	680.12	ft/s	Compressor Design
Mach Number at Inlet	Ma_3	0.32	/	Compressor Design
Air Mass Flow Rate at Inlet	W_3	169.26	lb/s	Cycle Design
Air Mass Flow Rate at Outlet	W_4	173.44	lb/s	Cycle Design
Air Density at Inlet	ρ_3	0.34	lb/ft^3	Compressor Design
Fuel-to-Air Ratio at Outlet	far_4	0.025	/	Cycle Design

7.2 Pre-Diffuser Design

Compressor outlet axial flow velocity of as high as 680 ft/s (M = 0.32) must be ideally reduced within a short axial distance before combustion commences. This flow deceleration is accomplished by employing a diffuser between the compressor exit and burner inlet.

A design goal for the main burner diffuser is to reduce the velocity of the air exiting the compressor as much as necessary to enable optimal performance of the combustor, with the least loss of total pressure consistent with that goal. Unfortunately, an annular flat-wall diffuser has an extremely limited range of design and performance parameters. The best possible flat-wall diffuser has an included angle 2θ = 9 deg [12].

According to Ref [12], whenever the required diffuser area ratio AR is less than four, the excessive length of the diffuser can be reduced by subdividing the flow into adjacent streams, each having an included angle 2θ = 9 deg, as illustrated in Fig 7.1. By the introduction of equally spaced splitter plates, the required length for any AR < 4 is reduced by a dividing factor equal to the number of parallel streams, for example three for the case of two splitter plates as illustrated in Fig 7.1. In principle, the number of splitter plates could be increased to three, four, five, or more, and a correspondingly shorter diffuser would result. However, geometric complexity and difficulty

of manufacturing puts a practical limit on this approach, so that two splitter vanes seem to be optimal [12]. A dump diffuser is required to further increase pressure and complete the transition to the main combustor dome.
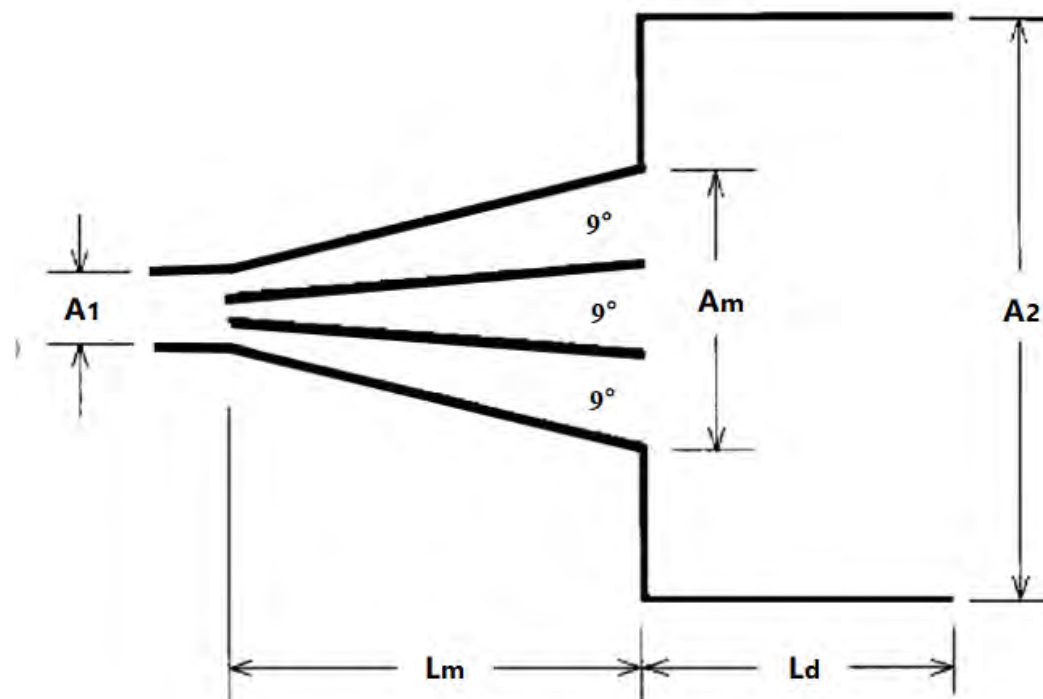
Figure 7.1 Combined Diffuser

The total pressure loss of the annular flat-wall diffuser with two splitters plates is obtained by Eq. (7.1) with the assumption of uniform, steady, incompressible flow with negligible fraction. [12]

$$\Delta P_t = q_1 \left(1 - \frac{1}{AR^2}\right)(1 - \eta_D) \tag{7.1}$$

where q_1 is the inlet dynamic pressure of combustor, AR is the area ratio which equals A_2/A_1 and η_D is the best efficiency of the whole diffuser combined by the flat-wall diffuser and dump diffuser. η_D can be calculated as follows:

$$\eta_D = \frac{\eta_{D9°}AR^2(1 - [A_1/A_m]^2) + 2(AR[A_1/A_m] - 1)}{AR^2 - 1} \tag{7.2}$$

where $\eta_{D9°}$ is the best efficiency of the flat-wall diffuser with expansion angle $2\theta = 9$ deg. $\eta_{D9°}$ is chosen as 0.9378 by Eq. (9.68) of Ref. 12.

Geometry parameters and calculated results are listed in Table 7.2 as follows:

Table 7.2 Pre-Diffuser Calculation

Parameter	Symbols	Value	Unit	Source
Inlet Area of Diffuser Region	A_3	105.033	in^2	Compressor Design
Outlet Area of Flat-Wall Region	A_{31}	300.096	in^2	Combustor Design
Outlet Area of Dump Region	A_{32}	320	in^2	Combustor Design
Total Pressure at Diffuser Region Inlet	$P_{t,3}$	273.535	psia	Cycle Design
Pressure Loss in the Diffuser	dP	0.938	psia	Calculated
		0.343%	%	Calculated
Total Pressure at Diffuser Region Exit	$P_{t,32}$	272.602	psia	Calculated
Static Pressure at Diffuser Region Exit	$P_{s,32}$	270.767	psia	Calculated
Mach Number at Diffuser Outlet	Ma_{32}	0.0975	/	Calculated
Diffuser Length	L_d	4.02	in	Calculated

7.3 LDI Combustor Configuration

Under the pressure of globe warming and climate change, extensive efforts are underway to develop combustors with lower nitrogen oxides (NOx) emissions for use in both subsonic and supersonic civil aircraft engines. In general, the inlet temperature and pressure are constantly increasing in order to improve the performance of the combustion chamber. However, the trend of pressure and temperature increase contradicts the goal of reducing NOx emissions. In order for the combustion chamber to achieve low NOx emissions, it is necessary to consider other influencing factors. The main feasible approaches are as follows:

(1) Reduce the equivalence ratio of the primary combustion zone to achieve lean-burn combustion.

(2) Improve injector structure to improve fuel atomization quality.

(3) Optimize the structure of the combustors to reduce the high-temperature gas residence time and improve the fuel air mixing uniformity.

Three of the currently major low-emission combustion chambers used in aero engines, namely RQL (Rich Burn, Quick Mix, Lean Burn), LPP (Lean, Pre-mixed, Pre-vaporized) and LDI (Lean Direct Injection), and the technical comparison of these combustion chambers are listed in Table 7.3.

Table 7.3 Technical Comparison of Low Emission Combustors [18]

Type of Combustor	NOx Emission Level	Combustion Efficiency	Combustion Stability	Smoke Level	Structure Condition
RQL	Very low	High	Tempering, spontaneous combustion or combustion instability will not occur	High	Long axial length
LPP	Extremely low	Extremely high, but slightly lower at low operating conditions	Tempering, spontaneous combustion and combustion instability will occur especially with high OPR	Extremely low	Short axial length with complex dome structure
LDI	Very low	High, but slightly lower at low operating conditions	No tempering or spontaneous combustion, but combustion instability may occur	Low	Short axial length with complex dome structure and multi-jet injector

According to Table 7.3, RQL could not be chosen as the combustor of CJ 3000 for its long axial length and high smoke level would not suit the demand of passenger aircrafts. LPP is also eliminated because of its tempering, spontaneous combustion and combustion instability in high OPR conditions while CJ 3000 is an aircraft engine with high OPR. Hence, LDI is chosen as the combustor of CJ 3000.

At present, a great deal of research has been conducted on LDI combustors. The NASA Glenn Research Center has developed several LDI concepts for aviation gas turbine combustors. Rolls-Royce also developed a single-loop LDI concept in the ANTLE program (advanced near-term low-emissions program). A typical architecture of LDI combustor is showed in Figure 7.2.
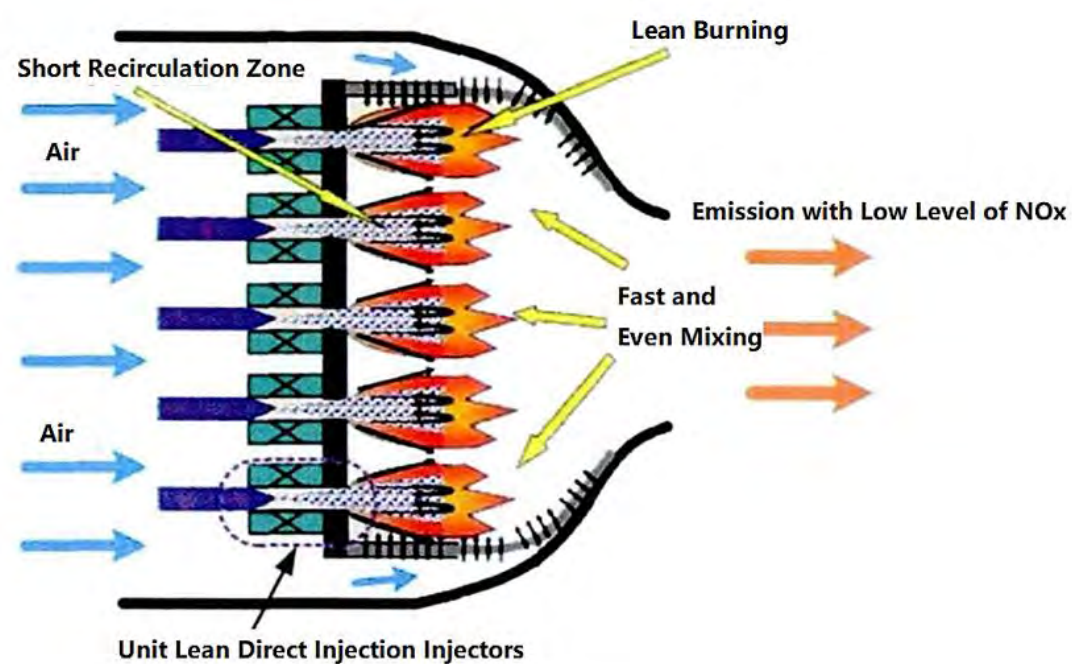
Figure 7.2 LDI Combustor [19]

In the multi-jet lean direct injection combustion chamber structure, the secondary air is reduced or eliminated, and most of the combustion air is introduced into the dome, thereby reducing the equivalence ratio and the flame temperature of the primary zone. Simultaneously, the multi-point injection performed by the dome of the combustor, the micro-mixed lean combustion performed by the unit injectors, and the strong interactions between the adjacent unit injectors make the fuel distribution more uniform, and enhance the effects of evaporation and mixing, resulting in the eliminating of hot spots in the primary zone and the avoiding of local high temperature zone to a greater extent. In addition, the small recirculation zone created by the unit injectors results in a shorter flame length, which reduces the residence time of the combustion. In view of the feasible approach to reducing the NOx emission in the combustors mentioned above, the above structural features of the multi-jet LDI combustors can effectively reduce NOx generation [20].

In addition to significantly reducing NOx emissions, the structural features of the multi-jet LDI combustor also have the following characteristics:

(1) High combustion stability. Since the unit injectors, such as the venturi mixing section of the unit injectors (Fig 7.3 [17]) could have the fuel and air micro-mixed well, no separate premixed section or a short scaled premixed section is needed. Also, the structure of venturi mixing section has a high air velocity at the throat. Therefore, it is possible to avoid the dangers that lean premixed combustion is often difficult to overcome - tempering and spontaneous combustion [20].

(2) Compact and lightweight. The multi-jet LDI combustor is more compact, lighter in weight, shorter in length, and more flexible in arrangement for it does not have a complex premixed system. Hence, the LDI combustors makes full use of the combustion space. In addition, the miniaturized injectors shorten the length of the flame. Therefore, the length of the combustors can be designed to be shorter for the complete layout of the gas turbine [20].
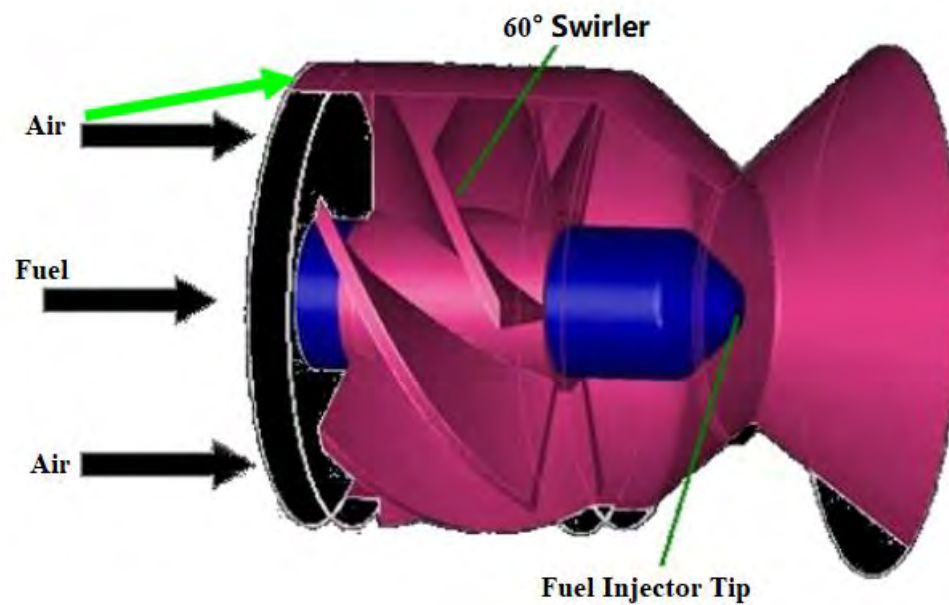
Figure 7.3 NASA LDI Unit Injector [17]

7.4 Air Flow Distribution

Airflow in the burner is distributed to different combustion zones to permit the desired fuel-to-air ratio and satisfy cooling demands. The airflow distribution normally does not vary significantly with combustor operating conditions [21]. Exact nomenclature for different airflows discussed in this design process are listed below:

W_c – Combustor inlet flow.

W_f – Fuel flow into the combustor.

W_{am} – Fuel atomizing airflow admitted through the fuel injector to brake the fuel into small drops.

W_{pz} – Airflow introduced into the dome.

W_{dc} – Cooling air to cool the dome.

W_{sw} – Swirler airflow admitted through a swirler around the atomizer to provide a strong, well-mixed recirculation zone within the primary zone.

W_{pa} – Airflow through the passage.

W_c – Cooling air to cool the liner.

W_{di} – Airflow introduced into dilution holes.

Note that data without source are considered to be calculated according to Ref 12.

7.4.1 Fuel Atomizing Flow

An air-blast atomizer typically requires about 3 lbm of primary air per lbm of fuel [12]. Fuel atomizing flow and other related parameters are listed in Table 7.4.

Table 3 Fuel Atomizing Flow Calculation

Parameter	Symbols	Value	Unit	Source
Combustor Flow	W_c	169.263	lb/s	Cycle Design
Fuel Flow	W_f	4.178	lb/s	Cycle Design
Atomize Air to Fuel Ratio	AFR	3	/	Ref 12, Page 379
Fuel Atomizing Flow Calculation	W_{am}	12.535	lb/s	Combustor Design
		7.41%	%	Combustor Design

7.4.2 Swirler Flow and Dome Cooling Flow

The equivalence ratio of the LDI combustor primary one is generally 0.6 to 0.8, which is taken as 0.6 here [20]. The dome air flow can be determined from the equivalence ratio of the primary and the fuel flow. The dome cooling air flow is generally 40% of the dome air flow [22]. Swirler flow, dome cooling flow and other related parameters are listed in Table 7.5.

Table 7.5 Swirler Flow and Dome Cooling Flow Calculation

Parameter	Symbols	Value	Unit
Equivalence at Primary Zone	FAR_{pz}	0.6	/
Dome Air Flow	W_{pz}	101.66	lb/s
		60.06%	%
Dome Cooling Flow Assumed	W_{dc}	40.66	lb/s
		24.02%	%
Swirler Flow	W_{sw}	48.46	lb/s
		28.63%	%

7.4.3 Liner Cooling Flow and Dilution Flow

After the primary zone the next priority of air partitioning must be liner cooling, as sufficient cooling air must be allocated to protect the burner liner and dome from the high radiative and convective heat loads produced within the burner. The coolant air is normally introduced through the liner in such a way that a protective blanket or film of air is formed between the combustion gases and the liner hardware [12]. Transpiration cooling and film cooling could be chosen as cooling methods used in combustors. While the transpiration

cooling has problem of pore clogging [23], film cooling is selected to cool the CJ 3000 combustor liner (Fig 7.4).
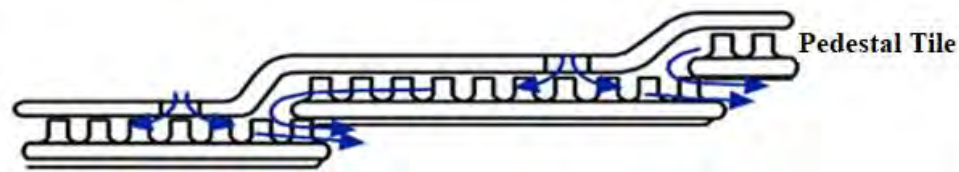
Figure 7.4 Film Cooling Method [24]

The effectiveness of whatever cooling technique may be employed is quantified by the cooling effectiveness, defined by Eq. (7.3) [12].

$$\emptyset = \frac{T_g - T_m}{T_g - T_c} \tag{7.3}$$

where T_g, T_m, and T_c are the static temperatures of the mainstream gas, average wall material limit, and cooling air, respectively. Note that $T_c = T_{t,32}$, the total temperature at the outlet of diffuser. While the wall material was chosen as SiC/CMC with TBCs mentioned above, T_m equals 2700 ºF [8].

Cooling air mass flow rates for varying values of cooling effectiveness are presented in Fig 7.5 [25].
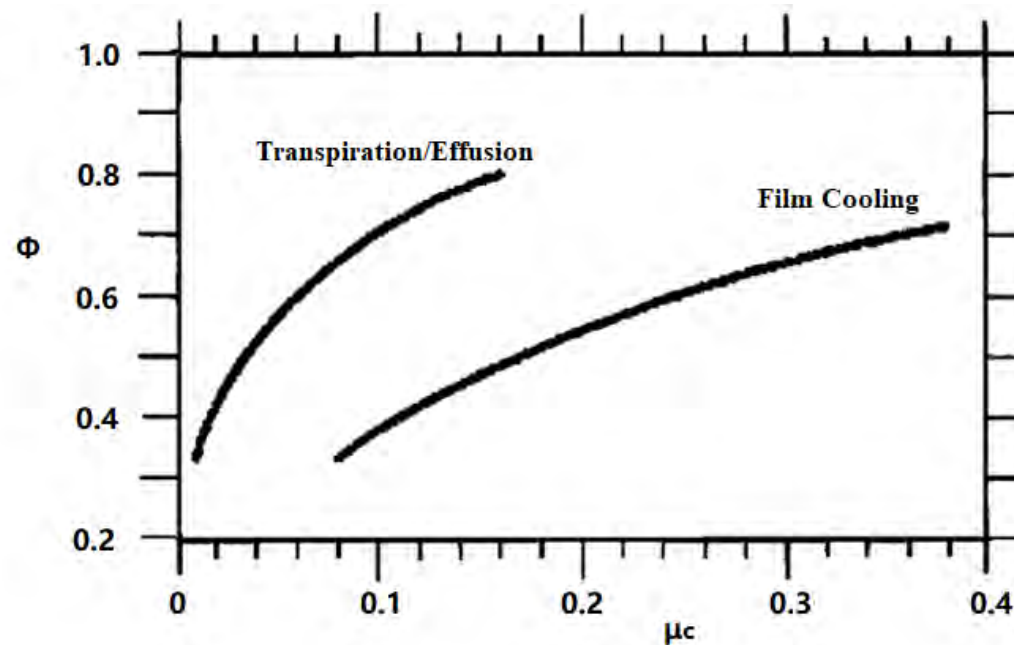
Figure 7.5 Air Flow μ_c Fraction Required for Given Cooling Effectiveness ϕ [25]

Equation (7.4) is approximate curve fits to Fig 18 and provide approximate design data for the fraction of main burner airflow required to achieve any desired cooling effectiveness, as illustrated in Fig 7.5 [12].

$$\mu_c = \frac{m_c}{m_3} \cong \frac{\varphi}{6(1-\varphi)} = \frac{1}{6}\left(\frac{T_g - T_m}{T_g - T_c}\right) \tag{7.4}$$

Hence, liner cooling flow, dilution flow and other related parameters are listed in Table 7.6.

Table 7.6 Liner Cooling Flow and Dilution Flow Calculation

Parameter	Symbols	Value	Unit
Passage Air Flow	W_{pa}	67.60	lb/s
		39.94%	%
Liner Cooling Flow	W_c	23.22	lb/s
		13.72%	%
Dilution Flow	W_{di}	44.38	lb/s
		26.22%	%

.

7.4.4 Summary of Air Distribution

Unlike other combustors, LDI combustor introduces a large amount of air into the dome to ensure a low equivalence ratio in the primary zone for stable lean combustion. Dome flow and passage air flow are listed in Table 7.7.

Table 7.7 Summary of Air Distribution

Parameter	Symbols	Value	Unit
Dome Flow	W_{pz}	101.66	lb/s
		60.06%	%
Passage Air Flow	W_{pa}	67.60	lb/s
		39.94%	%

7.5 Combustor Sizing

7.5.1 Dome and Passage Height

According to Ref 12, the best value of dome height to combustor height ratio, namely α could be calculated by Eq. (7.5).

$$\alpha_{opt} = 1 - \left(\frac{m_A}{m_c}\right)^{\frac{2}{3}} \left(\frac{\Delta P_t}{q_r}\right)_{MB}^{-\frac{1}{3}} \tag{7.5}$$

where m_A is the sum of airflow into secondary hole and dilution hole, m_c is the combustor inlet flow and $\frac{\Delta P_t}{q_r}$ is another form of total pressure loss coefficient defined by total pressure loss to pressure loss coefficient, which could be found in cycle analysis. For LDI combustor does not have secondary holes, Eq. (7.5) could be rewritten as Eq. (7.6).

$$\alpha_{opt} = 1 - \left(\frac{w_{di}}{W_c}\right)^{\frac{2}{3}} \left(\frac{\Delta P_t}{q_r}\right)_{MB}^{-\frac{1}{3}} \tag{7.6}$$

The combustor height ratio could be calculated by using parameters from the diffuser, while the mean diameter could be found in turbine design. Dome height, passage height and other related parameters are listed in Table 7.8.

Table 7.8 Dome and Passage Height

Parameter	Symbols	Value	Unit
Pressure Loss in the Combustor	dP	10.503	psia
		3.840%	%
Pressure Loss Coefficient of Dynamic Pressure	$\left(\frac{\Delta P_t}{q_r}\right)_{MB}$	5.77	/
Best Value of Height Ratio	α_{opt}	0.77	/
Combustor Height Calculated	H_r	2.76	in
Dome Height Calculated	H_L	2.13	in
Half Passage Height	H_p	0.31	in
Combustor Tip Diameter	D_{ct}	36.24	in
Combustor Hub Diameter	D_{ch}	30.10	in
Combustor Mean Diameter	D_{cm}	33.17	in

7.5.2 Number of Fuel Injectors and Combustor Length

According to Ref 17, 20 and 26, the inner and outer diameters of the swirler blades widely used in LDI were 0.708 in and 1.732 in, small values to reduce unit injector area to arrange multi-point injection, which was also selected in CJ 3000. The length of the combustor could be estimated using method in Ref 12. Number of fuel injectors, length of the combustor and other related parameters are listed in Table 7.9.

Table 7.9 Number of Fuel Injectors, Length of the Combustor

Parameter	Symbols	Value	Unit
Inner Diameter of swirler blades	D_{sin}	0.708	in
Outer Diameter of swirler blades	D_{sout}	1.732	in
Number of Fuel Injectors Calculated	$N_{fi,c}$	111.73	/
Number of Fuel Injectors Selected	N_{fi}	112	/
Combustor Length	L_c	4.57	in
Combustor Length to Height Ratio	L_c/H_L	2.15	/
Total Combustor Length	L_t	8.59	in

7.6 Performance Check

7.6.1 Total Pressure Loss

The total pressure loss in the combustion chamber should be greater than the total pressure loss due to the increase in total temperature, while the total pressure loss mentioned above is found in cycle design. Hence the total pressure loss must be checked to make sure that the total pressure loss caused by temperature increasing could be tolerated. The total pressure loss caused by total temperature increasing could be calculated by Eq. (7.7) [12] as follows.

$$\left(\frac{\Delta P_t}{q_r}\right)_{MB} > \left(\frac{\Delta P_t}{q_r}\right)_{MBmin} = \left(\frac{W_{pz}}{W_c}\right)^2 \left(\frac{A_r}{A_L}\right)^2 \tau_{pz}(2\tau_{pz} - 1) = \left(\frac{W_{pz}}{W_c}\right)^2 (\alpha_{opt})^2 \tau_{pz}(2\tau_{pz} - 1) \tag{7.7}$$

The check of total pressure loss is listed in Table 7.10.

Table 7.10 The Check of Total Pressure Loss

Parameter	Symbols	Value
Design Pressure Loss Coefficient	$\left(\frac{\Delta P_t}{q_r}\right)_{MB}$	5.77
Minimum Pressure Loss Coefficient	$\left(\frac{\Delta P_t}{q_r}\right)_{MBmin}$	4.83
Margin of Pressure Loss	M	16.12

The design pressure loss coefficient is higher than the lower limit and have a margin over 16%. Hence, the setting of total pressure loss is reasonable. Besides, according to Table 7.2 and 7.8, the combustor satisfies the design requirement of total pressure recovery coefficient equal to 0.9579.

7.6.2 Combustor Efficiency

The combustor efficiency would be checked by a combustor loading parameter (CLP) and Fig 7.6 which correlates well with combustor efficiency and is calculated by Eq. (7.8) [27].

$$CLP = \theta = \frac{P_{t,32}^{0.75} \cdot A_{ref} \cdot H \cdot e^{\frac{T_{t,3}}{b}}}{m_c} \qquad (7.8)$$
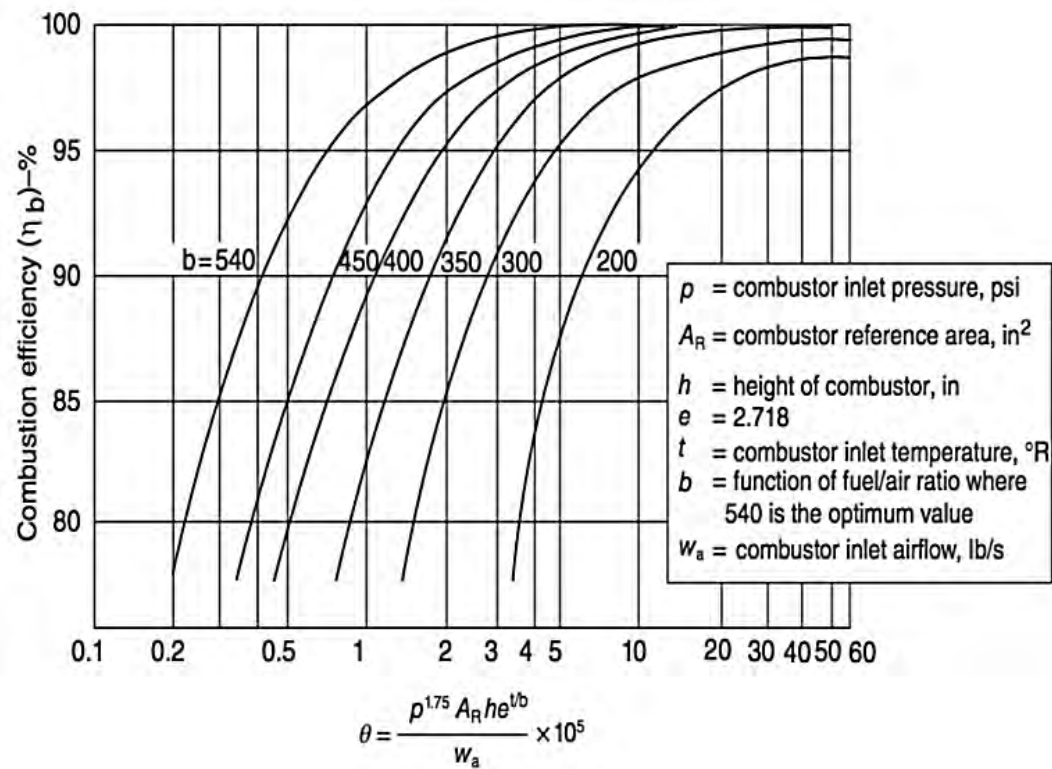
Figure 7.6 Combustor Efficiency

The reaction rate parameter, b, depends on the primary zone equivalence ratio, FAR_{pz}, and is calculated by the Eq. (7.9) [27].

$$b = 382\left(\sqrt{2} \pm \ln\frac{FAR_{pz}}{1.03}\right) \qquad (7.9)$$

where (+) for $FAR_{pz} < 1.03$ and (-) for $FAR_{pz} > 1.03$.

The check of combustor efficiency is listed in Table 7.11.

Table 7.11 Combustor Efficiency

Parameters	Value
FAR_{pz}	0.6
b	334
CLP	152×10^5
Estimated Combustor Efficiency	Tends to 100%
Design Combustor Efficiency	99.70%

Hence, the design of combustor efficiency, 99.70%, is satisfied.

7.7 3D Geometry of Combustor

After all the above-mentioned calculations, the three-dimensional sketch of the combustor can be drawn as follows:
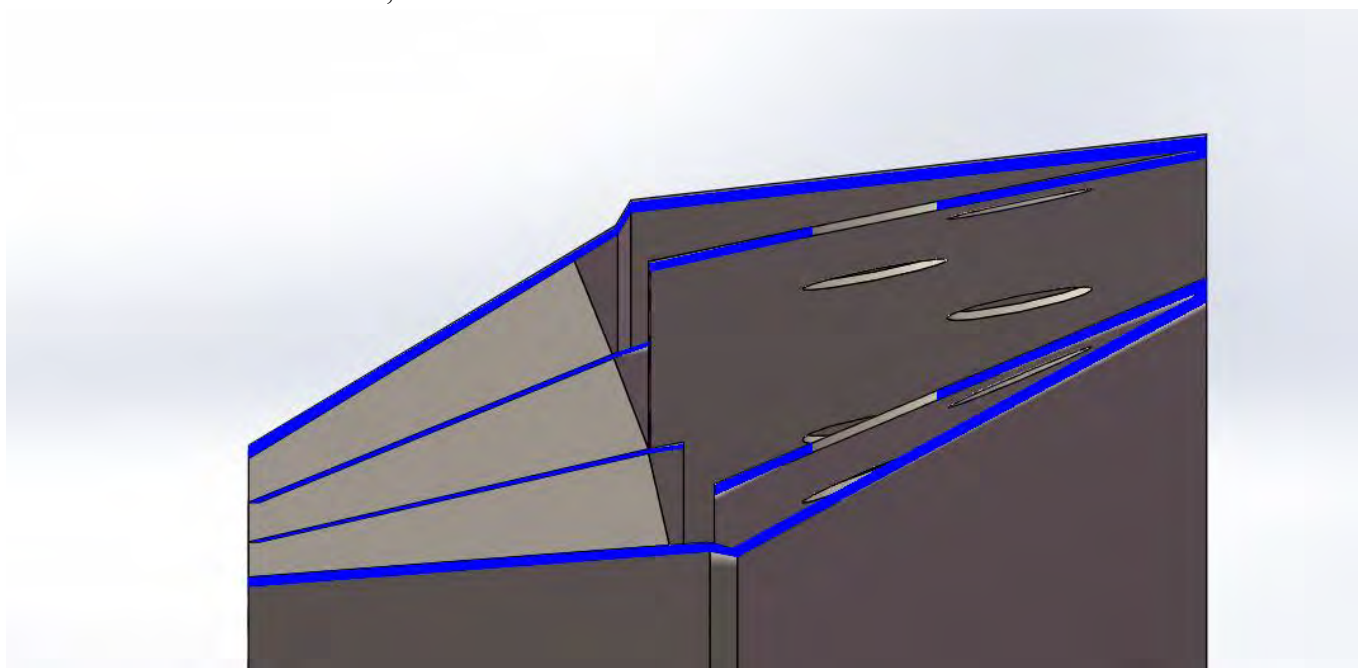
Figure 7.7 3D Sketch of the Combustor

8 Mixer Design

The CJ 3000 utilizes a forced flow lobed mixer to mix the core flow with the bypass flow, which is helpful to obtain thrust gain and

reduce that maximum outlet jet velocity of the nozzle. The flow through the mixer is demonstrated in Figure 8.1.
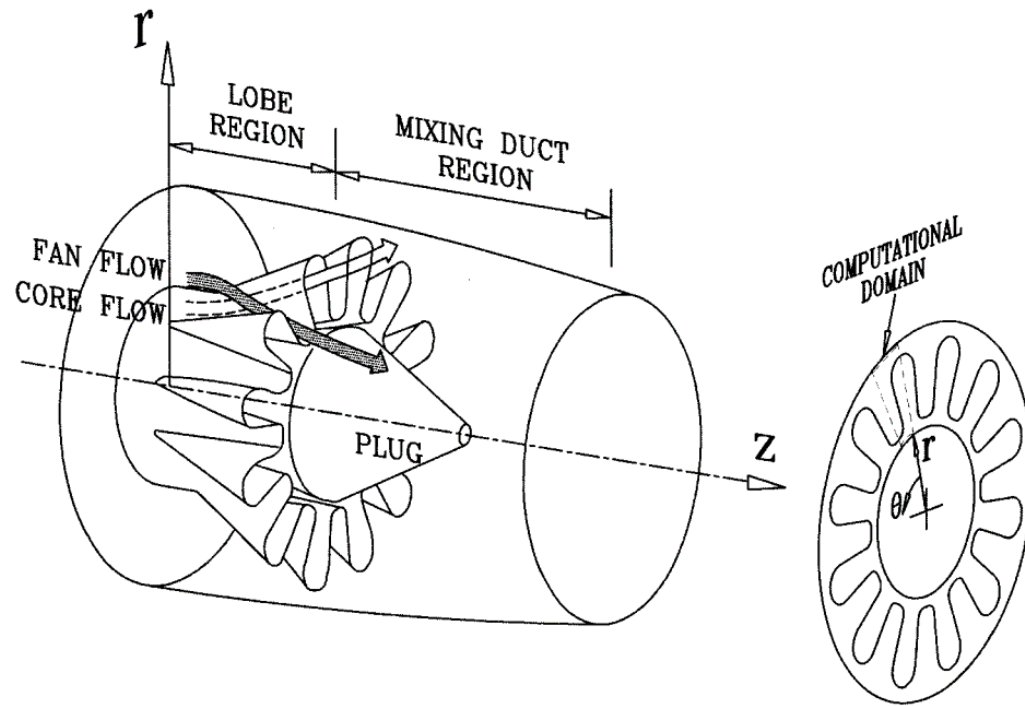
Figure 8.1 The Flow through Mixer [28]

8.1 Design Point Selection

The design point of cycle analysis (supersonic cruise) is chosen as the design point of mixer as well for the cruise is the main mission of all the missions. Mixer inlet condition of the design point is quoted from the cycle design and turbine design and listed in Table 8.1.

Table 8.1 Mixer Inlet Condition

Parameter	Symbol	Value	Unit
Bypass Exit Total Temperature	$T_{t,16}$	782.8	$°R$
Bypass Exit Static Temperature	$T_{s,16}$	754.8	$°R$
Bypass Exit Velocity	V_{16}	584.51	ft/s
Bypass Exit Mach Number	Ma_{16}	0.434	/
LPT Exit Total Temperature	$T_{t,6}$	1744.80	$°R$
LPT Exit Static Temperature	$T_{s,6}$	1672.33	$°R$
LPT Exit Velocity	V_6	884.81	ft/s
LPT Exit Mach Number	Ma_6	0.441	/
Mixer Exit Mach Number	Ma_{64}	0.28	/
Bypass to LPT Pressure Ratio	$P_{t,16}/P_{t,6}$	1.07	/
Bypass Exit Inside Radius	R_{16in}	30.91	in
Bypass Exit Outside Radius	R_{16out}	42.44	in
Bypass Exit Area	A_{16}	2656.70	in^2
LPT Exit Inside Radius	R_{6in}	21.02	in
LPT Exit Outside Radius	R_{6out}	30.83	in
LPT Exit Area	A_6	1599.60	in^2

8.2 Mixer Configuration

In order to decide whether to use a lobed mixer or an annular mixer, five selection principles have been proposed as follows [29]:

(1) When the Mach number of the outlet section of the mixer is greater than or equal to 0.2, select the lobed mixer.

(2) When the core inlet section twist angle of the mixing section is greater than or equal to 7° and bypass inlet section twist angle of the mixing section is greater than or equal to 3°, the lobed mixer is usually selected.

(3) When the bypass ratio is greater than or equal to 0.4, the lobed mixer should be selected.

(4) When the bypass ratio changes significantly during the whole mission, the lobed mixer should be selected.

(5) When the Mach number of the turbine outlet is less than or equal to 0.5, the annular mixer could be chosen.

Considering the above principles and the data of the cycle analysis and mixer inlet, the lobed mixer is chosen as the mixer of the CJ 3000.

8.3 Lobes Design

The lobed mixer induces a series of axial vortices through the shear layer at the cold and hot boundary layers of the lobe trailing edge as Fig 8.2, which improves the ability to mix the two streams.
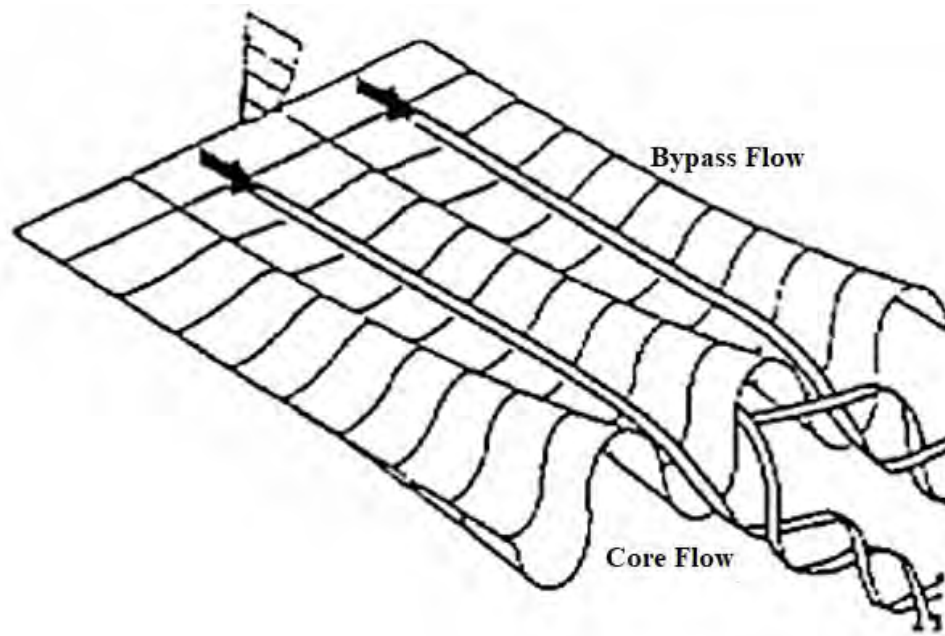
Figure 8.2 Lobe Mixing Mechanism [29]

According to Ref [30], when the lobe cycle length is equal to the lobe height, the mixing efficiency is maximized. At the meanwhile, the number of lobes should be between 12 and 20, and the height of the lobes and the height of the diverter ring passage should be between 0.55 and 0.85 [31]. Hence, the calculation of mixer lobe is shown in Table 8.2.

Table 8.2 Lobes Design

Parameter	Value	Unit
Diverting Ring Diameter	61.81	*in*
Diverting Ring Perimeter	194.09	*in*
Lobe Height	12.13	*in*
Lobe Period Length	12.13	*in*
Lobe Number	16	/
Lobe-Diverting Ring Height Ratio	0.8311	/
Extended Half Angle	25	*rad*
Minimum Lobe Length	12.99	*in*

6.4 Mixing Duct Design

After being mixed by lobes, the flow passes through the mixing duct to increase the mixing efficiency and static pressure properly. The length-to-diameter ratio (L/D) of the mixing duct could be estimated by the mixer type and mixing efficiency [29]. The total pressure recovery coefficient could be calculated by Eq. (8.1) [29]:

$$\sigma_{mix} = \frac{1}{\bar{A}_{mix}} \frac{\sqrt{(1+B)(1+B\theta)}}{1+B\theta} \frac{q(\lambda_{cp})}{q(\lambda_{mix})} \tag{8.1}$$

where $\bar{A}_{mix}$ is the outlet-to-inlet area ratio, B is the bypass ratio, θ is the bypass-to-core flow temperature ratio, $q(\lambda_{cp})$ is the flow function of core flow and $q(\lambda_{mix})$ is the flow function of mixer outlet flow.

The ideal thrust gain ratio could be calculated by Eq. (8.2) [29]:

$$\bar{F} = \frac{\sqrt{(1+B)\left(1+BC_p\theta\right)}}{1+B\sqrt{\theta}} \tag{8.2}$$

where C_p is the constant pressure specific heat capacity of the flow here. And if the mixing efficiency is less than 1, the actual thrust gain ratio should be estimated as follows [29]:

$$\bar{F}_t = 1 + K(\bar{F} - 1) \tag{8.3}$$

where K is the mixer efficiency.

The design of the mixing duct is listed in Table 8.3.

Table 8.3 Mixer Design

Parameter	Value	Unit
Mixer Exit Area	6494.51	in^2
Mixer Exit Radius	45.28	*in*
Mixer Area Ratio	1.526	/
Mixer efficiency	0.6	/
Length-Diameter Ratio	0.5	/
Mixing Duct Length	45.28	*in*
Mixer Total Pressure Recovery Coefficient	0.9951	/
Mixer Ideal Thrust Gain Ratio	1.0209	/
Mixer Actual Thrust Gain Ratio	1.0126	/

It could be seen that the total pressure recovery coefficient (0.995) satisfy the design request value (0.99), and the design mixer efficiency (0.6) could be achieved by L/D being equal to 0.5.

After all the above-mentioned calculations, the three-dimensional sketch of the mixer can be drawn as follows:
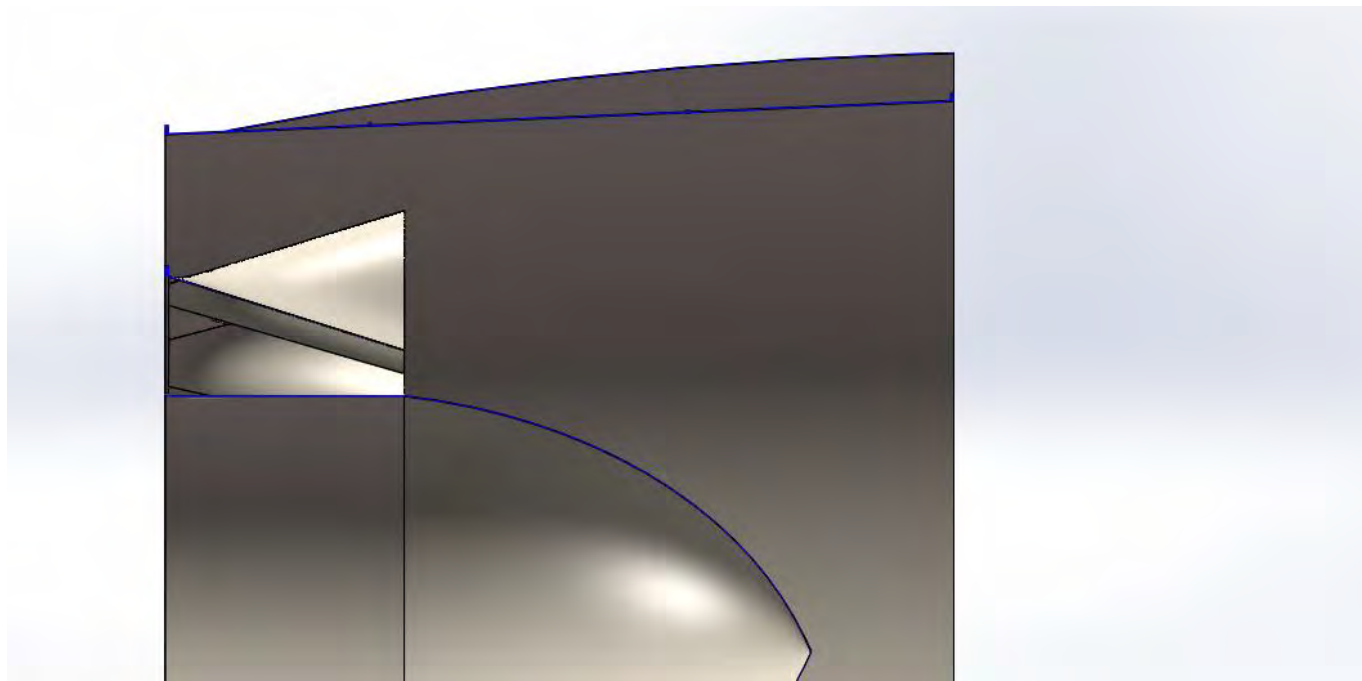
Figure 8.3 3D Sketch of the Mixer

9 Nozzle Design

To enable efficient supersonic cruise, and to meet current noise restrictions at take-off, an appropriate convergent-divergent noise-attenuating nozzle must also be designed. The nozzle should be designed to optimize internal performance (e.g. gross thrust coefficient) with proper nozzle propulsion system drags [1].

9.1 Inlet Conditions

The adjustable convergent-divergent nozzle should meet the requirement of all four work points, the inlet conditions of nozzle at four points are listed in Table 9.1.

Table 9.1 Inlet Conditions of Nozzle

Parameter	SLS Takeoff	Hot Day Takeoff	Transonic Point	Supersonic Cruise
Flow of Nozzle (lb/s)	1633.251	1653.863	677.713	668.826
Total Temperature of Nozzle ($°R$)	898.70	960.83	867.40	1055.37
Total Pressure of Nozzle (psia)	32.947	34.522	13.431	13.742
Atmospheric Pressure (psia)	14.697	14.697	2.677	1.502
Nozzle Inlet Area (square in)		6494.51		
Nozzle Inlet Radius (in)		45.28		

9.2 Nozzle Sizing and Performance

The design of the nozzle should meet two requirements. The one is that the takeoff jet velocity is less than 1375ft/s at takeoff and another one is that the thrust coefficients of each condition should be greater than or equal to the design value. The thrust coefficient could be calculated by Eq. (9.1) [31]:

$$C_F = \frac{C_V C_A \varphi_{NZ} \frac{\bar{m}_8}{\sqrt{T_{t8}}} V_9 + \left(\frac{P_9}{P_{t8}} - \frac{P_a}{P_{t8}}\right)\frac{A_9}{A_8}}{\varphi_{NZ} \frac{\bar{m}_8}{\sqrt{T_{t8}}} V_{9,id}} \tag{9.1}$$

where C_V is the speed correction factor, C_A is the angle correction factor, $\bar{m}_8$ is the flow factor of nozzle throat, V_9 is the actual velocity of nozzle exit and $V_{9,id}$ is the ideal velocity of nozzle exit after isentropic full expansion. The parameter could be calculated or estimated by Ref [31] and other parameters could be found in cycle design.

According to Ref [31], the convergence half angle should be between 5° and 45°, and the extended half angle should be less than 16°, which would be a limit in the sizing of nozzle.

The nozzle sizing and performance are listed in Table 9.2.

Table 9.2 The Nozzle Sizing and Performance

Parameter	SLS Takeoff	Hot Day Takeoff	Transonic Point	Supersonic Cruise
Nozzle Throat Area (square in)	2867.51	2867.51	2866.89	2988.87
Nozzle Exit Area (square in)	2867.51	2867.51	3870.30	5379.97
Exit to Throat Area Ratio	1	1	1.35	1.8
Nozzle Throat Radius (in)	30.21	30.21	30.21	30.84
Nozzle Exit Radius (in)	30.21	30.21	35.24	41.38
Velocity of Exit (lb/s)	1327.92	1373.13	1963.72	2430.42
Static Pressure of Exit (psia)	18.175	19.843	2.704	1.572
Convergence Half Angle (°)	31.44	31.44	31.44	30
Extended Half Angle (°)	0	0	5.54	12
Convergence Length (in)	24.96	24.96	24.96	25.33
Extended Length (in)	50.69	50.69	50.45	49.57
Total Length (in)	75.65	75.65	75.41	74.9
Pressure Ratio	2.12	2.35	5.04	9.15
Actual Thrust Coefficient	0.9305	0.9305	0.9795	0.9644
Thrust Coefficient in Cycle Analysis	0.9305	0.9305	0.9740	0.9600

From Table 31, the actual thrust coefficients satisfy the requirement of cycle analysis and the velocities of takeoff are less than 1375 ft/s. It should be noted is that as the area ratio at takeoff equals 1, the convergent-divergent nozzle would be seen as a convergent nozzle at takeoff. Hence, the thrust coefficients of takeoff calculated are 0.9747 and 0.9653, which are higher than general convergent-divergent nozzle (0.9305) by Fig 9.1 [1]. In order to improve the reliability of the nozzle thrust coefficient, the thrust coefficients of takeoff are determined as 0.9305 by Fig 9.2 [1].
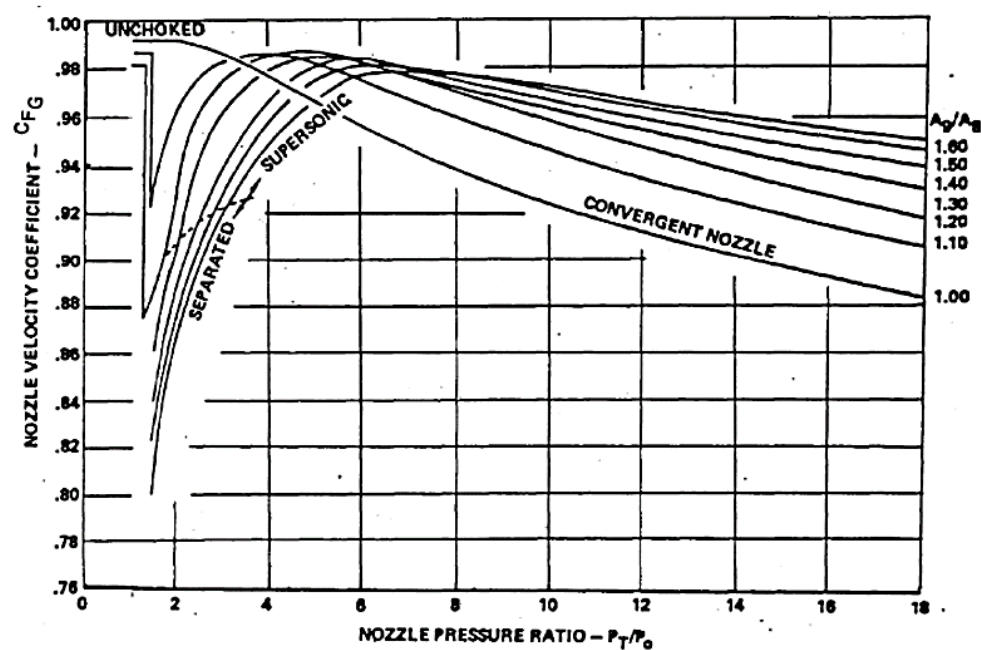
Figure 9.1 Changes of Thrust Coefficient due to Convergent Nozzle [1]
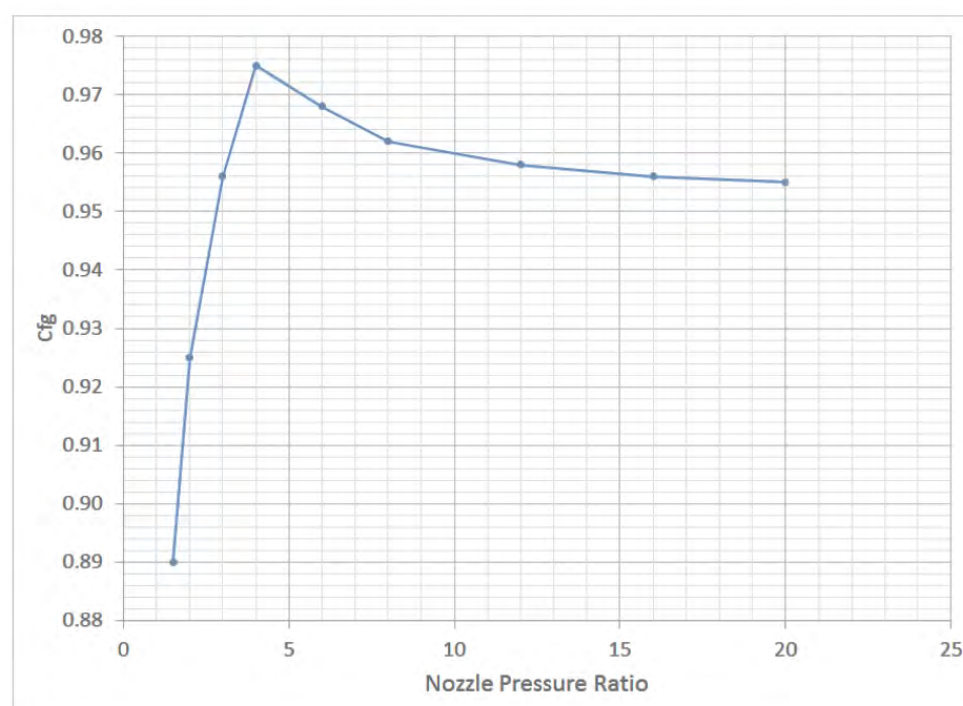
Figure 9.2 General Thrust Coefficient of Convergent-Divergent Nozzle [1]

The three-dimensional sketch of the mixer can be drawn as follows:
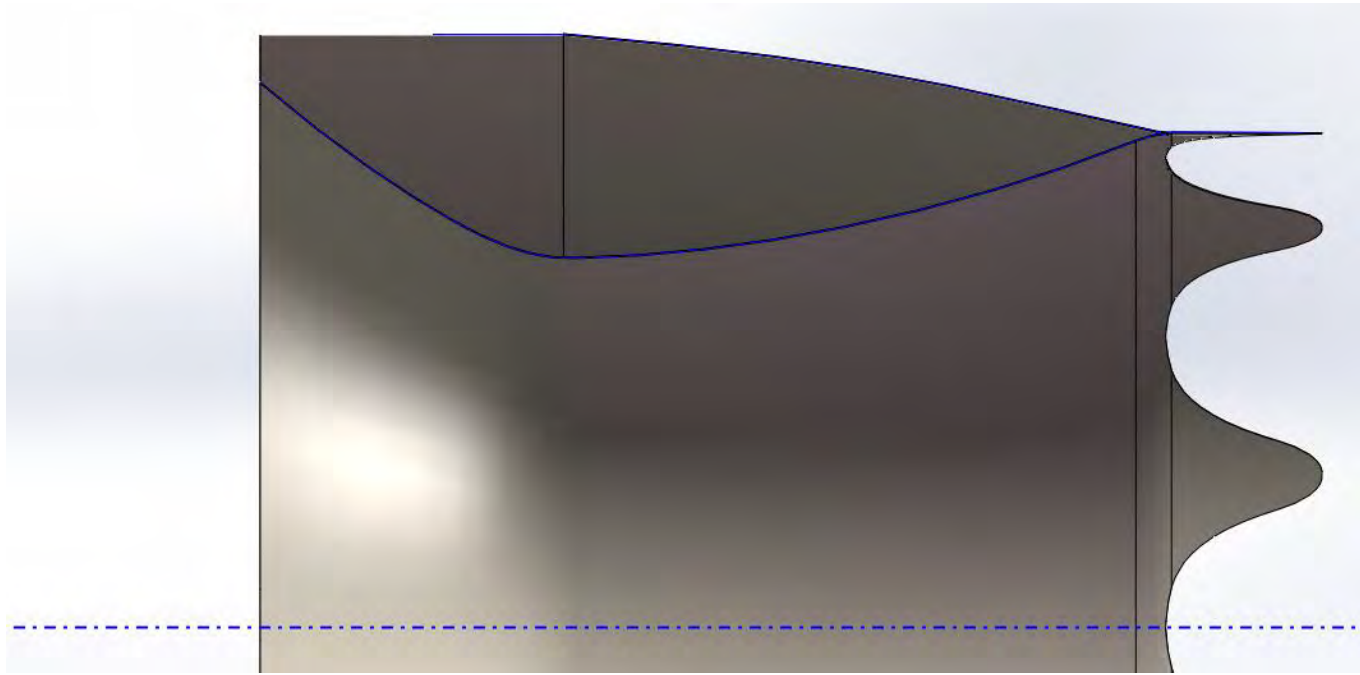
Figure 9.3 3D Sketch of the Nozzle

9.3 Nozzle Afterbody Drag

The nozzle afterbody drag should be estimated to check the installed performance. Nozzle afterbody drag results from shear forces (friction), pressure drag, and shock losses. It is a primarily a function of freestream Mach number and nozzle boat-tail curvature. An example nozzle drag curve is shown in Figure 9.4 [1].
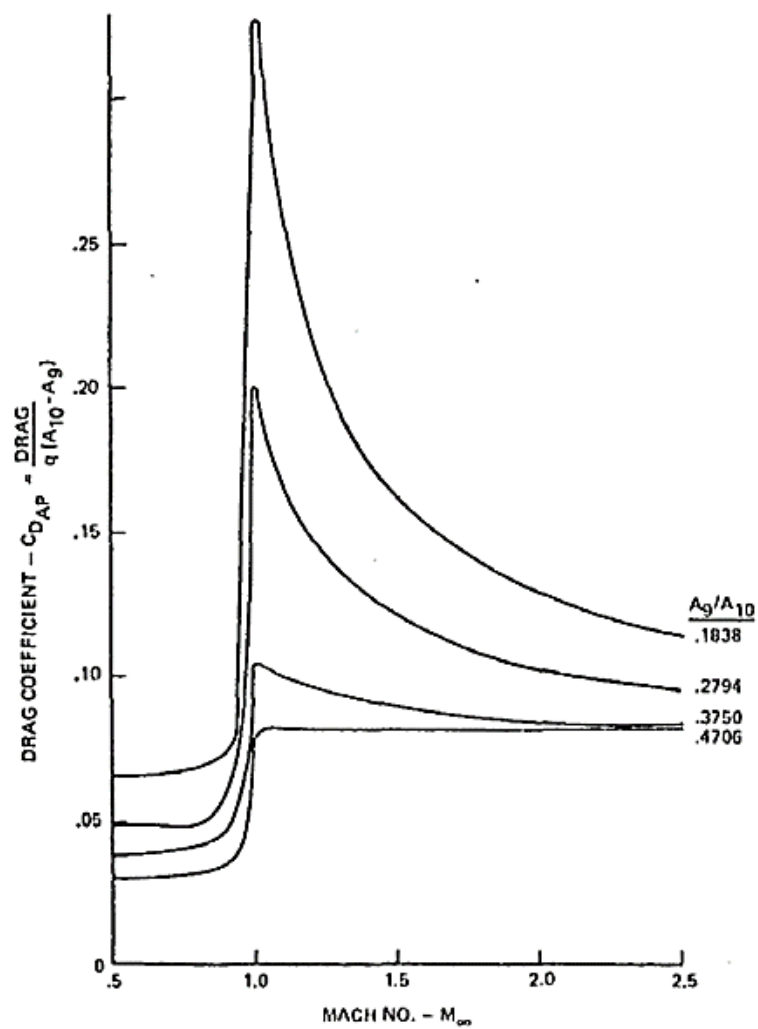
Figure 9.4 The Nozzle Drag Coefficient Curve [1]

In this example, the drag coefficient is presented as a function of nozzle exit area A_9 and the upstream maximum cross-sectional area A_{10}, and q is the dynamic pressure of the freestream outside the engine. From the drag coefficient curve above, the nozzle afterbody drag could be estimated as follows:

Table 9.3 The Nozzle Afterbody Drag

Parameter	SLS Takeoff	Hot Day Takeoff	Transonic Point	Supersonic Cruise
Nozzle Afterbody Drag (*lbf*)	0	96.25	718.65	454.60

36

10 Installed Performance Checking

Installed performance considers and includes inlet recovery and inlet drag from the inlet design, nozzle drag provided in section 9.3, 1% HP compressor customer bleed air, and 100 HP customer power extraction from the HP spool [1]. The installed performance would be checked in Table 10.1.

Table 10.1 The Check of Installed Performance

Flight Condition	Cycle Parameter	Requirements	CJ 3000	Margin (%)
SLS Takeoff	Thrust (lbf)	64625	64754.3	0.20
	TSFC (lbm/lbf/h)	0.520	0.4299	17.33
Hot Day Takeoff	Thrust (lbf)	56570	56582.9	0.02
	TSFC (lbm/lbf/h)	0.652	0.5445	16.49
Transonic Pinch Point	Thrust (lbf)	14278	14287.03	0.06
	TSFC (lbm/lbf/h)	0.950	0.8276	12.88
Supersonic Cruise	Thrust (lbf)	14685	15010.70	2.22
	TSFC (lbm/lbf/h)	1.091	0.9874	9.50

From Table 10.1, we note that installed fuel efficiency of the CJ 3000 meets the requirements at every operating point with the margin over 9 % while the thrust level requirement is satisfied. For SLS take-off, the CJ 3000 decreases fuel consumption by over 17% of the requirement. For hot day take-off, the CJ 3000 decreases fuel consumption by over 16% of the requirement. For transonic pinch point, the CJ 3000 decreases fuel consumption by over 12% of the requirement. For supersonic cruise, the CJ 3000 decreases fuel consumption by over 9% of the requirement. It can be seen that the requirements for installation performance have also been achieved with proper thrust levels and high TSFC margins.

11 Engine Noise Suppression

As the CJ 3000 is designed for the supersonic transport, the engine noise must be controlled to avoid the noise damaging airport buildings and surrounding personnel. Engine noise mainly comes from exhaust jet and turbomachines. Hence, different noise reduction measures have been taken for these two parts of the noise.

11.1 Exhaust Jet Noise

Three methods of different aspects have been taken to reduce the exhaust noise as follows.

11.1.1 Exhaust Jet Velocity Reduction

Since the sound power of the exhaust gas is in an eighth power relationship with the exhaust jet gas velocity [33], the most direct method of suppressing noise is to reduce the exhaust gas velocity. We have reduced the exhaust jet velocity to less than 1375 ft/s at takeoff with using mixer and taking a large bypass ratio, which makes the suppression of noise easier [1].

11.1.2 Noise Energy Reduction

The sawtooth trailing edge nozzle, which has been used in Trent 1000 of Boeing 787 to suppress the noise is taken in the CJ 3000 as well. Sawtooth nozzles significantly could change the development of the velocity shear layer and the density of turbulence to reduce the noise. According to a NASA study, the sawtooth nozzle can reduce noise by about 2 dB to 3 dB with very little loss of thrust [32]. An example architecture of sawtooth nozzle is shown in Fig 11.1.
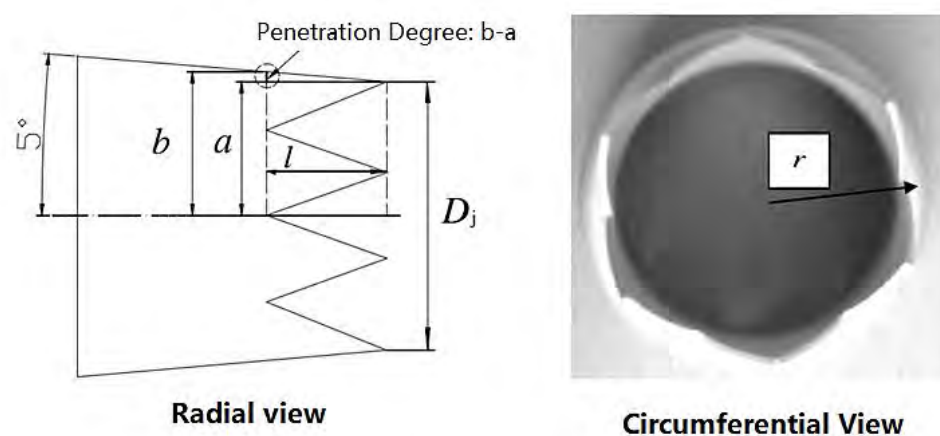
Figure 11.1 Sawtooth Trailing Edge Nozzle [32]

Each triangular protrusion in Fig 11.1 represents a sawtooth trailing edge, and the number of protrusions represents the number of sawtooth. According to Ref [32], as the sawtooth number increases, the ability of the nozzle to reduce noise become stronger. And as the penetration degree increases, the low-frequency noise reduces and the high-frequency noise increases, while the high-frequency noise would be attenuated in the atmosphere easily [33]. Hence, a sawtooth nozzle with large number of sawtooth and high penetration degree would reduce the noise largely. Due to Ref [32], we choose the sawtooth number as 10 with high penetration degree.

11.1.3 Noise Energy absorption

Helmholtz resonators target specific frequencies by using a trapped volume to absorb acoustic energy through harmonic oscillation of a mass slug in the neck [34]. These frequencies of resonators are a function of speed of sound in the fluid medium coupled with the cavity

volume as Fig 11.2 shows:
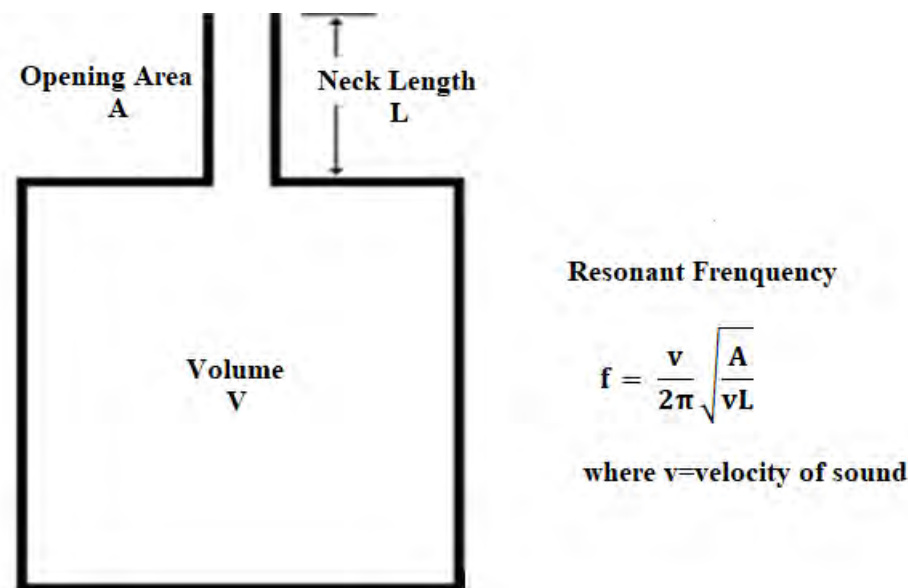
Figure 11.2 Helmholtz resonators [35]

Hence, the liner with Helmholtz resonators could be used in the divergent duct of nozzle as Fig 11.3 to absorb the noise with specific frequencies, especially the specific high frequencies, since the high-frequency noise would be increased by sawtooth nozzle.
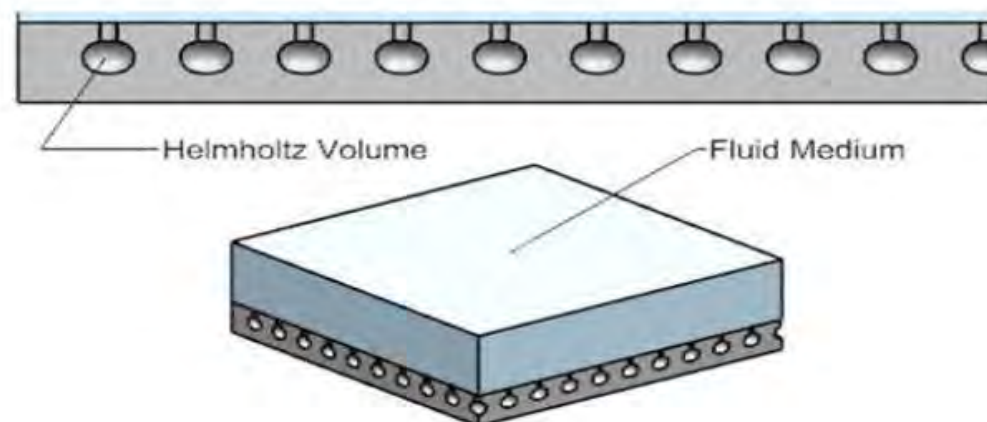
Figure 11.3 The Divergent Duct Liner with Helmholtz Resonator [35]

11.2 Turbomachine Noise

Four measures have been taken to reduce the turbomachine noise as follows:

(1) The cancel of the inlet guide vane of the fan. By canceling the guide vane, the aero-dynamic noise caused by the fan would be greatly reduced by about 10 dB [33].

(2) The Mach number of inlet throat equals 1, which would reduce the noise through the inlet caused the compressors [33].

(3) The ratio of stator blade number to the corresponding number of rotor blades is greater than 2, which would reduce the noise power by acoustic principle. At the meanwhile, expect the first stage of IPC, each blade passage frequency extremely keeps away from 3000Hz, which is the sensitive frequency of human's ears [33].

(4) Liner with Helmholtz resonators would be used at the inlet, the casing of compressors, the inside and outside wall of the bypass duct to reduce specified frequencies noise as mentioned above.

12 Overall Structural Design

Vibration characteristics are important information when the engine is running. This chapter describes the material selection of the CJ3000 aeroengine components, the possibility of implementing the CJ3000 on the structure, and the vibration characteristics of the CJ3000 during operation.

With reference to the classic design of the aero engine structure and accurate air path parameters, the CJ3000 uses computer-aided design software to create a 3D model. Assigning the total engine weight obtained is a feasible method of structurally fitting the CJ3000 design. Throughout the design process, the parameters obtained in the CAD model will be entered into the self-programmed Excel and Matlab combined program. The CJ3000 vibration characteristics (including critical speed, natural frequency, and mode shape) can be obtained later. The results of the calculation will serve as an important reference for the CJ3000 to further optimize. Finally, the overall structural design and 3D model of the CJ3000 engine, as well as details of certain structural designs, will be identified and presented in this chapter.

12.1 Component Material Selection

Performance-driven and cost-driven are the two major driving forces for the development of materials technology. The performance design of the CJ3000, as well as the development trend of aerospace materials when the CJ3000 is put into use in 2025, needs to be considered. Silicon Carbide Fiber Reinforced Ceramic Matrix Composites (SiC/SiC CMC), Continuous Silicon Carbide Fiber Reinforced Titanium Matrix Composites(SiCf/Ti), 4th Generation Organic-Inorganic Hybrid P^2SI 900HT Polyimide Composites, PST TiAl Intermetallic Compound single crystals will be considered for putting into use in the specific structure of CJ3000.
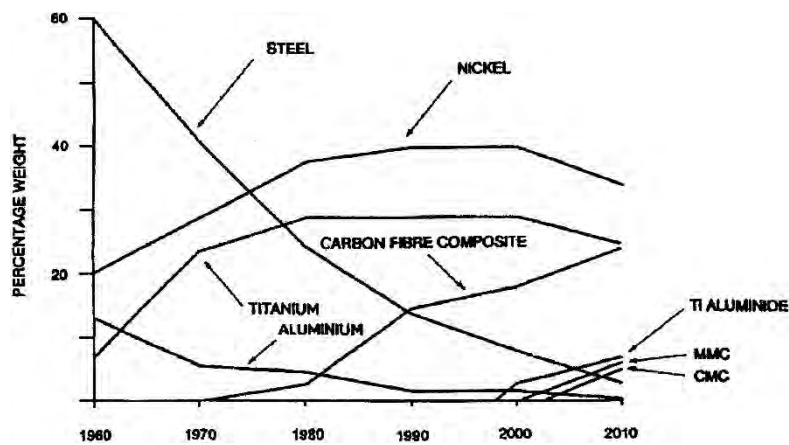
Figure 12.1 Trends in Civil Gas Turbine Material Usage [37]
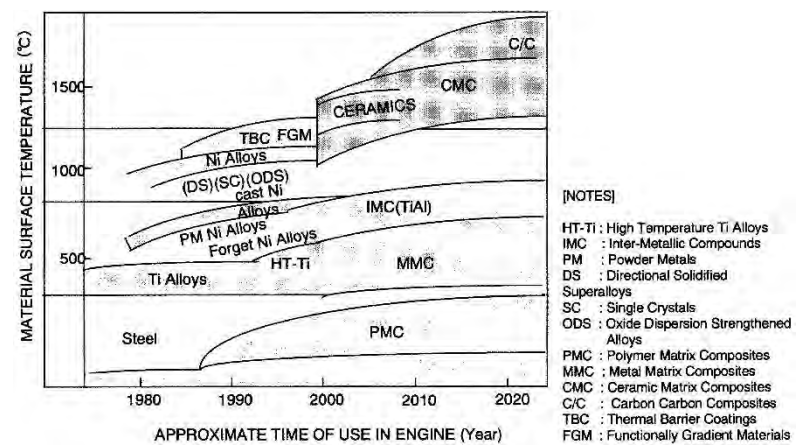
Figure 12.2 Trends in Development of High Temperature Turbine Materials [37]

12.1.1 Ceramic Matrix Composites

Due to its fascinating high-temperature performance, low density, and reliable testing of engine durability, ceramic matrix composites have been widely used in engines such as Trent and LEAP [39] and have accumulated considerable service life. Among them, the most promising silicon carbide fiber-reinforced CMCs have lower oxidation rates compared to C/SiC and C/C CMCs at temperatures above 400°C[38]. It will be considered for use in the combustion chamber, turbine guide vanes, turbine blades, and tail nozzles of CJ3000 engine. The properties of CMC materials used in the design are as follows:

Table 12.1 Material Properties of SiC/SiC Ceramic Matrix Composite

Material Property	Value
Max Service Temperature (°R)	3160
Density (lb · in^{-3})	0.0903
Tensile Strength (ksi)	46.56
Young's Modulus (msi)	41.3

12.1.2 TiAl Intermetallic Compounds

In 2016, Prof. Chen Guang from Nanjing University of Science and Technology of China successfully manufactured PST monocrystalline materials (Ti-45Al-8Nb PST single crystals) with extremely low production costs.

It has a ductility of 6.3-7.6% and a high strength of 930-10,030 MPa at ambient temperature. In addition, they show good creep resistance at high temperatures of 900°C and the creep life and minimum creep rate are better than those of commercial 4822 TiAl polycrystalline materials by more than an order of magnitude - indicating their remarkable service environment at high temperatures potentiality [41]. It will be considered for use in the CJ3000 third and fourth stage turbines. The material properties used in the design are as follows:

Table 12.2 Material Properties of Ti-45Al-8Nb PST Single Crystals

Material Property	Value
Max Service Temperature (°R)	2100
Density (lb · in^{-3})	0.1409
Tensile Strength (ksi)	92.39
Young's Modulus (msi)	20.305

12.1.3 Titanium-Based Metal Matrix Composites

Continuous fiber reinforced titanium matrix composites have the advantages of high specific strength, high specific rigidity, good fatigue resistance, and an average increase in substrate use temperature of 200° C., which are much higher than nickel-base superalloys, steels, aluminum, and titanium-aluminum intermetallic compounds. The fatigue performance of SiCf/Ti-based composites is significantly higher than that of titanium alloys, especially at high temperature. The fatigue strength in the low-cycle fatigue zone and the high-cycle fatigue zone is at least 100% higher than that of the base material.

The use temperature of the SCS-6/Ti2AlNb composite reaches 760°C [44]. The design of the CJ3000 will consider its application to rotors and stators below 600°C. The material properties used in the design are as follows:

Table 12.3 Material Properties of SiCf/Ti Composites

Material Property	Value
Max Service Temperature (°R)	1570
Density (lb · in^{-3})	0.1409
Tensile Strength (ksi)	246.56
Young's Modulus (msi)	31.18

12.1.4 Polyimide Composites

Polyimide resin has excellent heat resistance and mechanical properties and has always been the focus of research on aero engine high temperature resistant composite materials. The long-term working temperature of the epoxy resin is not higher than 130°C, the bismaleimide resin is 150-230°C, and the polyimide resin can be used in the range of 280-450°C.

The fourth generation of organic-inorganic hybrid polyimide composite resin matrix P2SI900HT with a temperature resistance of 450°C has initially formed a material grade. Its glass transition temperature is as high as 489°C (Tanδ) and it can be used over 425°C for a long time and can be used at 815°C. Use it for a short time. Polyimide material usually has a density of 1.3~1.7g/cm3. The properties of P2SI900HT polyimide composite material used in CJ3000 design are as follows:

Table 12.4 Material Properties of P2SI900HT Composites [49]

Material Property	Value
Max Service Temperature (°R)	1256
Density (lb · in⁻³)	0.04805
Tensile Strength (ksi)	287
Young's Modulus (msi)	20

12.1.5 Nickel-Base Superalloy

The material selection of each part of the CJ3000 will use the four advanced aerospace materials described above. At the same time, the nickel-based superalloy is used as the main material of the turbine disk and the high-temperature bearing parts. The nickel-based superalloy has excellent comprehensive performance at medium and high temperatures and is suitable for working under high temperature for a long time.

For the turbine disk, the developed third-generation powdered nickel-base superalloy has excellent strength and damage tolerance, such as Alloy 10 and RR1000, Rene 104 (ME3), etc., with higher strength and lower fatigue crack growth rate [50]. The properties of nickel-based superalloy materials used in the CJ3000 design (mainly referred to Inconel 718) are as follows:

Table 12.5 Material Properties of Nickel-base Superalloy

Material Property	Value
Max Service Temperature (°R)	1660
Density (lb · in⁻³)	0.2984
Tensile Strength (ksi)	159.54
Young's Modulus (msi)	23.206

The material usage of the various parts of the CJ3000 will depend on their operating temperature and the location in the route that passes the engine's forces. Among other components, TMMC is used for internal- and low-pressure shafts, NS is used for high-pressure shafts, CMC materials are used for diffusers and combustion chambers, and NS and CMC are used together for turbine casing and mixing chambers, and tail nozzles. PC materials are used for bypass duct casing.

In the following text, abbreviations will be used in place of the above five materials. PC - Polyimide Composites, TMMC - Titanium Matrix Composites, CMC - Ceramic Matrix Composites, PST-TA - Polysynthetic Twinned TiAl Single Crystals for High-Temperature Applications, NS - Nickel-Base Superalloy.

12.1.6 Blade Structure Analysis

The strength of the blades will be verified according to the Eq. 12.1 and Eq. 12.2 [51]:

$$A = 2\pi r_m (r_t - r_h) \tag{12.1}$$

$$\sigma_c = \frac{\rho_{blade}\omega_{shaft}^2 A}{4\pi}\left(1 + \frac{A_t}{A_h}\right), \ \sigma_t = \alpha E \Delta T \tag{12.2}$$
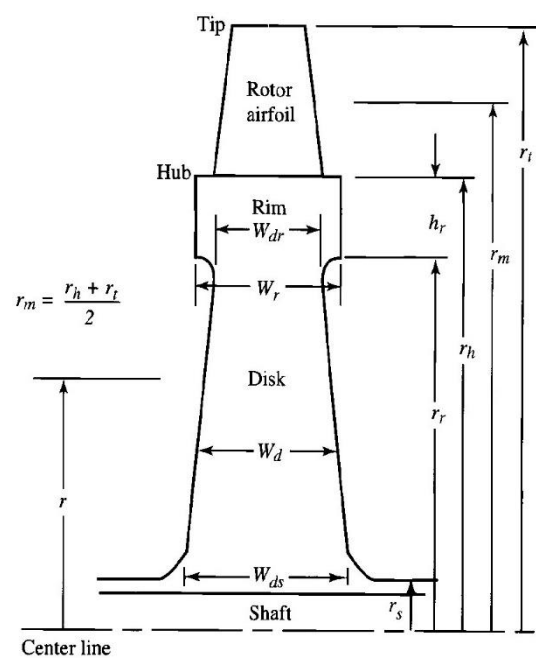
Figure 12.3 Turbomachinery Rotor Nomenclature

σ_c – Centrifugal stress, σ_t - Thermal stress, α - Coefficient of linear expansion, E - Modulus of elasticity, ΔT - Temperature change value.

Due to:

$$AN^2 = \omega_{shaft}^2 A(30/\pi)^2 \tag{12.3}$$

AN^2 can be used to measure the stress of the blade：

$$AN^2 = \frac{3600\ \sigma_c}{\pi(1 + A_t/A_h)\rho_{blade}} \tag{12.4}$$

The results of the calculation of the maximum blade stress for each material are shown in the following table (with taper ratio 0.8):

Table 12.6 CJ3000 Turbine Blade Stress Analysis

Material	Max σ_{total} Component	σ_c /ksi	σ_t /ksi	Max σ_{total} /ksi	AN^2 $(in^2 s^{-2})$	Allowable Stress /ksi	MS
NC	HPT S1	—	-68.79	68.79	5.68×10^{10}	159.54	1.319
CMC	HPT R1	7.919	-22.58	14.66	4.99×10^{10}	46.56	2.177
PST-TA	LPT S4	14.48	-9.51	4.97	8.66×10^9	92.39	17.604

Table 12.7 Centrifugal Stress Analysis of CJ3000 Compressor Blades

Material	Blade of Max σ_c	Allowable σ_C/ksi	Material Density $\rho/lb \cdot in^{-3}$	Taper Ratio A_t/A_h	Flow Area /in²	Shaft Speed ω /rpm	Design Max σ_c /ksi	MS
TMMC	IP-R1	246.56	0.1409	0.8	788.76	7800	27.508	7.96
PC	Fan R1	287	0.04805	0.8	5765.46	4000	18.033	14.915
NS	HP-R3	159.54	0.2984	0.8	124.54	12000	21.72	6.345

By selecting five aerospace materials further developed on the basis of long-term service, the CJ3000 conceptual design is well controlled at a level of 11250 *lbm*, compared to the Trent 800 series (13100 *lbm*) and the Trent 900 series (13800 *lbm*). The current civil triple-rotor aeroengines (static thrust of 50,000 to 80,000 *lbf*), such as the Trent 1000 Series (11,900 *lbm*), are very impressive.

After that, the calculation of the vibration characteristics and the optimization of the structural scheme will be performed using the CAD software Solidworks and self-programmed programs based on the above evaluation.

Precondition: cruise working speed is 12000/7800/4000 rpm.

Table 12.8 Blade Strength Calculation Details

Part Name	Fan R1	Fan S1	Fan R2	Fan S2	IP R1	IP S1	IP R2	IP S2	IP R3	IP S3	IP R4	IP S4
Material	PC	PC	PC	PC	TMMC	TMMC	TMMC	TMMC	TMMC	TMMC	TMMC	TMMC
Operating Temperature/R	634	651.66	730.64	748.93	826.47	844.9	921.07	939.89	1016.59	1035.59	1112.8	1131.92
Flow Area/in^2	5765.46		4139.06		788.76		602.82		478.83		391.02	
Design σ_c	1.80E+4		1.29E+4		2.75E+4		2.10E+4		1.67E+4		1.36E+4	
MS	14.92		21.17		7.96		10.73		13.76		17.08	

Part Name	IP R5	IP S5	HP R1	HP S1	HP R2	HP S2	HP R3	HP S3	HP R4	HP S4
Material	TMMC	TMMC	TMMC	TMMC	TMMC	TMMC	NS	NS+CMC	NS	NS+CMC
Operating Temperature/R	1209.63	1227.92	1341.05	1370.03	1498.19	1527.94	1657.21	1687.38	1817.7	1848.18
Flow Area/in^2	319.11		285.62		162.28		124.54		105.80	
Design σ_c	1.11E+4		2.36E+4		1.34E+4		2.17E+4		1.85E+4	1.11E+4
MS	21.15		9.46		17.41		6.35		7.65	21.15

Part Name	HPT S1	HPT R1	IPT S1	IPT R1	LPT S1	LPT R1	LPT S2	LPT R2	LPT S3	LPT R3	LPT S4	LPT R4
Material	NS+CMC	CMC	NS	CMC	NS	CMC	CMC	CMC	CMC	PSTTA	CMC	PSTTA
Operating Temperature/R	3214.96	2820.20	2659.5	2347.95	2306.52	2220.07	2151.79	2072.68	2003.47	1922.6	1851.98	1767.76
Design σ_c/ksi		7.92E+3		6.38E+3		3.61E+3		4.09E+3		1.07E+4		1.45E+4
Design σ_t/ksi	-6.88E+4	-2.26E+4	-5.41E+4	-1.66E+4	-1.50E+4	-4.90E+3	-5.68E+3	-4.90E+3	-2.74E+3	-9.28E+3	-2.80E+3	-9.51E+3
Design σ_{total}/ksi	6.88E+4	1.47E+4	5.41E+4	1.03E+4	1.50E+4	1.30E+3	5.68E+3	8.08E+2	2.74E+3	1.39E+3	2.80E+3	4.97E+3
AN^2/in^2s^{-2}	5.68E+10	4.99E+10	4.47E+10	3.49E+10	5.11E+10	4.41E+9	1.93E+10	2.75E+9	9.32E+9	2.43E+9	9.53E+9	8.66E+9
MS	1.32	2.18	1.95	3.54	2.10	34.91	7.20	56.64	15.99	65.30	15.62	17.60

12.2 Whole Engine Vibration Characteristic Calculation Program

The program used to process the conceptual design information, calculate the vibration characteristics of the engine (including the casing) and display the vibration mode is called " Procedure Dedicated to Vibration Characteristics of Complex Structure Aeroengine " (PDVCCA). It was written by "The Little Boys" team using Excel and Matlab tools. Before the program is run, the 3D model built according to the CJ3000 concept design (described in Section 12.4) will provide the parameters for entering the program. After the Matlab calculation, the output will be displayed in Excel, and Matlab will output the mode shape image of the CJ3000 according to the preset requirements. These results will provide strong help for "The Little Boys" team to choose the CJ3000 support program.

12.2.1 Calculation Principle

Considering the weight of the bare machine, the internal and external casings will be included in the evaluation range of the vibration characteristics and form a complex vibration system with the three rotors. Therefore, the substructure transfer matrix method will be used to evaluate the overall machine vibration characteristics of the CJ3000 and divide the CJ3000 into five substructures: a low-pressure rotor, an intermediat-pressure compressor, a high-pressure rotor, a core machine casing, and a bypass casing.

For each individual sub-structure, the use of the transfer matrix method will divide them in the axial direction (left to right in the airflow direction) into tens of axisymmetric sections. Each side of the section has four state parameters X, θ (positive anti-clockwise direction), M (positive rotation axis is positive) and Q (shaft recovery torque is positive), they are characterized on the cross-section displacements, corners, moments and shears:

$$P = [X\ \theta\ M\ Q]^T \tag{12.5}$$

The state parameters of the right section of the shaft section will be calculated by passing the state parameters of the left section through the shaft section. This calculation process will be implemented in the form of a matrix. Each axis segment can be divided into four types based on the geometric and mass characteristics. The mass station, the roulette station, the elastic hinge station, and the elastic support station are integrated. In practice, their transfer matrix is combined with massless shaft segments, which are collectively expressed as:

$$T = \begin{bmatrix} T_{11} & T_{12} & T_{13} & T_{14} \\ T_{21} & T_{22} & T_{23} & T_{24} \\ T_{31} & T_{32} & T_{33} & T_{34} \\ T_{41} & T_{42} & T_{43} & T_{44} \end{bmatrix} = \begin{bmatrix} 1+\frac{l^3(1-\nu)}{6EI}(m\Omega^2-k) & l\left[1+\frac{l}{2EI}(J\Omega^2+C_b)\right] & \frac{l^2}{2EI}+\frac{l}{C_h} & \frac{l^3}{6EI}(1-\nu) \\ \frac{l^2}{2EI}(m\Omega^2-k) & 1+\frac{l}{EI}(J\Omega^2+C_b) & \frac{l}{EI}+\frac{l}{C_h} & \frac{l^2}{2EI} \\ \left[l+\frac{l^3(1-\nu)N}{6EI}\right](m\Omega^2-k) & Nl+\left(1+\frac{l^2N}{2EI}\right)(J\Omega^2+C_b) & \frac{Nl}{C_h}+1+\frac{l^2N}{2EI} & l+\frac{l^3(1-\nu)N}{6EI} \\ m\Omega^2-k & 0 & 0 & 1 \end{bmatrix} \tag{12.6}$$

In Eq. 12.6 :l - shaft length, ν - shear effect coefficient, m - concentrated weight, Ω- precession angle frequency, k -elastic support lateral stiffness, E - elastic modulus, I - section moment of inertia, J - equivalent moment of inertia, C_b - Angle stiffness of elastic support, C_h - bending stiffness coefficient of hinge, N - axis force.

The gyro moment is generated when the wheel rotates, which is related to the mass m of the disc and the moment of inertia J:

$$J = \left(\frac{J_p\omega}{J_d\Omega}-1\right)J_d\Omega^2 \tag{12.7}$$

J_d is the moment of inertia of the disc, J_p is the polar moment of inertia of the disc, and when the disc thickness H is significantly less than the diameter D $\left(H/D \leq 1/4\right)$:

$$J = \left(\frac{2\omega}{\Omega} - 1\right) J_d \Omega^2 \tag{12.8}$$

When the shear effect and axial force are not taken into consideration, the elastic support has no angular stiffness, and there is no elastic hinge in the structure: $v = 0$, $N = 0$, $C_b = 0$, $1/C_h \to 0$. The comprehensive shaft transfer matrix becomes:

$$T = \begin{bmatrix} 1 + \frac{l^3}{6EI}(m\Omega^2 - k) & l\left[1 + \frac{l}{2EI}J\Omega^2\right] & \frac{l^2}{2EI} & \frac{l^3}{6EI} \\ \frac{l^2}{2EI}(m\Omega^2 - k) & 1 + \frac{l}{EI}J\Omega^2 & \frac{l}{EI} & \frac{l^2}{2EI} \\ l & J\Omega^2 & 1 & l \\ m\Omega^2 - k & 0 & 0 & 1 \end{bmatrix} \tag{12.9}$$

Therefore, when dealing with the CJ3000 model, it is necessary to obtain the elastic modulus E, the moment of inertia I, the length l, the mass m, and the moment of inertia J of each shaft segment, and the value of their stiffness k is also required at the places where they are supported. This is the significance of the previous work on selecting materials.

For the start and end of each matrix transfer, for the convenience of calculation and understanding, a massless free end of length 0 ($10^{-7}in$) is set, and its state parameters satisfy:

$$P = [X\ \theta\ 0\ 0]^T \tag{12.10}$$

The state parameter of the right-most cross-section of the rotor can be represented by the transfer matrix as a function of the left-most section state parameter:

$$P_R = \begin{bmatrix} X \\ \theta \\ 0 \\ 0 \end{bmatrix}_R = T_n \begin{bmatrix} X \\ \theta \\ M \\ Q \end{bmatrix}_{n-1} = T_n T_{n-1} \begin{bmatrix} X \\ \theta \\ M \\ Q \end{bmatrix}_{n-2} = \prod_{i=1}^{n} T_i \begin{bmatrix} X \\ \theta \\ M \\ Q \end{bmatrix}_L = T \begin{bmatrix} X \\ \theta \\ 0 \\ 0 \end{bmatrix}_L = T \cdot P_L \tag{12.11}$$

R - end face at the end of the right side, L - end face at the left side.

Since both the beginning and the end are unconstrained, there are:

$$\begin{cases} M_R = T_{31}X_L + T_{32}\theta_L = 0 \\ Q_R = T_{41}X_L + T_{42}\theta_L = 0 \end{cases} \tag{12.13}$$

Therefore, the essence of this method is to multiply the front end (the left side of the shaft segment) by a matrix and transfer it to a known amount to the right of one shaft segment. In turn, the known quantity is used to solve the unknown process. To make X_L and θ_L not be zero at the same time,

$$\Delta T = \begin{vmatrix} T_{31} & T_{32} \\ T_{41} & T_{42} \end{vmatrix} = 0 \tag{12.14}$$

Since the elements in T are all functions of the rotational angular frequency ω and the precession angle frequency Ω, the solution equation gives the single rotor's critical speed/natural frequency.

After successfully applying the transfer matrix method to deal with each sub-structure, all the sub-structures of the system are to be linked together. The coupling relationship that is mainly considered is the lateral force R transmitted by the intermediate support. There are coupling conditions on the connected sections:

$$\begin{cases} R_{inner} = -R_{outer} \\ (X_{inner} - X_{outer}) + R_{inner}/k = 0 \end{cases} \tag{12.15}$$

For such a coupling section, unknown conditions can be associated with well-known cross-section parameters. For the free end:

$$P_R = \begin{bmatrix} X \\ \theta \\ 0 \\ 0 \end{bmatrix}_R = \prod_{i=1}^{n} T_i \begin{bmatrix} X \\ \theta \\ 0 \\ 0 \end{bmatrix}_l + \prod_{j=c}^{n} T_j \begin{bmatrix} 0 \\ 0 \\ 0 \\ R \end{bmatrix}_c = T_{LR} \begin{bmatrix} X \\ \theta \\ 0 \\ 0 \end{bmatrix}_l + T_{cR} \begin{bmatrix} 0 \\ 0 \\ 0 \\ R \end{bmatrix}_c = T_{lR} \cdot P_l + T_{cR} \cdot P_c \tag{12.16}$$

l - Free end with unknown condition and backwards pass; c - Support coupling point with unknown condition and backward pass;
n - Number of axis segments from free end l to free end R.

Then:

$$\begin{cases} M_R = T_{lR31}X_l + T_{lR32}\theta_l + T_{cR34}R_c = 0 \\ Q_R = T_{lR41}X_l + T_{lR42}\theta_l + T_{cR44}R_c = 0 \end{cases} \tag{12.17}$$

For bearing coupling points:

$$P_C = \begin{bmatrix} X \\ 0 \\ 0 \\ 0 \end{bmatrix}_C = \prod_{i=1}^{m} T_i \begin{bmatrix} X \\ \theta \\ 0 \\ 0 \end{bmatrix}_l + \prod_{j=c}^{m'} T_j \begin{bmatrix} 0 \\ 0 \\ 0 \\ R \end{bmatrix}_c = T_{lC} \begin{bmatrix} X \\ \theta \\ 0 \\ 0 \end{bmatrix}_l + T_{cC} \begin{bmatrix} 0 \\ 0 \\ 0 \\ R \end{bmatrix}_c = T_{lC} \cdot P_l + T_{cC} \cdot P_c \tag{12.18}$$

m - the number of shaft segments from the free end l to the coupling point C; m'- the number of shaft segments from the front coupling point c to the coupling point C.

Thus:

$$X_C = T_{lC11}X_l + T_{lC12}\theta_l + T_{cC14}R_c \tag{12.19}$$

Take Eq. 12.19 to $(X_{inner} - X_{outer}) + R_{inner}/k = 0$, and then combine Eq. 12.17 to create a coupled equation of motion for the complex structure and extract the frequency equation:

$$\Delta T = \begin{vmatrix} T_{lR31} & \cdots & T_{cR34} \\ \vdots & \ddots & \vdots \\ T_{lC11} & \cdots & T_{cC14} \end{vmatrix} = 0 \tag{12.20}$$

As with Eq. 12.14, the solution of Eq. 12.20 obtains critical speeds and natural frequencies of complex systems.

12.2.2 Case validation

For the general case of solving the critical speed, it is necessary to obtain the natural frequencies of the system at different operating speeds and connect these data points to form a natural frequency characteristic diagram. After that, the speed line is drawn on this graph. The intersection of the speed line and the natural frequency curve on the diagram is the critical speed of each stage of the entire system (Figure 12.4).

However, for the CJ3000's vibration characteristics evaluation program PDVCCA, if the rotational speed relationship between different rotors is obtained, using expressions to convert the symbols of multiple unknown frequencies into one, the process of plotting points can be omitted and the results can be obtained directly. This is significant for a three-rotor engine because a three-dimensional natural frequency map is much harder to compute than a map with only two axes.
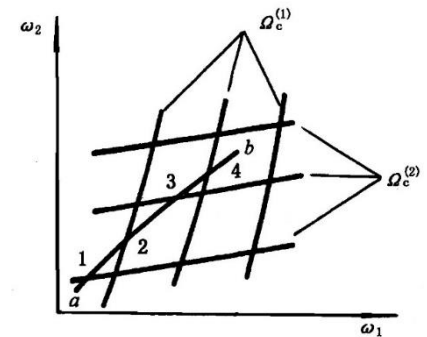
Figure 12.4 The Map of Critical Speed Characteristics of Double Rotors

Before starting the design of the CJ3000, the PDVCCA was used to compare the two computational needs of the same problem in textbooks and a dissertation. Numerical and graphical results show the reliability of the PDVCCA calculations. The title gives a case in point: a dual-rotor system with two intermediate supports. The rotor characteristics are shown in Figure 12.5 and other conditions are given in the Ref. 53.

(A) Structure Diagram   (B) Calculation Model
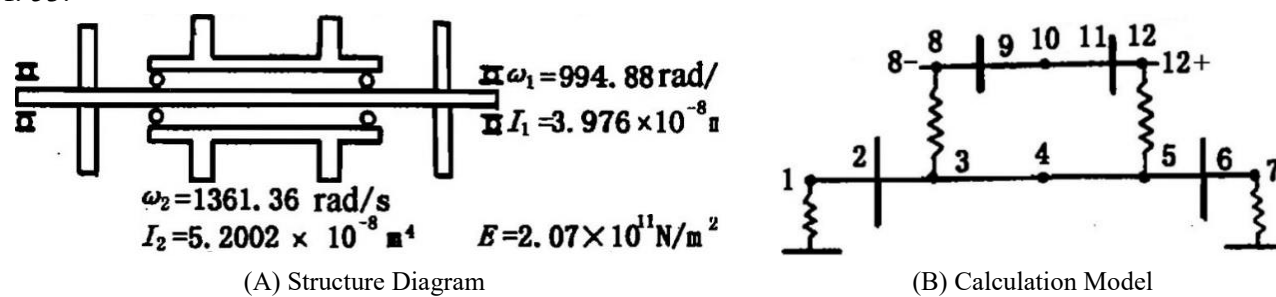
Figure 12.5 Double Rotor System with Two Intermediate Supports [53]

The PDVCCA solution for the natural frequency and the solution given by the literature program and the Lagrange analytical solution are compared in Table 12.8: (B is the reverse whirl, F is the positive whirl)

Table 12.8 Comparison Of PDVCCA Calculations On Natural Frequencies (rad/s)

PDVCCA Solution	B 174.713	F 400.441	B 518.674	B 632.999	F 894.415	B 1349.947
Manual Program Solution	B 174.723	F 400.436	B 518.678	B 632.982	F 894.408	B 1349.972
Lagrangian Solution	B 174.716	F 400.436	B 518.674	B 632.988	F 894.410	F 1349.958
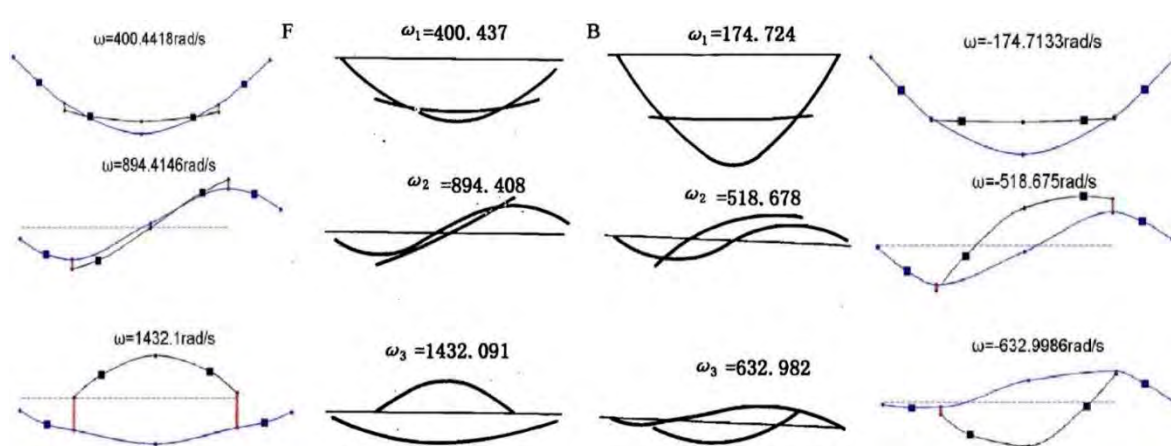
Figure 12.6 Comparison of Mode Shapes of PDVCCA With Respect to Natural Frequencies

In order to further reflect the reliability of the calculation results, the PDVCCA mode shape display function was used to compare with the vibration mode at the same natural frequency given in the literature.

In a Ref. 54, a more in-depth study of this case was made. In this case, the critical speed of the example was calculated after giving the relationship between the rotational speed of two rotors $\omega_2/\omega_1 = 1.37$. PDVCCA also accurately reproduced his results

Table 12.9 Comparison of PDVCCA Calculations on Natural Frequencies

rad/s	Internal Rotor Synchronization			External Rotor Synchronization		
	1st	2nd	3rd	1st	2nd	3rd
Literature Results	319.7154	881.3916	1509.5998	307.6482	847.2947	1445.1076
PDVCCA Results	319.4531	881.3876	1508.6648	307.4097	847.2917	1443.9703

12.3 Aeroengine Structural Scheme Case

The CJ3000, as a civilian hybrid three-rotor engine for supersonic operation, has unique structural design requirements and lacks identical cases. Therefore, its structural scheme is optimized based on many existing engines. The evolution of three-rotor engines such as the RB211 and Trent 1000 is a reference point.

12.3.1 RB211& RB199

The RB211 is the first three-rotor turbine engine to be put into use. Rolls-Royce has paid a huge price for its successful development. Its three-rotor structure allows each rotor to operate at its optimum tip speed. Compressor efficiency is high and the number of stages is small. This is one of the important reasons why the CJ3000 chooses a three-rotor structure.
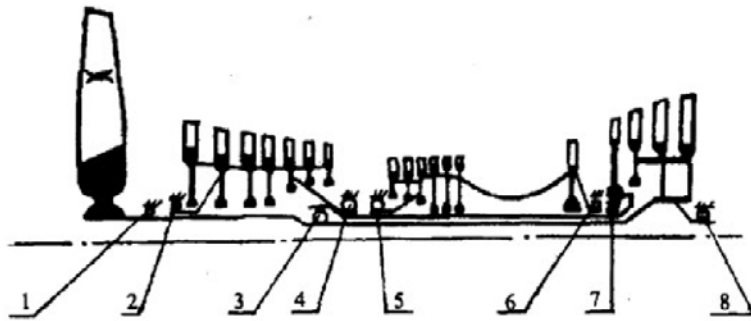
Figure 12.7 RB211 Engine Rotor Support Scheme
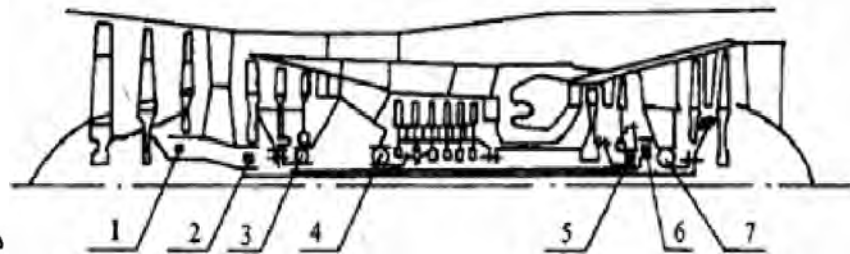
Figure 12.8 RB199 Engine Schematic

Table 12.10 RB211 Engine Rotor Solution

Rotor	Support Plan	Compressor / Turbine Stages	Design Features
LP	0-2-1	1:3	Thrust bearing (No. 3): an intermediate bearing, is difficult to assemble and lubricate.
IP	1-2-0	6:1	The thrust bearing:4th fulcrum. The compressor short shaft is fixed on the middle stage disc, and the internal pressure turbine disc uses the "anti-C" structure.
HP	1-0-1	6:1	Compressor short shaft fixed to middle wheel.

The three thrust bearings of the RB211 are concentrated in internal-pressure and high-pressure compressor intermediate casing. The transmission path is short. This is a typical bearing structure for a three-rotor engine. The RB211's casing is a two-layer structure that effectively separates the airflow path from the deformation of the load-bearing structure and effectively maintains the tip clearance of the core machine [55].

The RB199 is the first engine to use a three-rotor structure in a small bypass ratio turbofan engine. Compared with the RB211 engine, the RB199 uses an intermediate fulcrum located behind the high-pressure turbine, and an inter-stage turbine load bearing frame is placed in the low-pressure turbine guide, reducing the number of load-bearing frames for the entire engine to three. What is more unique is that its low-pressure rotor thrust bearing is located in front of the low-pressure turbine.

Table 12.11 RB199 Engine Rotor Solution

Rotor	Support Plan	Compressor / Turbine Stages	Design Features
LP	0-3-0	3:2	Thrust bearing: No. 7, at the front of the low-pressure turbine
IP	0-1-1	3:1	Thrust bearing: No. 3. No support before the compressor.
HP	1-0-1	6:1	The intermediate bearings: at the rear of the high-pressure turbine

12.3.2 Trent Series

The Trent 1000 engine is the sixth model of RR's Trent series engine and has a supporting solution that is consistent with the RB211. However, the rear fan support is a roller bearing, and there is a risk that the fan disk will be thrown after the fan shaft is broken[56].
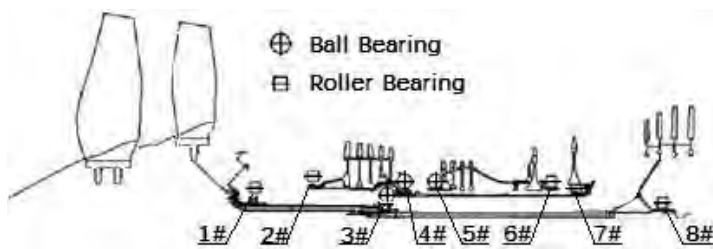
Figure 12.9 Trent 1000 Engine Rotor Schematic

Table 12.12 Trent 1000 Engine Rotor Scheme

Rotor	Support Plan	Compressor / Turbine Stages
LP	0-2-1	1:6
IP	1-2-0	8:1
HP	1-0-1	6:1

Trent 1000's turbine load bearing frame is arranged between high pressure and internal pressure turbines. The temperature load and the ambient pressure are very high. Therefore, it is difficult to seal the air system and design heat protection.

The design of the Trent XWB engine is quite different from that of the previous RB211/ Trent series. The large-size ball bearing behind the fan solves the problem that the RB211 series engine fan retention system is not perfect.

12.3.3 PW4000

The PW4000 engine was developed by Pratt & Whitney in late 1982. A roller bar bearing was added after the fan thrust ball bearing, which solved the problem of low-pressure rotor rigidity. The 1-1-0 high pressure support scheme design has good vibration characteristics for two-stage high pressure turbine engines [55].

Table 12.13 PW4000 Engine Rotor Solution

Rotor	Support Plan	Compressor / Turbine Stages
LP	0-2-1	1 (+4-stage booster):4
HP	1-1-0	11:2
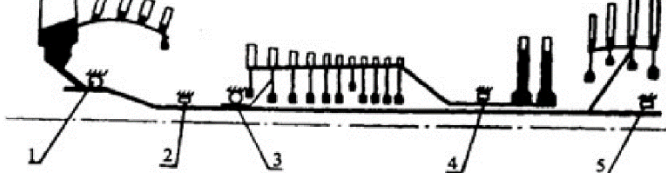
Figure 12.10 PW4000 Engine Rotor Support Scheme

12.3.4 GEnx

The high-pressure rotors of GE's GE90 to GEnx series of engines all use 1-0-1 two-point support. Separate high- and low-pressure turbine bearing frames are provided for the high-pressure rear bearing to avoid excessive distances between the middle bearing and the low-pressure turbine fulcrum (requirements for the smooth transition of the local gas line), which will make the coupling effect between high and low-pressure rotors too large [57].
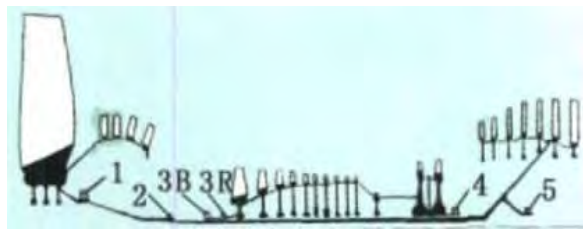
Figure 12.11 GEnx Engine Rotor Support Solution

Table 12.14 GEnx Engine Rotor Scheme

Rotor	Support Plan	Compressor / Turbine Stages
LP	0-2-1	1 (+4-stage booster):7
HP	1-1-0	10:2

12.4 CJ 3000 Overall Structure Design

Based on the characteristics of RR, PW, and GE engine support schemes, CJ3000 initially performs structural design. It is difficult to arbitrarily modify the specific structure in the actual design of the engine, so the overall structural scheme is determined by the evaluation and optimization of the vibration characteristics.

12.4.1 Original Design & CAD Model Creation

In the initial design of the CJ3000, the first version of the support scheme was determined primarily from the perspective of avoiding the placement of high-temperature load-bearing components. The main features of the CJ3000 were the use of high-pressure turbine front bearings and internal-low-pressure turbine bearing frames. Because the CJ3000 is a medium by-pass ratio engine, there are three more rigid coupling points between the internal and external gearboxes. They are located in the fan-internal pressure compressor bearing frame, the internal pressure-high pressure compressor bearing frame, and the high pressure- internal pressure turbine bearing frame. The mounting section of the engine is located at the fan-internal pressure compressor internal load bearing frame and the high pressure turbine-internal pressure turbine inter-stage bearing frame to reduce the force transmission route. The specific results are as follows:

(a) Rotor support scheme   (b) CAD model section view
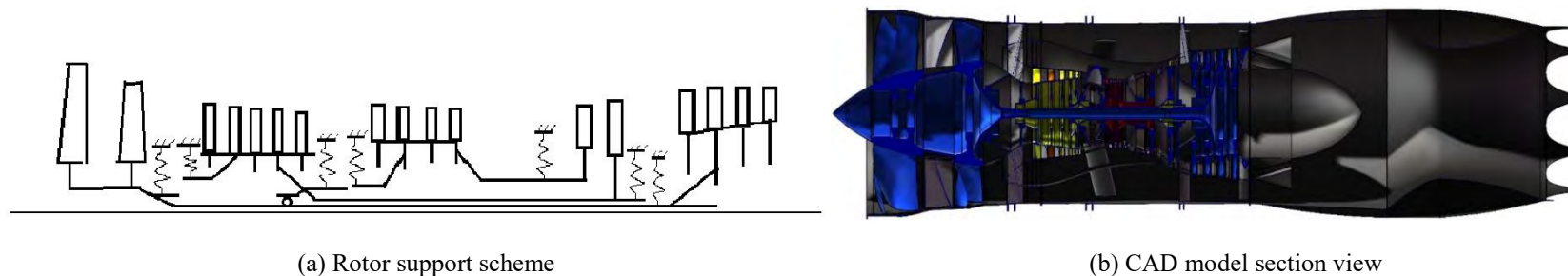
Figure 12.12 Original Design of CJ3000 Engine

Table 12.15 CJ3000 Engine Rotor Scheme

Rotor	Support Plan	Compressor / Turbine Stages
LP	0-3-0	2:4
IP	1-1-1	5:1
HP	1-1-0	4:1

12.4.2 Model Parameters

The model of the CJ3000 is divided into 74 stations. With a large data amount, only the general situation listed in the report. :

Table 12.16 CJ 3000 Engine Transfer Matrix Model Parameters

	LP Rotor	IP Rotor	HP Rotor	Core Machine Casing	Bypass Duct Casing
Substructure Weight (lbm)	5386.7	536.91	271.16	1792.03	2277.26
Section Inertia Moment (in^4)	75.68~528.55	38.2~226.8	31.47~94.18	0.769~4.16×10^5	1.22~2.93×10^6
Elasticity Modulus (msi)	20.31~31.18	23.21~31.18	$(1.6$~$1.8)\times 10^{11}$	$(1.4$~$2.96)\times 10^{11}$	$(1.4$~$2.96)\times 10^{11}$
Structure Number	13	18	13	16	14
Axial Length (in)	2.91~33.7	1.1~34.84	0.63~5.91	2.56~53.19	3.74~88.19

12.4.3 Rotational Speed Relation and Critical Speed Margin of Safety

CJ3000 analyzed the speed of four working conditions:

Table 12.17 CJ 3000 Working Point Speed

		Design Point			
		1.6 Ma	1.129 Ma	0.25 Ma	0 Ma
Shaft Speed	N3 (HP)/rpm	12000 (1×N3)	10920 (1×N3)	11461 (1×N3)	11149 (1×N3)
	N2 (IP)/rpm	7800 (0.650×N3)	7058 (0.646×N3)	7447 (0.650×N3)	7256 (0.651×N3)
	N1 (LP)/rpm	4000 (0.333×N3)	3513 (0.322×N3)	3680 (0.321×N3)	3662 (0.328×N3)

The working speed relation of CJ3000 is determined.

$$\begin{cases} \omega_1 = 0.33 \times \omega_3 \\ \omega_2 = 0.65 \times \omega_3 \end{cases} \tag{12.21}$$

The four working points determine a wide range of working speed, and the value of the critical speed of the system should be avoided when the working speed of all the above cases is guaranteed to be 20% margin of safety.

Table 12.18 CJ3000 Critical Speed Regulation Range (0.2 MS)

Rotor	Working Speed Range /rpm	Avoidance Value /$rad \cdot s^{-1}$
HP	10920~12000	914.83~1507.96
IP	7058~7800	591.31~980.18
LP	3513~4000	294.32~502.65

The rotational speed relation can be used directly in the PDVCCA. The critical speed of the high-pressure rotor, the internal pressure

rotor and the low-pressure rotor can be obtained separately according to the unknowns of the retained precession frequency. The critical speed at this time is the inherent characteristics of different systems with different excitation, so the margin of corresponding excitation source needs to be satisfied.

12.4.4 Rotor Steering Analysis

The Trent series has a customary counter rotating design of high pressure rotor and internal pressure rotor. For the dual rotor engine's overall structure design, counter rotating can reduce the first stage low pressure turbine guide vane so as to reduce engine quality. At the same time, due to the effect of the gyroscopic moment, the axis is more easily deformed when the reverse rotation is rotating. By the reasonable support design, the dual rotor system can work in the speed range far away from the resonance frequency. But the critical speed of three rotor engine still needs to be verified.

Table 12.19 Critical Speed of CJ3000 High Pressure Rotor with Different Steering Conditions

rad/s	1st	2nd	3rd	4th	5th	6th	7th	8th	9th	10th
Same Direction	148.707	182.06	267.096	330.398	376.524	590.928	799.439	1001.166	1468.243	2073.36
HP Reversal	122.285	174.438	241.532	267.546	321.547	459.537	573.43	634.78	1000.615	1467.81
IP Reversal	147.755	179.658	262.436	305.55	375.431	476.975	598.816	796.005	1000.686	1467.817
LP Reversal	122.599	177.34	241.614	276.946	339.639	541.078	648.602	1001.106	1468.23	2073.36

The opposite direction of rotation makes the gyro torque of different rotors cancel, weakening the rigidity of the rotor and reducing the critical speed, but the effect is not obvious. When the high-pressure rotor and internal-pressure rotor reverse, there adds a new critical speed. Considering the mature steering scheme, the selection of the CJ3000 support scheme will be determined first according to the calculation results of the same direction rotation. The final calculation value of the critical speed will consider the design of the high-pressure rotor steering and the opposite direction of the middle and low-pressure rotor.

12.4.5 Scheme Optimization

The calculation results of the critical speed of the original scheme synchronized with different rotors are shown in Table 12.20.

Table 12.20 Critical Speed of CJ3000 Original Scheme with Different Rotor Dominating

rad/s	1st	2nd	3rd	4th	5th	6th	7th	8th	9th
HP Dominating	148.707	182.06	267.096	330.398	376.524	590.928	799.439	1001.166	1468.243
IP Dominating	155.461	185.357	303.413	373.2	486.97	655.757	1001.273	1478.77	1542.449
LP Dominating	169.047	192.152	321.064	406.632	621.368	905.541	1001.85	1479.871	3451.892

The values of many critical speeds are distributed in the range of working speed and are scattered. So the original scheme can not well reflect the superiority of the vibration characteristics and needs to be modified.

The following points are considered:

1. The connection span of the inner casing and the outer casing is too short.

2. Low pressure turbine, mixing chamber and tail nozzle are of high quality and need a rear bearing frame to carry out restraint and transmission.

Therefore, the low-pressure turbine rear bearing frame is added to the design. As a result, there are changes including the cancellation of the diffuser bearing frame, the setting of the high pressure turbine - middle pressure turbine inter-stage bearing frame (the axial distance of them meets the demand for the gentle transition of the gas path) and the cancellation of a rigid coupling of the core machine casing and bypass casing(using the force transmission line of a large by-pass ratio turbofan engine).

In the RB199 engine (Figure 12.8), the core machine casing and the by-pass casing are connected at internal and high-pressure mediator casing, and the axial force transmission line of the thrust bearing is shorter. Therefore, whether the rigid coupling in the same location is added is the first problem to be considered after the adjustment of the scheme. Using the parameters of the transfer matrix at the location in the original scheme, the critical speed calculation results are as follows: when the total mass of CJ3000 is basically unchanged, the calculation results are as follows:

Table 12.21 CJ3000 Scheme No. 2 with Critical Speed of Same Rotation Direction

rad/s	Avoidance Value	MS$\geqslant$0.2 ?	Critical Speed with MS < 0.2	
HP Dominating	914.83~1507.96	No	1342.812(8th)	1470.801(9th)
IP Dominating	591.31~980.18	No	656.5(6th)	—
LP Dominating	294.32~502.65	No	318.547(3rd)	417.786(4th)

Scheme two, after adopting three rigid coupling points, although it still does not reach 20% safety margin, it has the potential of optimization.

On this basis, the intermediate thrust bearing is tried to be placed in the rear fan bearing frame (such as RB211), and the results have not been found to be helpful in the calculation of the critical speed. Therefore, the overall structure scheme of CJ3000 is determined.
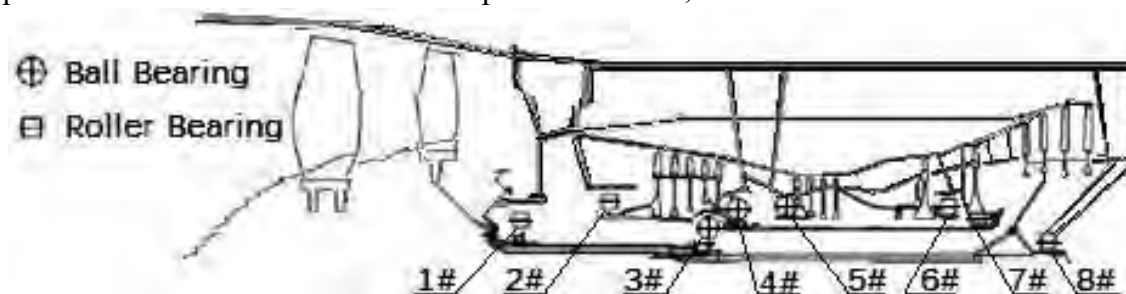
Figure 12.13 CJ3000 Engine Structure Diagram

12.4.6 Support Stiffness - Critical Speed Relation

The stiffness of each support has an important influence on the characteristics of critical speed. Changing the stiffness of the support

is an effective way to adjust the critical speed. Before attempting to optimize the supporting stiffness combination of CJ3000, the influence of the eleven stiffness values on the critical speed of the system will be evaluated.

Because the number of supports and critical speeds should be considered more, and the process is more complicated, the results of the program adjustment are listed directly in the report:

1. Improving stiffness of rigid coupling points has a very high effect on the optimization of critical speed of higher order.

2. The adjustment of the critical speed is a project which considers the engine structure comprehensively. The working form of the three rotor and the wider range of working speed determined by the four working points are more difficult for the optimization of the critical speed. Different critical speed schemes will be compared with the nearest boundary of the working speed range, and the safety margin (rather than 20%) will be recalculated.

12.4.7 Vibration Analysis Tool

PDVCCA can give the vibration modes of CJ3000 when the critical speeds and natural frequencies are given, which can be used to understand the vibration of CJ3000 directly after adjusting the overall structure scheme, so as to help further understand the vibration characteristics of the critical speed.

Generally speaking, the following principles or engineering experience should be followed:

1, the vibration at rotor speed is generally rigid body vibration (translational or overall pitching) or first order bending vibration (to ensure the service life of the rotor).

2. Casing generally does not vibrate at lower frequencies.

The mode of vibration given by PDVCCA is as follows:

(a) The Vibration Pattern

(b) Legend of The Vibration Pattern
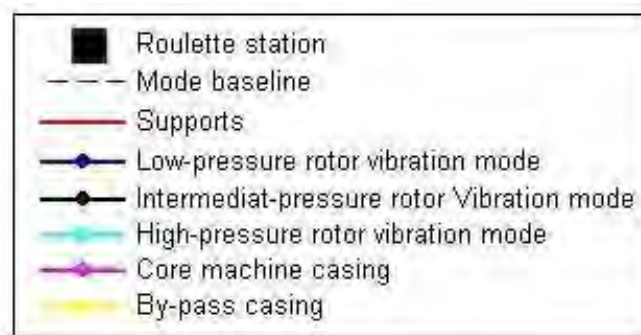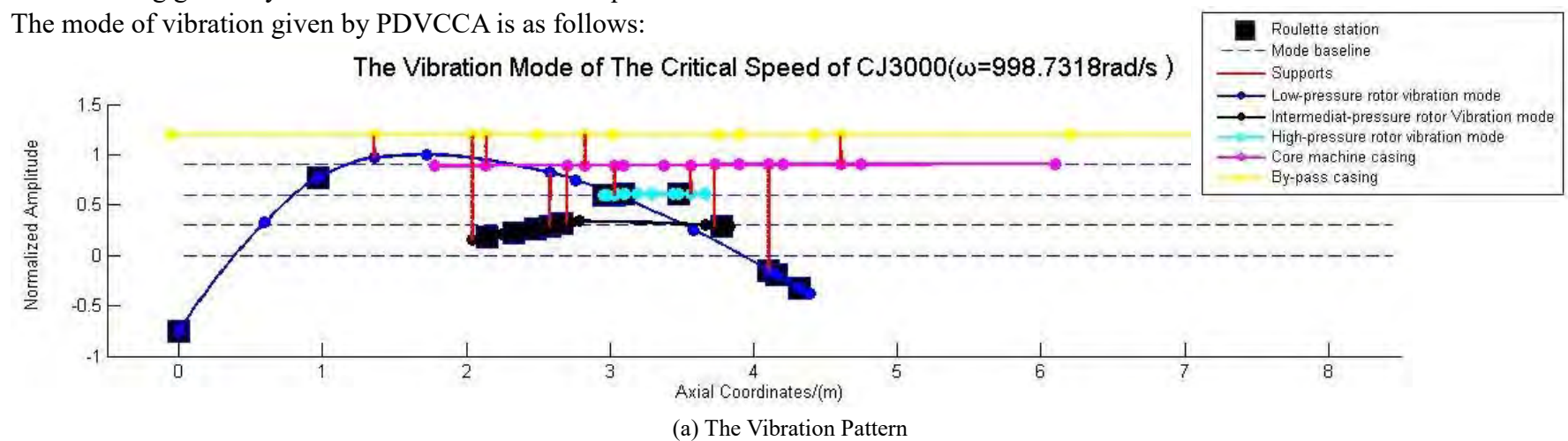
Figure 12.14 The Vibration Pattern Given by PDVCCA

The Y axis coordinate is the normalized amplitude, and the maximum amplitude of CJ3000 is 1. The X axis coordinates are the axial length, using the international unit m. The vibration modes of the five sub structures from inside to outside (the low-pressure rotor to the outer culvert casing) are raised by 0.3 amplitude and the baseline is displayed so as to distinguish them clearly. The PDVCCA also shows the wheel and the position of the support.

12.4.8 Critical Speed Results

After the combination of stiffness, the critical speed of CJ3000 is calculated as follows:

Table 12.22 Critical Rotational Speed of CJ3000 Three Rotor at The Same Direction

rad/s	Shaft Angular Frequency	Critical Speed	MS	Critical Speed	MS
HP Dominating	1143.54~1256.64	821.82 (7th)	0.281	1649.15 (8th)	0.312
IP Dominating	739.14~816.81	631.85 (6th)	0.145	1545.48 (7th)	0.892
LP Dominating	367.9~418.88	253.45(3rd)	0.311	494.41 (4th)	0.18

Table 12.23 Critical Speed of CJ3000 with High Pressure Rotor Reverse Rotation

rad/s	Shaft Angular Frequency	Critical Speed	MS	Critical Speed	MS
HP Dominating	1143.54~1256.64	649.63 (8th)	0.432	1646.69 (9th)	0.31
IP Dominating	739.14~816.81	631.85 (7th)	0.145	1545.48 (8th)	0.892
LP Dominating	367.9~418.88	253.49(3rd)	0.311	494.50(4th)	0.181

The design of the working state of the high-pressure rotor reversal has no obvious effect on the MS of the stable work, but it will make the engine a new critical speed. And attention needs to be paid in the process of reaching the cruise speed from start. With the determination of critical speed, the vibration characteristic evaluation proves that the structural scheme adopted can guarantee the reliability of CJ3000 in operation.

Since the cruising state takes a considerable amount of time in the flight envelope of the CJ3000, the natural frequency of the CJ3000 in the operating state is a concern for users of the CJ3000. Its calculation result is as follows (the inherent frequency below 1900rad/s is shown):

Table 12.24 Natural Frequency of Cruising (rad/s)

Same Direction	-1782.92	-1651.19	-618.61	-595.63	-430.13	-326.18	-255.88	-219.48
	-158.74	-110.38	-47.41	24.73	197.82	232.47	272.28	481.47
	610.47	710.59	964.29	1407.52	1650.06	1699.62		
HP Reversal	-1782.92	-1652.19	-1407.52	-618.62	-595.54	-429.97	-326.10	-255.03
	-212.06	-110.48	-47.44	20.35	160.74	199.41	237.72	272.60
	481.58	610.50	710.60	964.29	1649.11	1699.57		

Other results and scenario information are given in Appendix C.

12.4.9 CJ 3000 Overall Airflow Path

After establishing the three-dimensional model of the CJ3000 engine, the airflow path in the whole engine is drawn out:
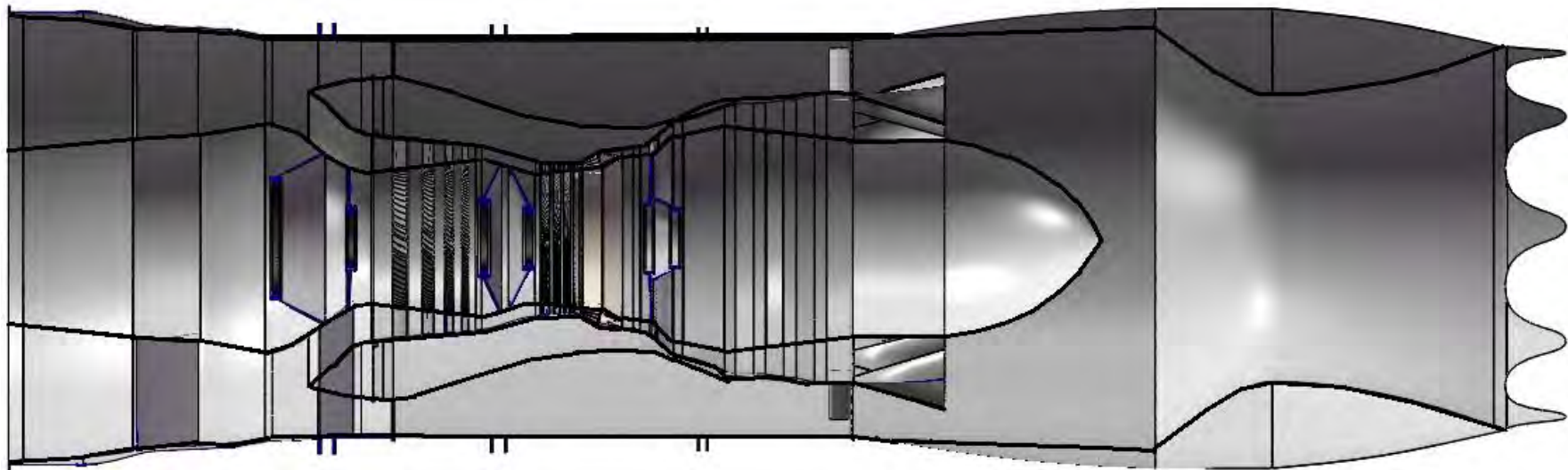
Figure 12.15 CJ3000 Overall Airflow Path

13 Identification and Selection of Engine Subsystems

13.1 Anti-Icing System

The anti-icing system prevents ice formation in the engine and the leading edge of the inlet. When the inlet parts of the engine freeze, the ice layer will reduce the intake area of the engine, which would reduce the intake air flow, thereby worsen the performance of the engine, and may even cause the compressor to surge. In addition, due to the vibration of the engine, the ice layer may be broken. The broken ice pieces may be sucked into the interior of the engine, which may cause the blades or even the entire engine to be damaged. Three measures would be taken to prevent ice formation and buildup: the hydrophobic coating, electrical system and hot air bleed system. The hydrophobic coating would be painted on the inlet cone, inlet casing and the support webs to prevent water vapor adhesion and condensation into ice. The electrical system, especially the heating pads bonded to the outer skin of the cowls on the inlet, would help to prevent ice buildup on the engine. The hot air taken from the HPC stages and distributed to engine components through the regulator valve would be led to the easily frozen position to aid in deicing.

13.2 Secondary Power System

The secondary power system of CJ 3000 consists of the auxiliary power system (APS) and the emergency power system (EPS) which work together controller as an integrated system – the Auxiliary/Emergency Power System (A/EPS) [36], which has been used by T-50. The APS provides with the main engine self-start capability, power to drive the main aircraft accessories (hydraulic pumps and electric generators), emergency electric power to the EPS via a shaft driven electric generator (BSG) and compressed air for the environmental control system (ECS). The EPS provides the necessary emergency electric and hydraulic power for the aircraft in the event of the loss of the main aircraft accessories. The A/EPS schematic diagram is shown in Fig 13.1 [36].
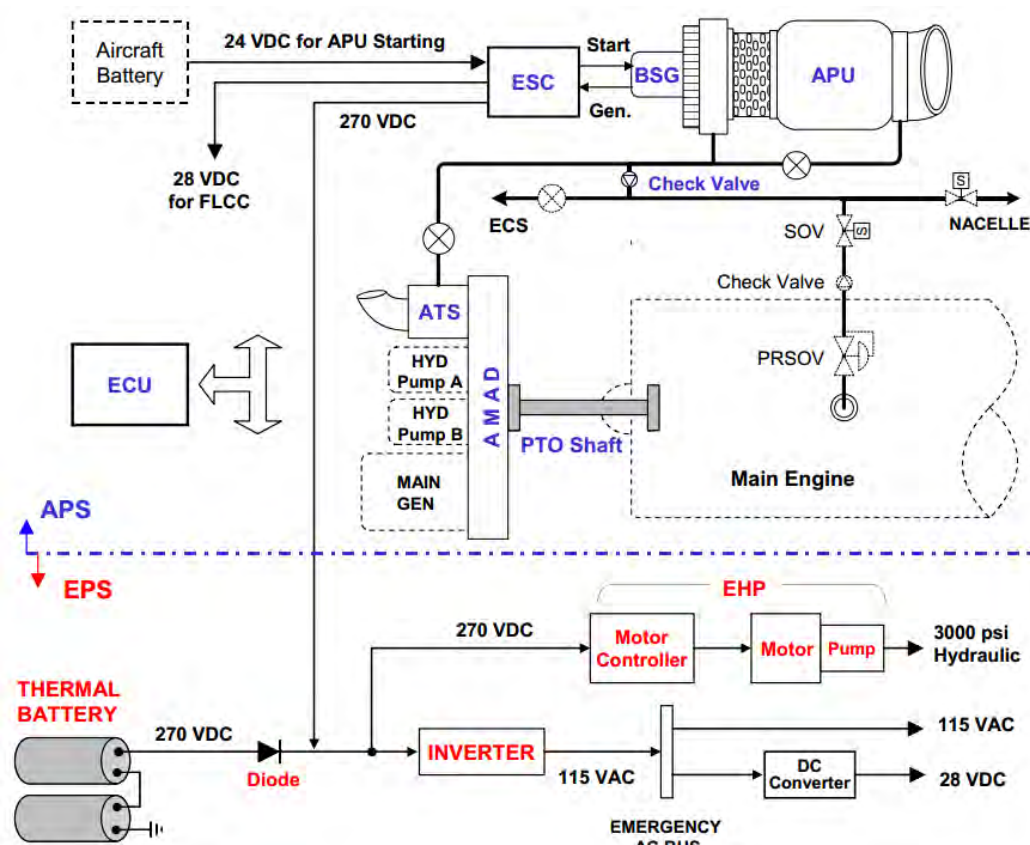
Figure 13.1 Schematic Diagram of A/EPS [36]

13.2.1 Auxiliary Power System

The CJ 3000 will be started by the APS that consists of an auxiliary power system (APS), an electronic starter controller (ESC), an air turbine starter (ATS), an airframe mounted accessory drive (AMAD), an electronic control unit (ECU), a brushless generator (BSG), flow control valve and airframe mounted accessory drive, as Fig 31 shows. The APU is a gas turbine engine that provides both pneumatic and shaft power. By delivering the compressed air from the APU via airframe ducting to the ATS, the APS converts the pneumatic power of APU to shaft power and delivers the shaft air to the AMAD. The AMAD then transfers the shaft power to the power take-off (PTO) shaft to start the main engine and to the AMAD-mounted accessories such as HYD pumps. After the main engine being started, the engine shaft power is delivered to the AMAD via the PTO shaft to provide primary flight control power for the aircraft. After starting the main engine, the APU provides pneumatic power to the environmental control system.

13.2.2 Emergency Power System

The EPS of CJ 3000 is a self-contained energy storage system that consists of thermal batteries, an electrically driven hydraulic pump (EHP) and an inverter. The EPS provides hydraulic and electrical emergency power simultaneously. The shaft power of APU drives the BSG to provide the electric energy for the EPS and store itself into thermal batteries. While needed, the DC electric power output of batteries could be transferred into AC for use by the inverter and/or drive the EHP to provide with hydraulic power.

13.3 Engine Control System

The performance and reliability of the aircraft engine control system is very important for the normal operation of the engine. In recent years, the mature full authority digital electronic engine control (FADEC) system can realize complex control law and modern control algorithm to meet the needs of modern aero-engine control. Its main uses include thrust control, control of fuel quantity, position of vent valve and angle control of adjustable stator blade, turbine clearance control, engine fuel and oil control, engine ignition and anti-thrust control, and safety protection, etc. Through the communication interface of the sensor and the operating table, the electronic controller accepts the state information from the engine and the control instruction information of the operating table. The controller calculates the required main fuel flow, the inlet of the high-pressure compressor inlet and the adjustable stator blade angle according to the scheduled engine adjustment plan, control law and control mode.

The main controller is the high performance digital computer, which is loaded with the aero engine control software. The control function is calculated according to the control instructions given by the pilot. The working condition input module sends signals from the sensor and signals from the control instruction input device to the computer. The main function of the execution instruction output module is to convert the control signal given by the main controller to the signal that the relevant actuator can accept. The oil supply unit mainly provides the required fuel to the engine main combustor and uses the fuel with certain pressure and flow as the working medium to drive the actuator. The electric hydraulic liquid conversion device converts the electrical signal from the digital controller to the flow or pressure of the hydraulic liquid as the working medium. It has fast response speed, smooth process, very good repeatability.

The electronic controller outputs analog signals to the main fuel actuator and the high-pressure compressor inlet adjustable stator blade angle actuator. After the conversion and amplification of the corresponding solenoid valve, these analog signals drive the metering valve movement and the high-pressure compressor inlet adjustable stator blade angle rotation to achieve the main fuel flow suitable for the engine state and the adjustable stator blade angle of the high-pressure compressor inlet. At the same time, the displacement sensor feedback the metering valve displacement signal and the adjustable stator blade angular displacement signal to the electronic controller, forming the respective closed loop control loop.
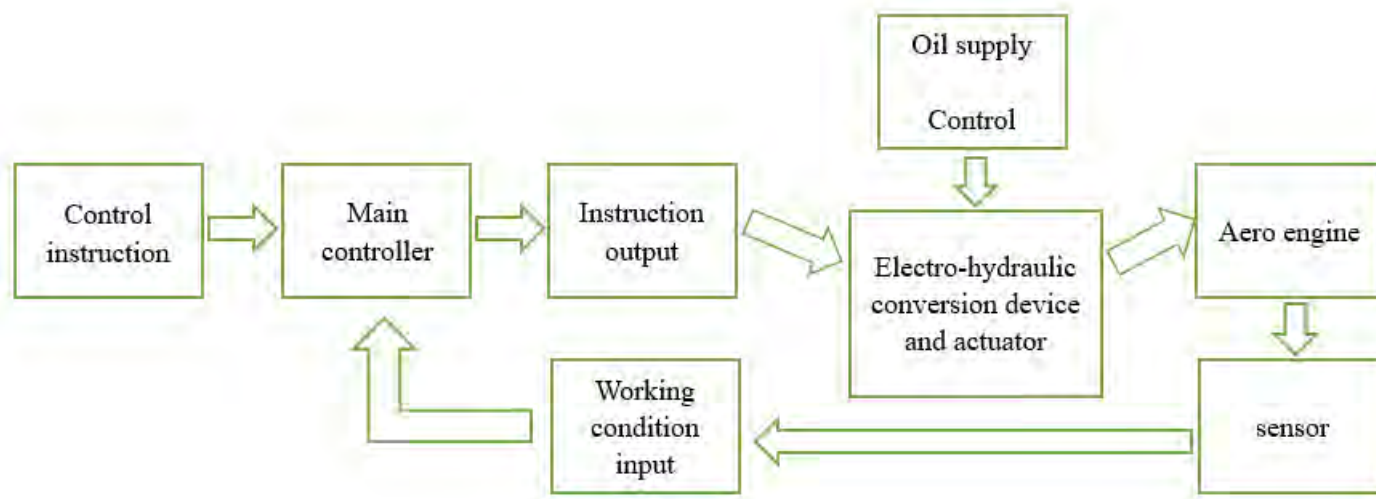
Figure 13.2 FADEC Block Diagram

13.4 Fuel System

The CJ 3000 uses signals provided by FADEC to electronically control the fuel system. The fuel is pumped from the aircraft fuel tank and then pressurized so that it can be injected into the combustor. In order to ensure the performance and service life of the engine, filters are used in fuel pumped and pressurized systems to ensure that the fuel quality meets the combustion requirements.

13.5 Lubricating Oil System

The main function of the lubricating oil is to lubricate the frictional contact interface between the bearing and gear and reduce the temperature. In order to achieve and maintain this function, a large number of pipelines, oil pumps and valves constitute the lubricating oil system. The CJ 3000 uses a double loop oil system with main and auxiliary circuits. Most of the oil does not pass through the slippery tank and enters the inlet of the turbocharged pump through the main oil road. The small part of the oil returns to the oil tank along the auxiliary circuit. The advantage of the dual loop design is that most of the lubricating oil only circulates in the lubricating oil path, which accelerates the preheating of the lubricating oil, reduces the starting resistance and accelerates the start-up speed. In addition, an oil suction pump can ensure that the booster pump has a certain residual pressure, and the system has good altitude characteristics.
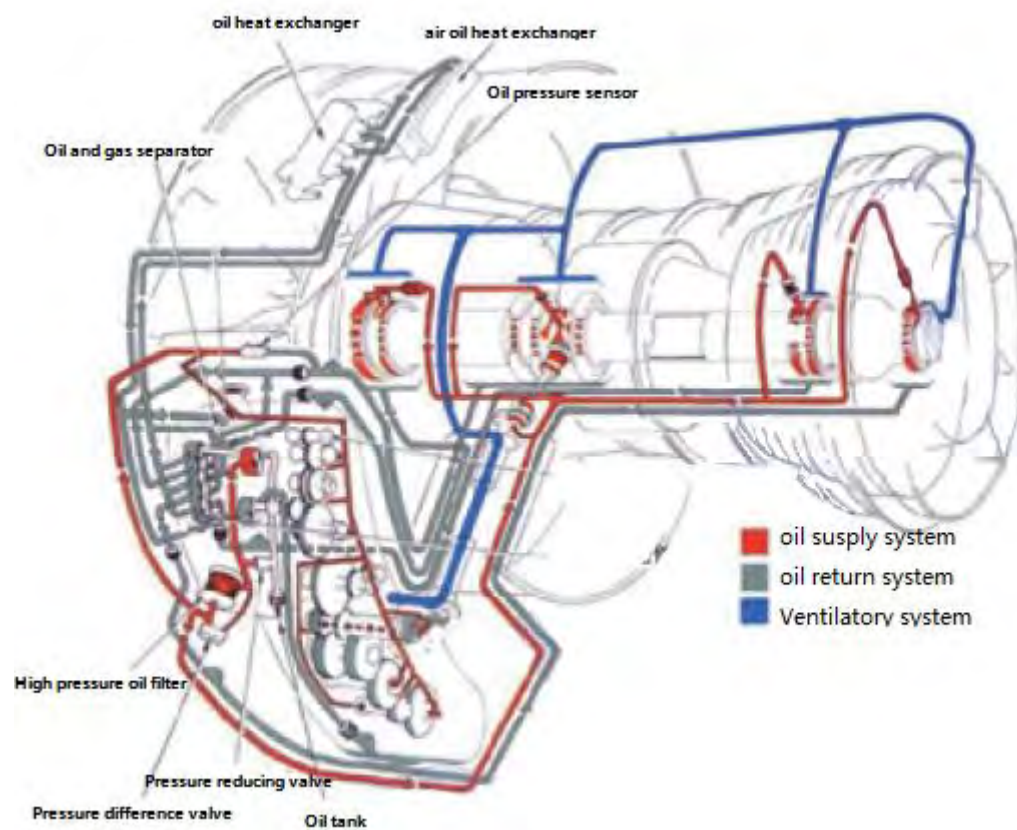
Figure 13.3 Lubricating Oil System

REFERENCES

[1] Anon, "Candidate Engines for a Next Generation Supersonic," AIAA Foundation Undergraduate Team Engine Design Competition, 1 August 2017.

[2] Harry R. Welge, "N+2 Supersonic Concept Development and Systems Integration," Boeing Research & Technology, Huntington Beach, California, August 2010

[3] Greg B. Bruening and Won S. Chang, "Cooled Cooling Air Systems For Turbine Thermal Management," Turbine Engine Division, 1999.

[4] Joachim Kurzke,, "GasTurb 13: A Design & Off-Design Performance Program for Gas Turbines", http://www.gasturb.de, 2017.

[5] Wood, K, Ceramic-matrix composites heat up. Retrieved from Composite World: http://www.compositesworld.com/articles/ceramic-matrix-composites-heat-up, 11 January 2013.

[6] Norris, G. GE Unveils CMC Production Ramp-Up Plan. Retrieved from Aviation Week: http://aviationweek.com/optimizing-engines-through-lifecycle/ge-unveils-cmc-production-ramp-plan, 27 October 2015.

[7] Anon, "GE Successfully Tests World's First Rotating Ceramic Matrix Composite Material for Next-Gen Combat Engine," GE Aviation, Cincinnati, Ohio, 2015.

[8] Michael C. Halbig, Martha H. Jaskowiak, James D. Kiser, and Dongming Zhu. Evaluation of Ceramic Matrix Composite Technology for Aircraft Turbine Engine Applications. NASA Glenn Research Center, Cleveland, OH 44135, 2013.

[9] Olcay Sari, Orçun Bulat, ITU BeEngine for a Next Generation Trainer. AIAA 2015 – 2016\ Undergraduate Engine Design Competition, May 2016.

[10] P. Walsh & P. Fletcher, "Gas Turbine Performance", Blackwell/ASME Press, 2nd Edition, 2004, pp. 225-226.

[11] Greitzer E. M. & Slater H. N., Design Methodologies for Aerodynamics, Structures, Weight, and Thermodynamic Cycles – Final Report. MIT - Aurora Flight Sciences and Pratt&Whitney Team, 31 March 2010.

[12] Mattingly, J.D. Hever, W.H., and Pratt, D.T., "Aircraft Engine Design," *J.S. Przemieniecki Ed.*, AIAA, Reston Virginia, 2002.

[13] Roskam, Jan. "Preliminary Sizing of Airplanes." *Airplane Design,* Vol. I, DARcorporation, Lawrence, KS 66049.

[14] Huang Yong, "Combustion and Combustor." BUAA Press, Beijing, September 2009.

[15] Allaire D L. A Physics Based Emissions Model for Aircraft Gas Turbine Combustors[D]. US: Department of Aeronautics and Astronautics, Massachusetts Institute of Technology, 2006.

[16] Antoine N E, Kroo I M. Framework for Aircraft Conceptual Design and Environmental Performance Studies[J]. AIAA Journal, 2005,43(10): 2100-2109.

[17] Tacina K M, Lee C M We C. NASA Glenn High Pressure Low NOx Emissions Research[R]. NASA TM-2008-214974, 2008.

[18] Lin Yuzhen, Quanhong Xu, Gaoen Lin. Gas turbine combustion chamber[D]. Beijing, China: National Defense Industry Press. 2008: 233-234.

[19] Cai J. Aerodynamics of Lean Direct Injection Combustor with Multi-Swirler Arrays[D]. Ohio: University of Cincinnati. 2006: 7.

[20] Cao Qinghua. LDI combustor theory and experimental research. Chinese Academy of Sciences University. 2013: 12-13.

[21] Mellor, A. M. Design of Modern Turbine Combustors. San Diego: Academic Press Inc. 1990:378.

[22] *Aero Engine Manual* Editorial Board. Aeroengine Design Handbook, Volume 9, Main Combustor. Beijing, China: Aviation Industry Press. 2000:123-125

[23] Kyle P. Thompson. TF-CLAWS: Candidate Low-Bypass, Mixed-Flow Turbofan Engine for a Next Generation Trainer. AIAA 2015 – 2016\ Undergraduate Engine Design Competition, May 2016.

[24] Haselbach, F, Parker, R. Hot End Technology for Advanced, Low Emission Large Civil Aircraft Engines. Brisbane, Australia: 28th International Congress of the Aeronautical Sciences, 23-28 September 2012.

[25] Mattingly, J. D., Elements of Gas Turbine Propulsion, McGraw-Hill, New York, 1996.

[26] Geng Yi. LDI Low Emission Combustion Technical Research. Nanjing University of Aeronautics and Astronautics. 2015.

[27] Farokhi, S, "Aircraft Propulsion." 2nd Edition, John Wiley & Sons Ltd, West Sussex, United Kingdom, 2014. Print.

[28] Tsui, Y.Y., and Wu, P.W., "Effects of Lobe Geometry on the Mixing Flow in Multilobe Mixers," Numerical Heat Transfer, Part A, 2001: 61-77.

[29] *Aero Engine Manual* Editorial Board. Aeroengine Design Handbook, Volume 11, Afterburner. Beijing, China: Aviation Industry Press. 2000: 55-73.

[30] Wu Jingyi. Study on Mixing Characteristics of Hybrid Diffuser. Beijing, China: BUAA. May, 2017.

[31] *Aero Engine Manual* Editorial Board. Aeroengine Design Handbook, Volume 7, Intake and Exhaust System. Beijing, China: Aviation Industry Press. 2000: 271-274.

[32] Guo Jinzhi. Investigation on Mixing Enhancement and Noise Reduction Mechanism of Chevron Nozzle. Shanghai, China: Shanghai Jiao Tong University. February 2013.

[33] Chen Guang, Hong Jie, Ma Yanhong. Aviation gas turbine engine structure. Beijing, China: BUAA Press. 2010: 389-400.

[34] Farokhi, S., "Noise in a Nutshell," AE 524, University of Kansas, Lawrence, KS 66045, 2016: 1-16,

[35] Anon, "Report on Jet Engine Noise Reduction," Naval Research Advisory Committee, Department of the U.S. Navy, 1400 Defense Pentagon, Arlington, VA 20301, April 2009

[36] Cha. J, Choi., D, Jung. K, Lee, S. and Hunter, B, "Advanced Emergency Power System Using Thermal Battery for Future Aircraft", 4th International Energy Conversion Engineering Conference and Exhibit (IECEC), 26-29 June 2006, San Diego, California, AIAA 2006-4161.

[37] Zinkle, S. J, and Snead L. L. Thermophysical and mechanical properties of SiC/SiC composites. United States: N. p., 1998. Web. doi:10.2172/330618.

[38] Bansal, Narottam P., and J. Lamon. 19. Integration and Joining of Ceramic Matrix Composites. Ceramic Matrix Composites: Materials, Modeling and Technology. John Wiley & Sons, Inc. 2014:549-567.

[39] Jiao Jian, and Chen Mingwei. "The preparation, properties and applications of a new generation of engine high temperature materials-ceramic matrix composites." Aeronautical Manufacturing Technology 451.7 (2014): 62-69.

[40] Bewlay, B. P., Weimer, M., Kelly, T., Suzuki, A. & Subramanian, P. R. The science, technology, and implementation of TiAl alloys in commercial aircraft engines. MRS Proc. 1516, 49–58 (2013).

[41] Chen G, Peng Y, Zheng G, et al. Polysynthetic twinned TiAl single crystals for high-temperature applications. Nature Materials, 2016, 15(8):876.

[42] Fan Z, Cantor B. The kinetics and mechanism of interfacial reaction in sigma fiber - reinforced Ti MMCs. Composites Part A, 1997, 28(2): 131.

[43] Shankar M. Titanium matrix composites - mechanical behavior. USA: Technomic Publishing Company, 1998 : 40.

[44] Li X, Yang Y, Zhang R, et al. Research on the coating of CVD SiC fiber. Materials China, 2010, 29 (3): 33 (in Chinese)

[45] Liang Chunhua. Application of fiber reinforced polymer matrix composite component on turbofan aeroengine. Aeronautical Manufacturing Technology, 2008(4): 32-37.

[46] Gao Yu, Li Yangyang, Wang Baichen,et al. Application of advanced resin matrix composites in aeroengine and its research progress. Aeronautical

Manufacturing Technology, 2016(21): 16-21.

[47] Chen Jun. Status Quo and Development Trend of Advanced Aircraft Engine Resin Matrix Composites Technology. Aeronautical Manufacturing Technology, 2016, 500(5):68-72.

[48] Bao Jianwen, Chen Xiangbao. Advanced in high temperature polyimide resin matrix composites for aeroengine. Journal of Aeronautical Materials. 2012, 32(6): 1-13.

[49] P2SI-900HT-Datasheet［R/OL］. https://www.proofresearchacd.com/products/prepregs/ P2SI-900HT-Datasheet.

[50] Gabb T P, Telesman J, Kantzos P T, et al. Characterization of the Temperature Capabilities of Advanced Disk Alloy ME3. 2002.

[51] Mattingly, J. and W. Heiser and D. Pratt, Aircraft Engine Design, 2nd ed., AIAA Education Series, Reston, VA, 2002

[52] Yan Li Tang,B. Analysis of Structural System Dynamic Characteristics ; Beijing University of Aeronautics and Astronautics Press, Beijing, China, 1989;pp.143.

[53] *Aero Engine Manual* Editorial Board. Aeroengine Design Handbook, Volume 19, Rotor Dynamics and Machine Vibration. Beijing, China: Aviation Industry Press. 2000: 82-118.

[54] Pang Hui. Dynamic Characteristics Analysis and Application of Multi-rotor System. Diss. Northwestern Polytechnical University, 2004;pp.44-46

[55] Hong Jie, Ma Yanhong, and Zhang Dayi, General structure design and dynamic analysis of aviation gas turbines. Beijing University of Aeronautics and Astronautics Press, 2014.

[56] Chen Guang. "Design features of the Trent 1000 engine." Aero Engines 35.4 (2009): 1-6.

[57] Chen Guang. "The Design Features of GEnx Engine for Boeing 787 Passenger Aircraft." Aero Engine 36.1 (2010): 1-6.

[58] Chen Guang. "Development and Design Features of Trent XWB Engine." Aero Engine 41.4(2015):1-7.

Appendix A – Simulation Validation of Engine by GasTurb 13

```
          W         T         P       WRstd
Station  lb/s       R       psia      lb/s          FN        =  15893.64 lb
  amb             389.97    1.492
   1    616.062   589.81    6.343                   TSFC      =    1.0092 lb/(lb*h)
   2    616.062   589.81    5.993    1610.938       WF Burner=     4.45534 lb/s
  13    404.386   763.68   13.640     528.682       s NOx     =    1.9177
  21    211.676   763.68   13.640     276.739       BPR       =    1.9104
  25    211.676   763.68   13.503     279.534       Core Eff  =    0.6081
   3    207.443  1767.12  220.627      25.505       Prop Eff  =    0.7906
  31    169.341  1767.12  220.627                   P3/P2     =   36.813
   4    173.796  3273.59  211.905      30.280
  41    190.730  3149.98  211.905      32.597       P16/P6    =    0.98886
  43    190.730  2208.28   36.897                   A63       = 2921.05  in²
  44    208.723  2172.41   36.897                   A163      = 4165.93  in²
  45    211.898  2166.69   36.528     174.242       A64       = 7086.98  in²
  49    211.898  1738.84   13.236                   XM63      =    0.27468
   5    214.015  1734.55   13.236     434.535       XM163     =    0.23579
   6    214.015  1734.55   13.104                   XM64      =    0.26000
  16    404.386   763.68   12.958                   P63/P6    =    0.99000
  64    618.401  1119.22   12.856                   P163/P16  =    0.99000
   8    618.401  1119.22   12.856    1038.419       A8        = 3204.95  in²
Bleed    2.117  1280.32   70.578                    CD8       =    0.95000
-----------------------------------------          Ang8      =   25.00  °
Efficiencies:  isentr  polytr   RNI    P/P          P8/Pamb   =    8.61895
  Outer LPC     0.8923  0.9039  0.350  2.276        WLkBy/W25=     0.00000
  Inner LPC     0.8923  0.9039  0.350  2.276        WCHN/W25  =    0.08000
  HP Compressor 0.8534  0.8958  0.579 16.339        WCHR/W25  =    0.08500
  Burner        0.9970                 0.960        Loading   =  100.00  %
  HP Turbine    0.9098  0.8913  1.755  5.743        WCLN/W25  =    0.01500
  LP Turbine    0.9122  0.9016  0.465  2.760        WCLR/W25  =    0.01000
  Mixer         0.5000                              WBHD/W21  =    0.00000
-----------------------------------------          far7      =    0.00726
HP Spool mech Eff 1.0000  Nom Spd  22800 rpm        WBLD/W25  =    0.01000
LP Spool mech Eff 1.0000  Nom Spd  14600 rpm        PWX       =    100.0 hp
-----------------------------------------          P16/P13   =    0.9500
P2/P1= 0.9448 P25/P21=0.9900 P45/P44= 0.9900        P6/P5     =    0.9900
Con-Di Nozzle:                                      A9/A8     =    1.72314
  A9*(Ps9-Pamb)      557.955                        CFGid     =    0.94844
-----------------------------------------
hum [%]    war0      FHV     Fuel
  0.0    0.00000   18552.4   Generic
```

Figure Appendix-A1 Baseline Engine Performance at Supersonic Cruise

```
          W         T         P       WRstd
Station  lb/s       R       psia      lb/s          FN        =  16471.16 lb
  amb             389.97    1.492                   TSFC      =    0.9132 lb/(lb*h)
   2    664.648   589.81    6.078    1713.680       WF Burner=     4.17818 lb/s
  13    487.408   782.82   14.831     593.356       s NOx     =    2.77485
  21    177.239   782.82   14.831     215.766       BPR       =    2.7500
  22    177.239   782.82   14.831     215.766       Core Eff  =    0.6640
  24    177.239  1266.84   71.766      56.723       Prop Eff  =    0.7984
  25    177.239  1266.84   71.048      57.295       P3/P2     =   45.003
   3    177.239  1866.31  273.535      18.063       P2/P1     =    0.95820
  31    169.264  1866.31  273.535                   P22/P21   =    1.00000
   4    173.442  3282.50  262.019      24.472       P25/P24   =    0.99000
  41    176.987  3256.33  262.019      24.873       P4/P3     =    0.95790
  42    176.987  2734.05  111.411                   P44/P43   =    1.00000
  43    180.531  2718.20  111.411                   P48/P47   =    1.00000
  44    180.531  2718.20  111.411                   P6/P5     =    1.00000
  45    181.418  2714.33  111.411      54.743       P16/P13   =    0.97000
  46    181.418  2318.86   52.593                   P5/P2     =    1.07644
  47    181.418  2318.86   52.593                   P8/P64    =    1.00000
  48    181.418  2318.86   52.593     107.186       P16/P6    =    1.07644
  49    181.418  1724.68   13.364                   A63       = 3470.93  in²
   5    181.418  1724.68   13.364     363.780       A163      = 3024.30  in²
  64    668.826  1055.37   13.742                   A64       = 6495.23  in²
   8    668.826  1055.37   13.742    1020.262       A8        = 3049.81  in²
Bleed    0.000  1866.31  273.534                    WBld/W2   =    0.00000
-----------------------------------------          Ang8      =   10.00  °
Efficiencies:  isentr  polytr   RNI    P/P          P8/Pamb   =    9.21304
  Outer LPC     0.8800  0.8939  0.355  2.440        PWX       =    0.00 hp
  Inner LPC     0.8800  0.8939  0.355  2.440        WlkLP/W25=     0.00000
  IP Compressor 0.8800  0.9023  0.618  4.839        WHDBl/W22=     0.00000
  HP Compressor 0.8800  0.8984  1.674  3.850        WCHN/W25  =    0.02000
  Burner        0.9970                 0.958        Loading   =  100.00  %
  HP Turbine    0.9200  0.9125  2.088  2.352        WCHR/W25  =    0.02000
  IP Turbine    0.9200  0.9133  1.096  2.118        WCIN/W25  =    0.00500
  LP Turbine    0.9200  0.9067  0.620  3.935        WCIR/W25  =    0.00000
-----------------------------------------          far7      =    0.00629
HP Spool mech Eff 0.9990  Nom Spd  40000 rpm        WCLR/W25  =    0.00000
IP Spool mech Eff 0.9990  Nom Spd  18000 rpm
LP Spool mech Eff 0.9990  Nom Spd  14600 rpm
-----------------------------------------
Con-Di Nozzle:                                      A9/A8     =    1.80000
  A9*(Ps9-Pamb)      433.311                        CFGid     =    0.95130
-----------------------------------------
hum [%]    war0      FHV     Fuel
  0.0    0.00000   18552.4   Generic
```

Figure Appendix-A2 CJ 3000 Uninstalled Performance at Supersonic Cruise

Station	W lb/s	T R	P psia	WRstd lb/s
amb		389.97	1.492	
2	661.943	589.81	6.053	1713.680
13	485.425	782.82	14.770	593.356
21	176.518	782.82	14.770	215.766
22	176.518	782.82	14.770	215.766
24	176.518	1266.84	71.474	56.723
25	176.518	1266.84	70.759	57.295
3	174.753	1866.31	272.422	17.882
31	166.810	1866.31	272.422	
4	170.927	3282.50	260.953	24.216
41	174.458	3256.06	260.953	24.616
42	174.458	2732.29	110.656	
43	177.988	2716.31	110.656	
44	177.988	2716.31	110.656	
45	178.870	2712.41	110.656	54.324
46	178.870	2312.81	51.775	
47	178.870	2312.81	51.775	
48	178.870	2312.81	51.775	107.212
49	178.870	1712.14	12.885	
5	178.870	1712.14	12.885	370.667
64	664.295	1049.63	13.443	
8	664.295	1049.62	13.443	1033.048
Bleed	1.765	1266.84	70.759	

FN	=	15993.69	lb
TSFC	=	0.9268	lb/(lb*h)
WF Burner=		4.11761	lb/s
s NOx	=	2.77032	
BPR	=	2.7500	
Core Eff =		0.6583	
Prop Eff =		0.8012	
P3/P2	=	45.003	
P2/P1	=	0.95430	
P22/P21	=	1.00000	
P25/P24	=	0.99000	
P4/P3	=	0.95790	
P44/P43	=	1.00000	
P48/P47	=	1.00000	
P6/P5	=	1.00000	
P16/P13	=	0.97000	
P5/P2	=	1.11196	
P8/P64	=	1.00000	
P16/P6	=	1.11196	
A63	=	3858.52	in²
A163	=	2717.49	in²
A64	=	6576.02	in²
A8	=	3087.71	in²
WBld/W2	=	0.00267	
Ang8	=	10.00	°
P8/Pamb	=	9.01275	
PWX	=	100.00	hp
WlkLP/W25=		0.00000	
WHDBl/W22=		0.00000	
WCHN/W25	=	0.02000	
Loading	=	100.00	%
WCHR/W25	=	0.02000	
WCIN/W25	=	0.00500	
WCIR/W25	=	0.00000	
far7	=	0.00624	
WCLR/W25	=	0.00000	

Efficiencies:	isentr	polytr	RNI	P/P
Outer LPC	0.8800	0.8939	0.354	2.440
Inner LPC	0.8800	0.8939	0.354	2.440
IP Compressor	0.8800	0.9023	0.615	4.839
HP Compressor	0.8800	0.8984	1.667	3.850
Burner	0.9970			0.958
HP Turbine	0.9200	0.9125	2.080	2.358
IP Turbine	0.9200	0.9133	1.089	2.137
LP Turbine	0.9200	0.9065	0.612	4.018

HP Spool mech Eff 0.9990	Nom Spd	12000	rpm
IP Spool mech Eff 0.9990	Nom Spd	7800	rpm
LP Spool mech Eff 0.9990	Nom Spd	4000	rpm

Con-Di Nozzle:
A9*(Ps9-Pamb)   251.706

A9/A8	=	1.80000
CFGid	=	0.95182

hum [%]	war0	FHV	Fuel
0.0	0.00000	18552.4	Generic

Figure Appendix-A3 CJ 3000 Installed Performance Without Drag of Inlet and Nozzle at Supersonic Cruise

Appendix B –Detailed Design Output of Turbomachinery Validation of Engine by GasTurb 13

We note that all value of parameters in Appendix B are in SI units.

Appendix B.1 Fan

Table Appendix-B1 Fan Design Output Values

Fan Measurements	Rotor 1		Stator 1		Rotor2		Stator2	
Static pressure	34.7255	52.3021	52.3027	57.1468	57.147	81.8888	81.8891	88.4315
Static Temperature	310.687	353.645	353.849	363.75	363.926	405.876	406.119	416.744
Total pressure	41.907	72.068	72.068	71.203	71.203	100.895	100.895	99.381
Total Temperature	327.67	389.604	389.515	389.513	389.686	447.931	447.933	448.158
Mach Numbers (absolute, mean radius)	0.526	0.715	0.715	0.598	0.598	0.721	0.720	0.613
Mach Numbers (relative, mean radius))	1.176	0.774	0.715	0.598	1.093	0.740	0.720	0.613
Blade angle(t)	-60.7507	-53.6608	29.7655	-1.02919	-52.7806	-41.9893	30.4962	-7.40118
Blade angle(m)	-54.3968	-38.6609	32.8393	-2.18019	-47.8146	-35.9894	30.9725	-7.40118
Blade angle(h)	-29.2173	10.3391	49.4189	-1.89419	-37.4436	-21.9894	33.9285	-7.40118
Radius(t)	1.20517	1.12023	1.11413	1.08878	1.08627	1.06663	1.06506	1.05188
Radius(m)	0.887362	0.887361	0.888158	0.887361	0.887336	0.887361	0.887374	0.887361
Radius(h)	0.349838	0.565595	0.579963	0.624	0.628294	0.661148	0.663717	0.684367
Hub to Tip Ratio	0.290281	0.504891	0.520551	0.573118	0.578397	0.619847	0.623176	0.65061
Blade axial gap	0	0.04	0.04	0.03	0.035	0.025	0.025	0.025
Tip speed	504	469	Not available		454	438	Not available	
Reaction(t)	0.957953		0.0420471		0.922818		0.0771823	
Reaction(m)	0.788354		0.211646		0.791777		0.208223	
Reaction(h)	0.552505		0.447495		0.631708		0.368292	
D factor(t)	0.411112		0.238785		0.404403		0.260574	
D factor(m)	0.40808		0.322257		0.390777		0.307549	
D factor(h)	0.335844		0.404278		0.369693		0.392827	
De Haller(t)	0.711		0.946		0.745		0.938	
De Haller(m)	0.701		0.847		0.715		0.859	
De Haller(h)	0.737		0.748		0.656		0.745	
Work coefficient	0.435937		Not available		0.386678		Not available	
Total Pressure ratio	1.720		0.988		1.471		0.985	
Blade Number	18		24		34		42	
Chord	0.571308		0.373106		0.385409		0.254582	
Aspect Ratio	1.1102		1.24506		1.19012		1.23684	
Adiabatic efficiency	0.893145							
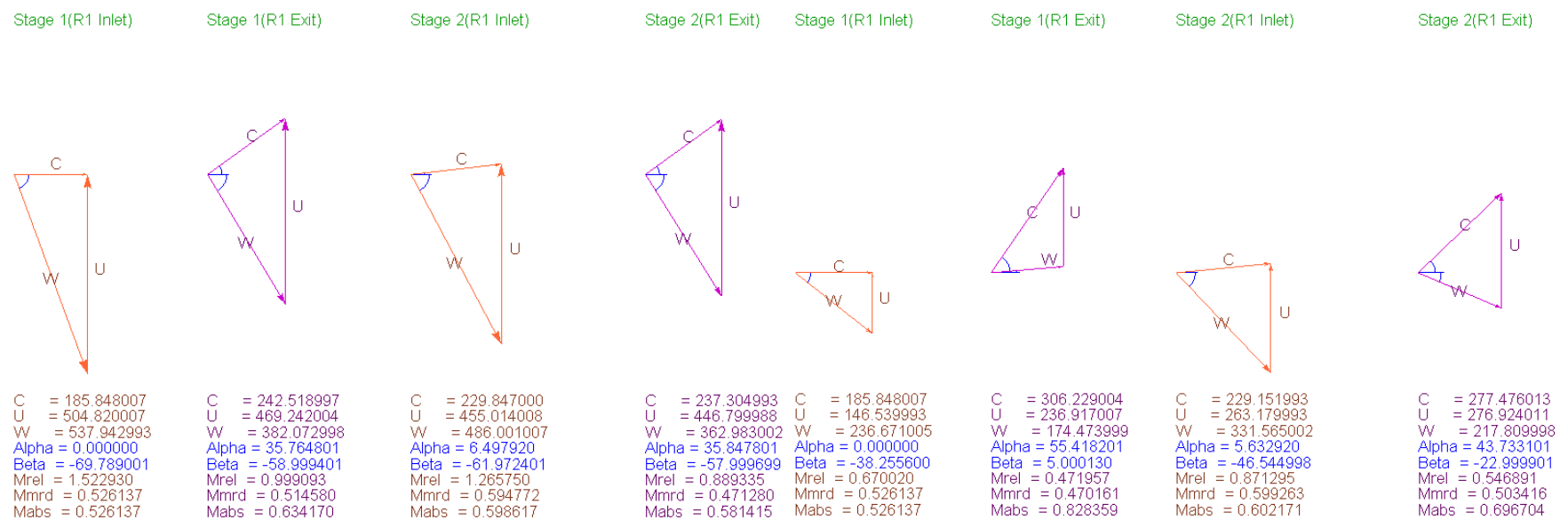
Figure Appendix-B1 Velocity Triangles of Tip Fan Blades   Figure Appendix-B1 Velocity Triangles of Hub Fan Blades

Stage 1(R1 Inlet)　　　Stage 1(R1 Exit)　　　Stage 2(R1 Inlet)　　　Stage 2(R1 Exit)

```
C     = 185.848007     C     = 269.480011     C     = 228.658005     C     = 255.028000
U     = 371.696991     U     = 371.696991     U     = 371.687012     U     = 371.696991
W     = 415.570007     W     = 291.796997     W     = 417.846985     W     = 299.742004
Alpha = 0.000000       Alpha = 38.838600      Alpha = 5.346920       Alpha = 36.719299
Beta  = -63.435101     Beta  = -43.999802     Beta  = -56.985699     Beta  = -46.999901
Mrel  = 1.176480       Mrel  = 0.774186       Mrel  = 1.093270       Mrel  = 0.742864
Mmrd  = 0.526137       Mmrd  = 0.556905       Mmrd  = 0.595669        Mmrd  = 0.506633
Mabs  = 0.526137       Mabs  = 0.714974       Mabs  = 0.598272        Mabs  = 0.632048
```

Figure Appendix-B3 Velocity Triangles of Mean Fan Blades

Appendix B.2 IPC

Table Appendix-B2 IPC Design Output Values

IPC Measurements	Rotor 1		Rotor2		Rotor3		Rotor4		Rotor5	
Static pressure	89.2043	123.04	131.957	176.234	187.719	244.253	258.632	329.212	346.952	433.369
Static Temperature	418.41	460.666	470.785	513.059	523.398	565.866	576.398	619.175	629.607	672.593
Total pressure	102.254	151.251	150.223	212.218	210.758	290.402	288.294	384.514	381.846	499.871
Total Temperature	434.9	488.391	488.386	540.77	540.836	594.282	594.391	647.002	646.922	700.335
Mach Numbers (absolute, mean radius)	0.446	0.549	0.433	0.523	0.410	0.505	0.397	0.476	0.372	0.457
Mach Numbers (relative, mean radius))	1.032	0.709	0.929	0.613	0.848	0.534	0.836	0.548	0.803	0.529
Blade angle(t)	-58.97	-55.40	-55.39	-54.99	-53.11	-54.28	-52.14	-53.37	-54.49	-52.22
Blade angle(m)	-55.18	-48.33	-52.96	-49.13	-52.15	-49.41	-52.53	-49.30	-54.16	-48.78
Blade angle(h)	-48.32	-33.62	-48.07	-38.97	-50.87	-41.96	-53.36	-43.58	-53.63	-44.25
Radius(t)	0.559	0.541	0.538	0.531	0.525	0.523	0.512	0.511	0.505	0.503
Radius(m)	0.467	0.467	0.467	0.467	0.467	0.467	0.467	0.467	0.467	0.467
Radius(h)	0.351	0.378	0.383	0.392	0.400	0.402	0.416	0.418	0.425	0.428
Hub to Tip Ratio	0.629	0.700	0.712	0.738	0.764	0.767	0.813	0.819	0.843	0.851
Blade axial gap	0.02	0.01	0.009	0.009	0.008	0.008	0.006	0.007	0.005	0.006
Inlet Tip speed	456.627		439.591		428.794		418.645		412.454	
Reaction(t)	0.862		0.86		0.880		0.852		0.843	
Reaction(m)	0.794		0.795		0.796		0.798		0.799	
Reaction(h)	0.712		0.708		0.702		0.73		0.752	
D factor(t)	0.363		0.386		0.414		0.389		0.416	
D factor(m)	0.383		0.419		0.458		0.430		0.443	
D factor(h)	0.383		0.466		0.532		0.524		0.479	
De Haller(t)	0.747		0.715		0.687		0.715		0.705	
De Haller(m)	0.721		0.678		0.649		0.681		0.682	
De Haller(h)	0.676		0.625		0.575		0.603		0.627	
Work coefficient	0.372		0.367		0.373		0.367		0.373	
Total Pressure ratio	1.479		1.412		1.37		1.334		1.309	
Blade Number	34		44		56		68		74	
Chord	0.138396		0.10689		0.0844854		0.068287		0.0562123	
Aspect Ratio	1.172		1.302		1.440		1.354		1.332	
Adiabatic efficiency	0.924									

```
C     = 183.130997   C     = 229.022003   C     = 195.029007   C     = 235.757996   C     = 202.949997   C     = 242.682007   C     = 214.455002   C     = 236.557007   C     = 197.759003   C     = 236.940002
U     = 456.627014   U     = 441.972992   U     = 439.591003   U     = 434.102997   U     = 428.794006   U     = 427.963013   U     = 418.368011   U     = 417.346008   U     = 412.393005   U     = 410.829987
W     = 491.980988   W     = 366.576996   W     = 455.425995   W     = 328.170013   W     = 431.160004   W     = 299.101990   W     = 439.261993   W     = 314.494995   W     = 431.829010   W     = 304.221985
Alpha = 0.000000     Alpha = 34.070999    Alpha = 8.000090     Alpha = 41.763100    Alpha = 13.000500    Alpha = 47.271599    Alpha = 9.000120     Alpha = 41.652699    Alpha = 8.000070     Alpha = 42.837898
Beta = -68.146599    Beta = -58.834202    Beta = -64.908401    Beta = -57.597801    Beta = -62.700500    Beta = -56.596298    Beta = -61.170502    Beta = -55.804501    Beta = -63.031601    Beta = -55.172600
Mrel = 1.200190      Mrel = 0.848400      Mrel = 1.046090      Mrel = 0.719070      Mrel = 0.938358      Mrel = 0.623633      Mrel = 0.910895      Mrel = 0.627801      Mrel = 0.856365      Mrel = 0.582711
Mmrd = 0.446751      Mmrd = 0.439061      Mmrd = 0.443611      Mmrd = 0.385321      Mmrd = 0.430371      Mmrd = 0.343332      Mmrd = 0.439238      Mmrd = 0.352836      Mmrd = 0.388361      Mmrd = 0.332790
Mabs = 0.446751      Mabs = 0.530047      Mabs = 0.447971      Mabs = 0.516582      Mabs = 0.441692      Mabs = 0.505998      Mabs = 0.444713      Mabs = 0.472219      Mabs = 0.392178      Mabs = 0.453838
```

Figure Appendix-B4 Velocity Triangles of Tip IPC Blades

```
C     = 183.130997   C     = 236.354004   C     = 188.233994   C     = 237.238998   C     = 188.177002   C     = 240.528000   C     = 191.425003   C     = 237.613998   C     = 186.942993   C     = 237.490005
U     = 381.523010   U     = 381.522003   U     = 381.518005   U     = 381.522003   U     = 381.523987   U     = 381.522003   U     = 381.532013   U     = 381.522003   U     = 381.523987   U     = 381.522003
W     = 423.197998   W     = 305.023010   W     = 404.330994   W     = 254.610992   W     = 388.737000   W     = 402.343994   W     = 274.498993   W     = 403.885986   W     = 275.700012
Alpha = 0.000000     Alpha = 36.939201    Alpha = 7.000090     Alpha = 43.394100    Alpha = 12.000500    Alpha = 49.034100    Alpha = 8.000120     Alpha = 44.317699    Alpha = 7.000070     Alpha = 44.029701
Beta = -64.358902    Beta = -51.732399    Beta = -62.479000    Beta = -51.732498    Beta = -61.738701    Beta = -51.731602    Beta = -61.891499    Beta = -51.732399    Beta = -62.650902    Beta = -51.732399
Mrel = 1.032400      Mrel = 0.709114      Mrel = 0.929901      Mrel = 0.613201      Mrel = 0.847958      Mrel = 0.534157      Mrel = 0.836737      Mrel = 0.550875      Mrel = 0.803688      Mrel = 0.530832
Mmrd = 0.446751      Mmrd = 0.439179      Mmrd = 0.429684      Mmrd = 0.379776      Mmrd = 0.401502      Mmrd = 0.330828      Mmrd = 0.394222      Mmrd = 0.341176      Mmrd = 0.369222      Mmrd = 0.328763
Mabs = 0.446751      Mabs = 0.549473      Mabs = 0.432911      Mabs = 0.522643      Mabs = 0.410473      Mabs = 0.504611      Mabs = 0.398097      Mabs = 0.476852      Mabs = 0.371995      Mabs = 0.457263
```

Figure Appendix-B5 Velocity Triangles of Mean IPC Blades

```
C     = 183.130997   C     = 250.832993   C     = 187.227997   C     = 239.897003   C     = 170.309998   C     = 237.067993   C     = 161.272995   C     = 239.925003   C     = 175.701004   C     = 238.020004
U     = 287.420990   U     = 309.480988   U     = 312.843994   U     = 320.427002   U     = 327.502014   U     = 328.582001   U     = 340.738007   U     = 341.966003   U     = 347.927002   U     = 349.766998
W     = 340.804993   W     = 230.186996   W     = 347.390991   W     = 222.516998   W     = 339.082001   W     = 199.966003   W     = 350.751007   W     = 211.903000   W     = 373.020996   W     = 243.326996
Alpha = 0.000000     Alpha = 42.911900    Alpha = 6.000090     Alpha = 46.064098    Alpha = 11.000500    Alpha = 52.853199    Alpha = 10.000100    Alpha = 52.167801    Alpha = 6.000070     Alpha = 46.005100
Beta = -57.496601    Beta = -37.051601    Beta = -57.588001    Beta = -41.578602    Beta = -60.459599    Beta = -44.283199    Beta = -63.076000    Beta = -46.015900    Beta = -62.066700    Beta = -47.199699
Mrel = 0.831398      Mrel = 0.537936      Mrel = 0.799906      Mrel = 0.493136      Mrel = 0.741272      Mrel = 0.422325      Mrel = 0.731585      Mrel = 0.427712      Mrel = 0.744961      Mrel = 0.471115
Mmrd = 0.446751      Mmrd = 0.429323      Mmrd = 0.428752      Mmrd = 0.368888      Mmrd = 0.365475      Mmrd = 0.302341      Mmrd = 0.331267      Mmrd = 0.297028      Mmrd = 0.346972      Mmrd = 0.320097
Mabs = 0.446751      Mabs = 0.586185      Mabs = 0.431114      Mabs = 0.531652      Mabs = 0.372317      Mabs = 0.500682      Mabs = 0.336377      Mabs = 0.484272      Mabs = 0.350894      Mabs = 0.460840
```

Figure Appendix-B6 Velocity Triangles of Hub IPC Blades

Appendix B.3 HPC

Table Appendix-B3 HPC Design Output Values

HPC Measurements	Rotor 1		Rotor2		Rotor3		Rotor4		Exit
Static pressure	442.497	616.282	659.857	888.306	944.797	1237.25	1308.69	1674.89	1763.5
Static Temperature	683.828	754.835	770.844	842.209	858.644	930.373	947.314	1020.15	1037
Total pressure	489.859	729.058	724.835	1040.22	1033.5	1441.28	1430.66	1905.68	1893.81
Total Temperature	703.8	791.616	791.616	880.706	880.738	971.461	971.518	1058.13	1058.14
Mach Numbers (absolute, mean radius)	0.384	0.496	0.3691	0.481	0.361	0.473	0.359	0.434	Absolute Mach number at exit =0.321
Mach Numbers (relative, mean radius))	1.035	0.703	0.935	0.609	0.852	0.529	0.857	0.566	
Blade angle(t)	-60.35	-57.42	-58.23	-57.47	-56.06	-54.67	-53.69	-49.47	
Blade angle(m)	-58.79	-54.54	-57.41	-55.16	-55.98	-53.79	-54.25	-48.92	
Blade angle(h)	-56.82	-50.76	-56.34	-52.30	-55.92	-53.57	-54.94	-45.14	
Radius(t)	0.434	0.427	0.426	0.423	0.421	0.420	0.416	0.415	0.414
Radius(m)	0.401	0.401	0.401	0.401	0.401	0.401	0.401	0.401	0.401
Radius(h)	0.364	0.372	0.373	0.376	0.379	0.379	0.385	0.385	0.387
Hub ratio	0.837	0.870	0.874	0.888	0.901	0.902	0.927	0.928	0.929
Blade axial gap	0.013	0.007	0.006	0.006	0.005	0.005	0.004	0.004	
Inlet Tip speed	564		535		529		524		
Reaction(t)	0.826		0.831		0.831		0.823		
Reaction(m)	0.799		0.801		0.803		0.805		
Reaction(h)	0.771		0.770		0.768		0.786		
D factor(t)	0.384		0.425		0.464		0.418		
D factor(m)	0.395		0.438		0.484		0.436		
D factor(h)	0.411		0.455		0.508		0.458		
De Haller(t)	0.728		0.728		0.721		0.717		
De Haller(m)	0.716		0.715		0.709		0.708		
De Haller(h)	0.697		0.695		0.696		0.695		
Work coefficient	0.352		0.357		0.363		0.347		
Total Pressure ratio	1.488		1.435		1.394		1.332		
Blade Number	84		104		126		150		
Chord	0.045		0.035		0.028		0.023		
Aspect Ratio	1.232		1.346		1.470		1.309		
Adiabatic efficiency	0.926								

Stage 1 (R1 Inlet)　　Stage 1 (R1 Exit)　　Stage 2 (R1 Inlet)　　Stage 2 (R1 Exit)　　Stage 3 (R1 Inlet)　　Stage 3 (R1 Exit)　　Stage 4 (R1 Inlet)　　Stage 4 (R1 Exit)

C   = 201.544006
U   = 546.331970
W   = 582.320984
Alpha = 0.000000
Beta = -69.750801
Mrel = 1.111200
Mmrd = 0.384592
Mabs = 0.384592

C   = 269.007996
U   = 537.343018
W   = 424.640991
Alpha = 38.706600
Beta = -60.372898
Mrel = 0.770099
Mmrd = 0.380700
Mabs = 0.487853

C   = 208.598999
U   = 535.518982
W   = 574.711975
Alpha = -0.000054
Beta = -68.717697
Mrel = 1.032630
Mmrd = 0.374806
Mabs = 0.374806

C   = 269.665009
U   = 530.315002
W   = 418.385010
Alpha = 38.720200
Beta = -59.809601
Mrel = 0.718253
Mmrd = 0.361191
Mabs = 0.462941

C   = 205.776993
U   = 529.020996
W   = 567.632996
Alpha = -0.000049
Beta = -68.745102
Mrel = 0.965970
Mmrd = 0.350182
Mabs = 0.350182

C   = 270.808014
U   = 525.146973
W   = 409.768005
Alpha = 39.575199
Beta = -59.376202
Mrel = 0.669175
Mmrd = 0.340877
Mabs = 0.442245

C   = 204.945007
U   = 524.112976
W   = 562.757996
Alpha = -0.000064
Beta = -68.642899
Mrel = 0.911526
Mmrd = 0.331959
Mabs = 0.331959

C   = 271.593994
U   = 521.247986
W   = 403.621002
Alpha = 40.147099
Beta = -59.045700
Mrel = 0.629634
Mmrd = 0.323855
Mabs = 0.423677

Figure Appendix-B7 Velocity Triangles of Tip HPC Blades

C = 201.544006	C = 273.204987	C = 204.483994	C = 273.256989	C = 202.897995	C = 273.587006	C = 202.423004	C = 273.833008
U = 503.859985	U = 503.859985	U = 503.850006	U = 503.859985	U = 503.855011	U = 503.859985	U = 503.856995	U = 503.859985
W = 542.672974	W = 388.440002	W = 543.763000	W = 388.049988	W = 543.172974	W = 385.675995	W = 542.997986	W = 383.984985
Alpha = 0.000000	Alpha = 40.180000	Alpha = -0.000054	Alpha = 40.260899	Alpha = -0.000049	Alpha = 40.753601	Alpha = -0.000064	Alpha = 41.103901
Beta = -68.198601	Beta = -57.495499	Beta = -67.910599	Beta = -57.495499	Beta = -68.065804	Beta = -57.495499	Beta = -68.112396	Beta = -57.495899
Mrel = 1.035540	Mrel = 0.705693	Mrel = 0.977473	Mrel = 0.667351	Mrel = 0.925119	Mrel = 0.630968	Mrel = 0.880501	Mrel = 0.600111
Mmrd = 0.384592	Mmrd = 0.379215	Mmrd = 0.367581	Mmrd = 0.358612	Mmrd = 0.345570	Mmrd = 0.339061	Mmrd = 0.328239	Mmrd = 0.322476
Mabs = 0.384592	Mabs = 0.496341	Mabs = 0.367581	Mabs = 0.469935	Mabs = 0.345570	Mabs = 0.447591	Mabs = 0.328239	Mabs = 0.427960

Figure Appendix-B8 Velocity Triangles of Mean HPC Blades

C = 201.544006	C = 278.398010	C = 200.914993	C = 277.351013	C = 200.244003	C = 276.665985	C = 200.011993	C = 276.259003
U = 457.460999	U = 467.985992	U = 470.053009	U = 475.934998	U = 477.364014	U = 481.631989	U = 482.752014	U = 485.848999
W = 499.890015	W = 348.941986	W = 511.191010	W = 355.721985	W = 517.661987	W = 360.266998	W = 522.546021	W = 363.454987
Alpha = 0.000000	Alpha = 42.118099	Alpha = -0.000054	Alpha = 42.072399	Alpha = -0.000049	Alpha = 42.114601	Alpha = -0.000064	Alpha = 42.186199
Beta = -66.223099	Beta = -53.714802	Beta = -66.856697	Beta = -54.636700	Beta = -67.242996	Beta = -55.273102	Beta = -67.495003	Beta = -55.722500
Mrel = 0.953906	Mrel = 0.635125	Mrel = 0.919340	Mrel = 0.612864	Mrel = 0.882393	Mrel = 0.590475	Mrel = 0.848268	Mrel = 0.569080
Mmrd = 0.384592	Mmrd = 0.375870	Mmrd = 0.361331	Mmrd = 0.354701	Mmrd = 0.341330	Mmrd = 0.336373	Mmrd = 0.324687	Mmrd = 0.320507
Mabs = 0.384592	Mabs = 0.506724	Mabs = 0.361331	Mabs = 0.477840	Mabs = 0.341330	Mabs = 0.453453	Mabs = 0.324687	Mabs = 0.432552

Figure Appendix-B9 Velocity Triangles of Hub HPC Blades

Appendix B.4 HPT

Table Appendix-B4 HPT Design Output Values

HPT Measurements	Stator 1		Rotor 1	
Static pressure	1694.62	1028.77	1028.77	652.188
Static Temperature	1776.6	1555.53	1555.53	1379.58
Total pressure	1806.56	1753.66	1753.66	765.334
Total Temperature	1809.07	1809.07	1809.07	1443.5
Mach Numbers (absolute, mean radius)	0.304	0.908	0.908	0.483
Mach Numbers (relative, mean radius))	0.304	0.908	0.458	0.940
Blade angle(t)	0	58.01	-0.15	-55.94
Blade angle(m)	0	57.13	4.84	-54.7
Blade angle(h)	0	56.17	9.33	-53.32
Radius(t)	0.485	0.485	0.486	0.491
Radius(m)	0.469	0.469	0.469	0.469
Radius(h)	0.453	0.452	0.451	0.445
Hub to Tip Ratio	0.934024	0.93237	0.927827	0.906305
Blade axial gap	0.008	0.008	0.008	0.008
Tip speed	Not available		611.362	
Reaction(t)	0.646		0.353	
Reaction(m)	0.673		0.326	
Reaction(h)	0.701		0.298	
Work Coefficient	0		1.0694	
Zweifel Coefficient(t)	0.826		0.793	
Zweifel Coefficient(m)	0.805		0.806	
Zweifel Coefficient(h)	0.782		0.821	
Total Pressure ratio	1.031		2.291	
Blade Number	145		145	
Blade Chord	0.0292		0.0295	
Aspect Ratio	1.126		1.56	
Adiabatic efficiency	0.9362			

Stage 1 (R1 Inlet)	Stage 1 (R1 Exit)	Stage 1 (R1 Inlet)	Stage 1 (R1 Exit)	Stage 1 (R1 Inlet)	Stage 1 (R1 Exit)

C   = 700.340027
U   = 611.362976
W   = 343.191010
Alpha = 60.657200
Beta = -0.145866
Mrel = 0.432493
Mmrd = 0.432492
Mabs = 0.882577

C   = 354.234985
U   = 617.960022
W   = 713.603027
Alpha = -0.245063
Beta = -60.237999
Mrel = 0.958765
Mmrd = 0.475930
Mabs = 0.475934

C   = 717.747986
U   = 589.713013
W   = 362.325989
Alpha = 59.801102
Beta = 4.848610
Mrel = 0.458385
Mmrd = 0.456745
Mabs = 0.908036

C   = 360.170013
U   = 589.721008
W   = 699.757996
Alpha = -1.641360
Beta = -59.036301
Mrel = 0.940115
Mmrd = 0.483685
Mabs = 0.483883

C   = 735.719971
U   = 567.237976
W   = 385.511993
Alpha = 58.864700
Beta = 9.330110
Mrel = 0.489745
Mmrd = 0.483266
Mabs = 0.934639

C   = 368.061005
U   = 560.059998
W   = 687.229980
Alpha = -3.218720
Beta = -57.674599
Mrel = 0.923203
Mmrd = 0.493662
Mabs = 0.494442

Figure Appendix-B10 Velocity Triangles of HPT Blades (Tip, Mean, Hub from left to right)

Appendix B.5 IPT

Table Appendix-B5 IPT Design Output Values

IPT Measurements	Stator 1		Rotor 1	
Static pressure	703.287	435.283	435.283	289.868
Static Temperature	1470.76	1293.79	1293.79	1164.62
Total pressure	768.153	747.729	747.729	362.497
Total Temperature	1507.96	1507.96	1507.96	1240.73
Mach Numbers (absolute, mean radius)	0.357	0.914	0.914	0.577
Mach Numbers (relative, mean radius))	0.357	0.914	0.535	0.944
Blade angle(t)	0	53.77	5.01	-50.96
Blade angle(m)	0	52.33	8.60	-48.81
Blade angle(h)	0	51.36	12.36	-47.81
Radius(t)	0.6045	0.614	0.617	0.626
Radius(m)	0.5763	0.585	0.589	0.597
Radius(h)	0.5479	0.555	0.557	0.567
Hub ratio	0.919	0.917	0.914	0.896
Blade axial gap	0.011	0.011	0.011	0.011
Tip speed			501.205	
Reaction(t)	0.665		0.335	
Reaction(m)	0.695		0.305	
Reaction(h)	0.726		0.273	
Zweifel Coefficient(t)	0.865		0.853	
Zweifel Coefficient(m)	0.834		0.858	
Zweifel Coefficient(h)	0.798		0.864	
Total Pressure ratio	1.028		2.062	
Blade Number	144		149	
Blade Chord	0.0367		0.0376	
Aspect Ratio	1.366		1.729	
Adiabatic efficiency		0.9252		
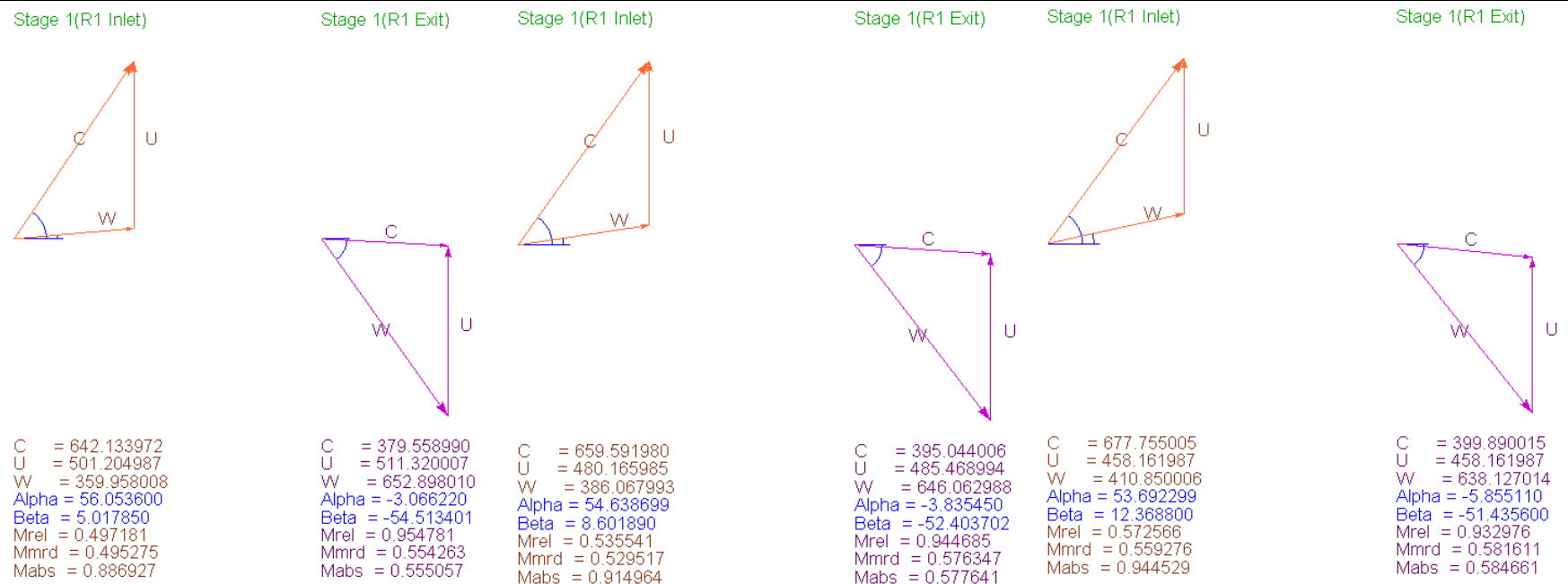
Figure Appendix-B11 Velocity Triangles of IPT Blades (Tip, Mean, Hub from left to right)

Appendix B.6 LPT

Table Appendix-B6 LPT Design Output Values

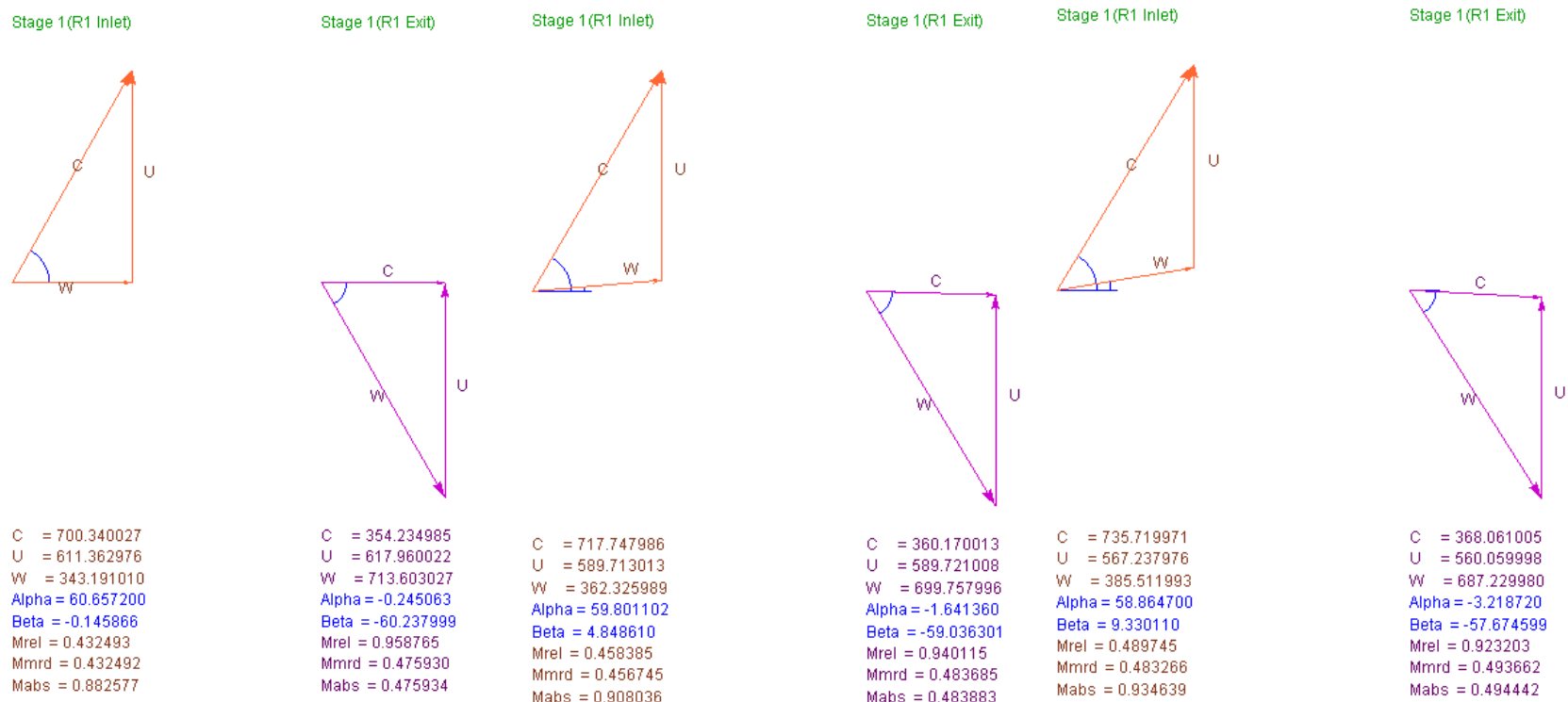| LPT Measurements	Rotor 1		Rotor 2		Rotor 3		Rotor 4	
Static pressure	285.383	245.255	205.326	174.449	143.627	120.449	97.0392	80.221
Static Temperature	1222.65	1184.5	1140.04	1101.43	1055.51	1016.36	968.433	929.068
Total pressure	358.255	269.945	266.42	194.345	191.78	135.93	134.153	92.0978
Total Temperature	1288.26	1211.11	1211.17	1129.67	1129.8	1045.98	1046.23	960.529
Mach Numbers (absolute, mean radius)	0.598	0.384	0.638	0.405	0.669	0.425	0.702	0.447
Mach Numbers (relative, mean radius))	0.361	0.591	0.388	0.622	0.408	0.652	0.429	0.686
Blade angle(t)	5.63	-49.21	5.35	-49.77	2.952	-50.50	-1.34	-51.55
Blade angle(m)	11.61	-47.05	13.60	-47.02	14.269	-46.94	14.74	-46.87
Blade angle(h)	16.11	-44.49	19.16	-43.55	20.92	-42.05	22.40	-39.59
Radius(t)	0.719	0.722	0.732	0.736	0.750	0.755	0.775	0.783
Radius(m)	0.670	0.670	0.670	0.670	0.670	0.670	0.670	0.670
Radius(h)	0.617	0.614	0.6020	0.597	0.579	0.572	0.544	0.533
Hub ratio	0.857	0.850	0.822	0.811	0.772	0.757	0.702	0.680
Blade axial gap	0.007	0.007	0.0075	0.0075	0.008	0.008	0.009	0.013
Tip speed	301.503		306.817		314.336		325.021	
Reaction(t)	0.397		0.402		0.420		0.446	
Reaction(m)	0.344		0.328		0.322		0.317	
Reaction(h)	0.286		0.247		0.213		0.169	
Zweifel Coefficient(t)	0.848		0.857		0.861		0.866	
Zweifel Coefficient(m)	0.848		0.867		0.877		0.886	
Zweifel Coefficient(h)	0.841		0.865		0.868		0.852	
Total Pressure ratio	1.327		1.371		1.411		1.456	
Blade Number	151		135		126		130	
Blade Chord	0.04336		0.04870		0.05208		0.0503	
Aspect Ratio	2.491		2.847		3.525		4.971	
Adiabatic efficiency	0.9268							

Stage 1(R1 Inlet)   Stage 1(R1 Exit)   Stage 2(R1 Inlet)   Stage 2(R1 Exit)   Stage 3(R1 Inlet)   Stage 3(R1 Exit)   Stage 4(R1 Inlet)   Stage 4(R1 Exit)

C   = 391.428009
U   = 301.576996
W   = 221.778000
Alpha = 55.675999
Beta = 5.612090
Mrel = 0.322596
Mmrd = 0.321050
Mabs = 0.569367

C   = 250.886993
U   = 302.544006
W   = 404.434998
Alpha = -3.432960
Beta = -51.740299
Mrel = 0.598686
Mmrd = 0.370723
Mabs = 0.371389

C   = 393.924988
U   = 307.112000
W   = 220.093002
Alpha = 56.195900
Beta = 5.270790
Mrel = 0.330647
Mmrd = 0.329249
Mabs = 0.591796

C   = 251.477005
U   = 308.371002
W   = 410.582001
Alpha = -3.787110
Beta = -52.327099
Mrel = 0.629218
Mmrd = 0.384548
Mabs = 0.385390

C   = 388.204010
U   = 314.760010
W   = 212.285004
Alpha = 56.894600
Beta = 2.815120
Mrel = 0.330316
Mmrd = 0.329917
Mabs = 0.604044

C   = 250.033005
U   = 316.648010
W   = 415.829987
Alpha = -3.668780
Beta = -53.126301
Mrel = 0.662142
Mmrd = 0.397321
Mabs = 0.398137

C   = 499.255005
U   = 227.632004
W   = 365.651001
Alpha = 47.423000
Beta = 22.512800
Mrel = 0.599564
Mmrd = 0.553873
Mabs = 0.818636

C   = 325.953003
U   = 223.507996
W   = 432.381989
Alpha = -12.184500
Beta = -42.534401
Mrel = 0.717018
Mmrd = 0.528350
Mabs = 0.540527

Figure Appendix-B12 Velocity Triangles of Tip LPT Blades

C = 410.221008	C = 259.856995	C = 423.532013	C = 264.906006	C = 428.238007	C = 267.518005	C = 431.683990	C = 269.649994
U = 280.839996	U = 280.839996	U = 280.842987	U = 280.839996	U = 280.846985	U = 280.839996	U = 280.854004	U = 280.839996
W = 247.755005	W = 399.572998	W = 257.782990	W = 406.576996	W = 261.398010	W = 410.153992	W = 264.065002	W = 413.052002
Alpha = 53.730999	Alpha = -5.213140	Alpha = 53.730999	Alpha = -6.273380	Alpha = 53.730999	Alpha = -6.799380	Alpha = 53.730999	Alpha = -7.218050
Beta = 11.619500	Beta = -49.635502	Beta = 13.603100	Beta = -49.635399	Beta = 14.267200	Beta = -49.635399	Beta = 14.740900	Beta = -49.635399
Mrel = 0.361204	Mrel = 0.591447	Mrel = 0.388483	Mrel = 0.622938	Mrel = 0.408508	Mrel = 0.652818	Mrel = 0.429686	Mrel = 0.686017
Mmrd = 0.353802	Mmrd = 0.383049	Mmrd = 0.377586	Mmrd = 0.403445	Mmrd = 0.395908	Mmrd = 0.422797	Mmrd = 0.415544	Mmrd = 0.444298
Mabs = 0.598065	Mabs = 0.384640	Mabs = 0.638270	Mabs = 0.405876	Mabs = 0.669243	Mabs = 0.425792	Mabs = 0.702435	Mabs = 0.447848

Figure Appendix-B13 Velocity Triangles of Mean LPT Blades

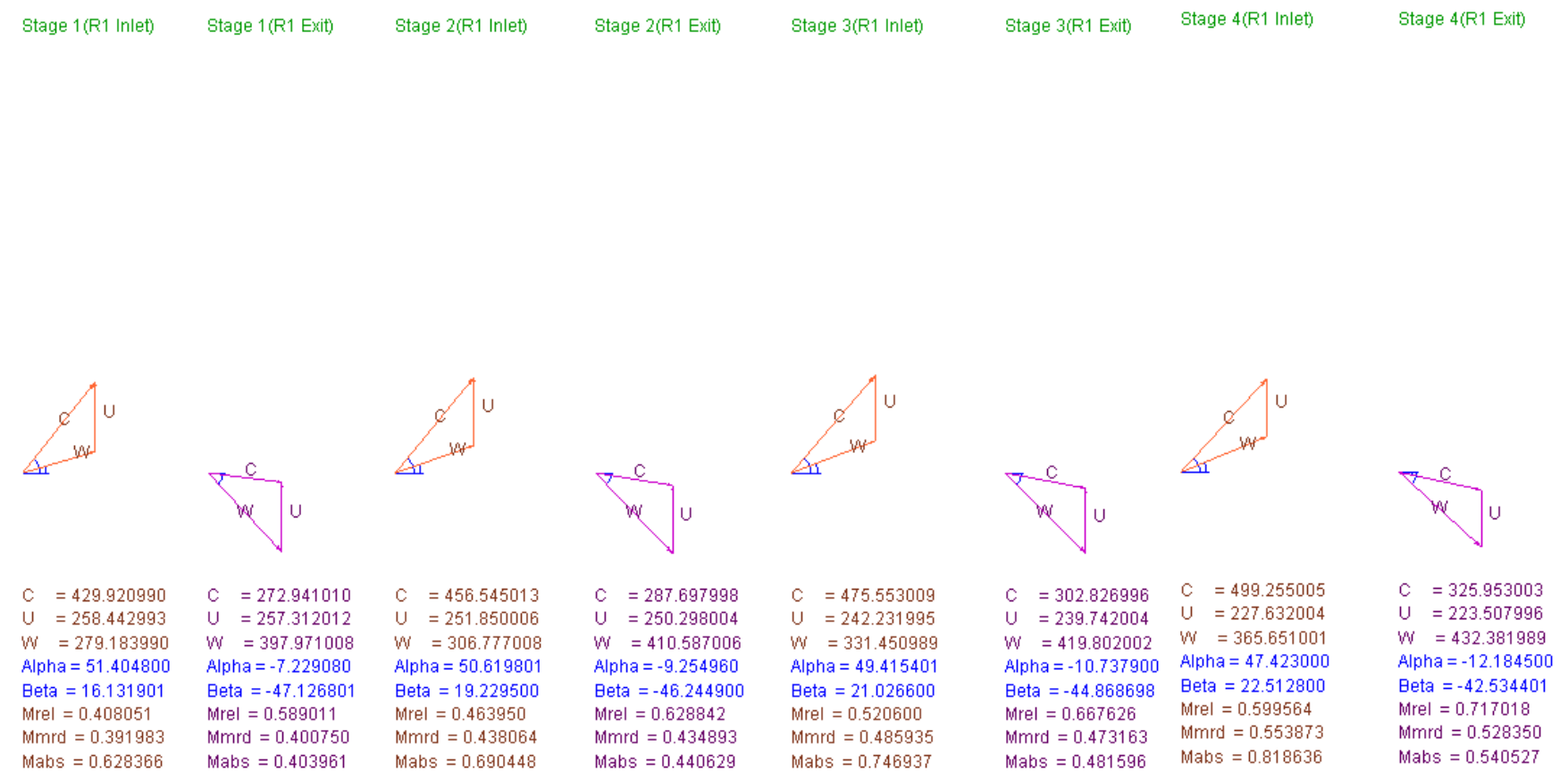| C = 429.920990	C = 272.941010	C = 456.545013	C = 287.697998	C = 475.553009	C = 302.826996	C = 499.255005	C = 325.953003
U = 258.442993	U = 257.312012	U = 251.850006	U = 250.298004	U = 242.231995	U = 239.742004	U = 227.632004	U = 223.507996
W = 279.183990	W = 397.971008	W = 306.777008	W = 410.587006	W = 331.450989	W = 419.802002	W = 365.651001	W = 432.381989
Alpha = 51.404800	Alpha = -7.229080	Alpha = 50.619801	Alpha = -9.254960	Alpha = 49.415401	Alpha = -10.737900	Alpha = 47.423000	Alpha = -12.184500
Beta = 16.131901	Beta = -47.126801	Beta = 19.229500	Beta = -46.244900	Beta = 21.026600	Beta = -44.868698	Beta = 22.512800	Beta = -42.534401
Mrel = 0.408051	Mrel = 0.589011	Mrel = 0.463950	Mrel = 0.628842	Mrel = 0.520600	Mrel = 0.667626	Mrel = 0.599564	Mrel = 0.717018
Mmrd = 0.391983	Mmrd = 0.400750	Mmrd = 0.438064	Mmrd = 0.434893	Mmrd = 0.485935	Mmrd = 0.473163	Mmrd = 0.553873	Mmrd = 0.528350
Mabs = 0.628366	Mabs = 0.403961	Mabs = 0.690448	Mabs = 0.440629	Mabs = 0.746937	Mabs = 0.481596	Mabs = 0.818636	Mabs = 0.540527

Figure Appendix-B14 Velocity Triangles of Hub LPT Blades
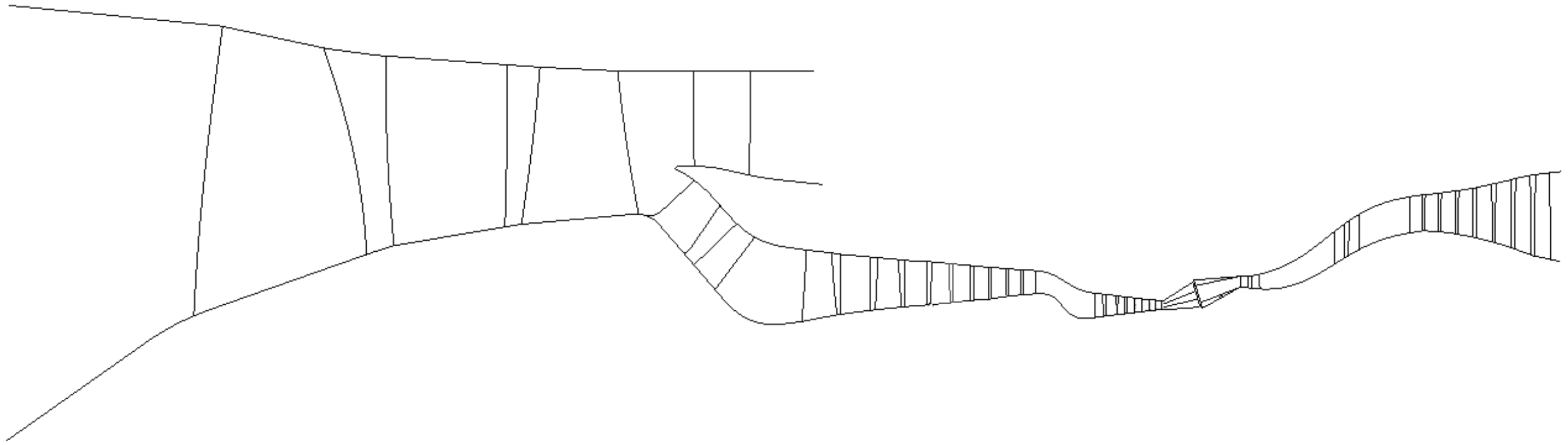
Appendix B.7 Turbomachinery Flow Path

Figure Appendix-B15 Turbomachinery Flow Path

Appendix B.8 Turbomachinery 3D Model

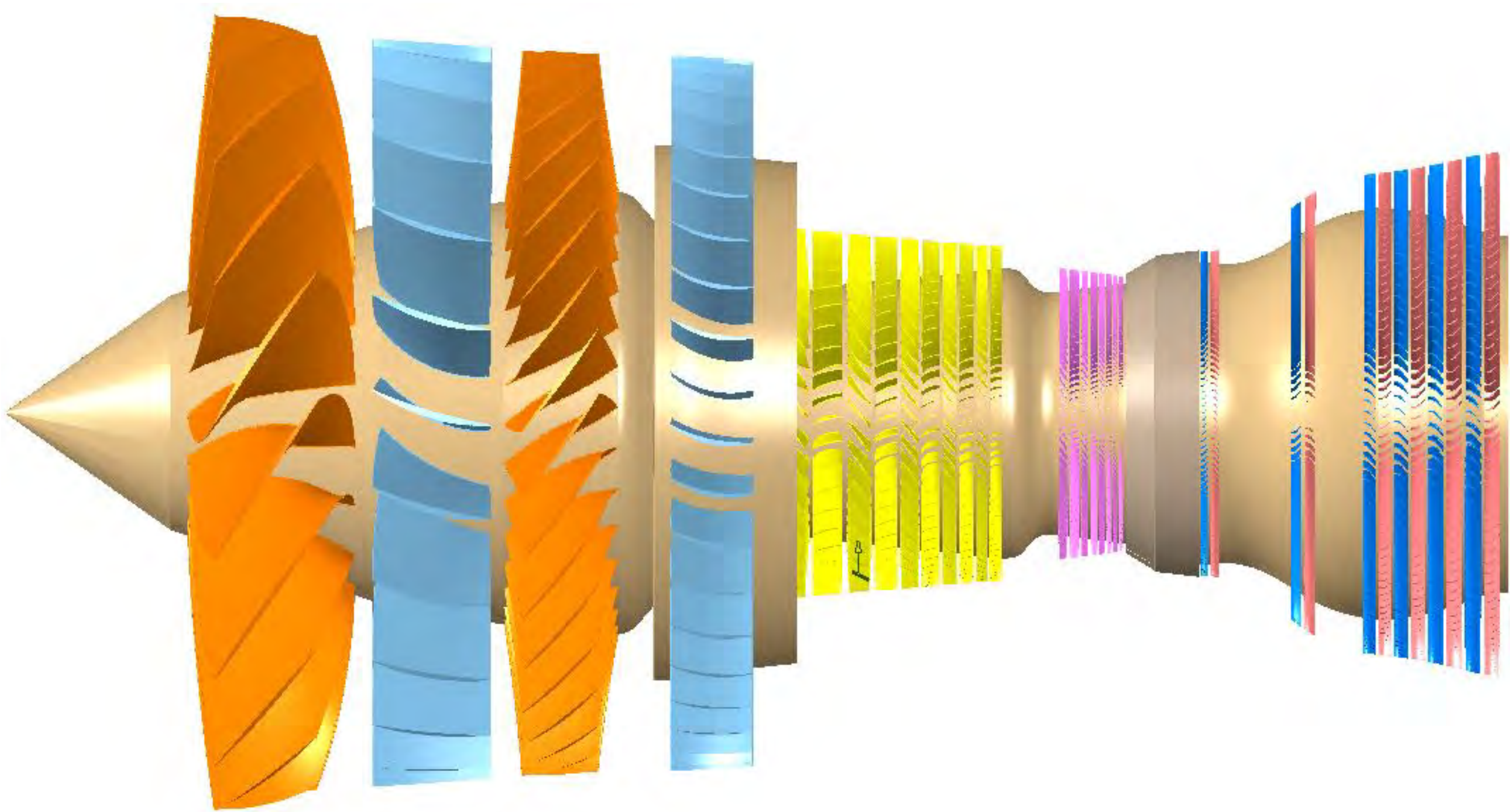

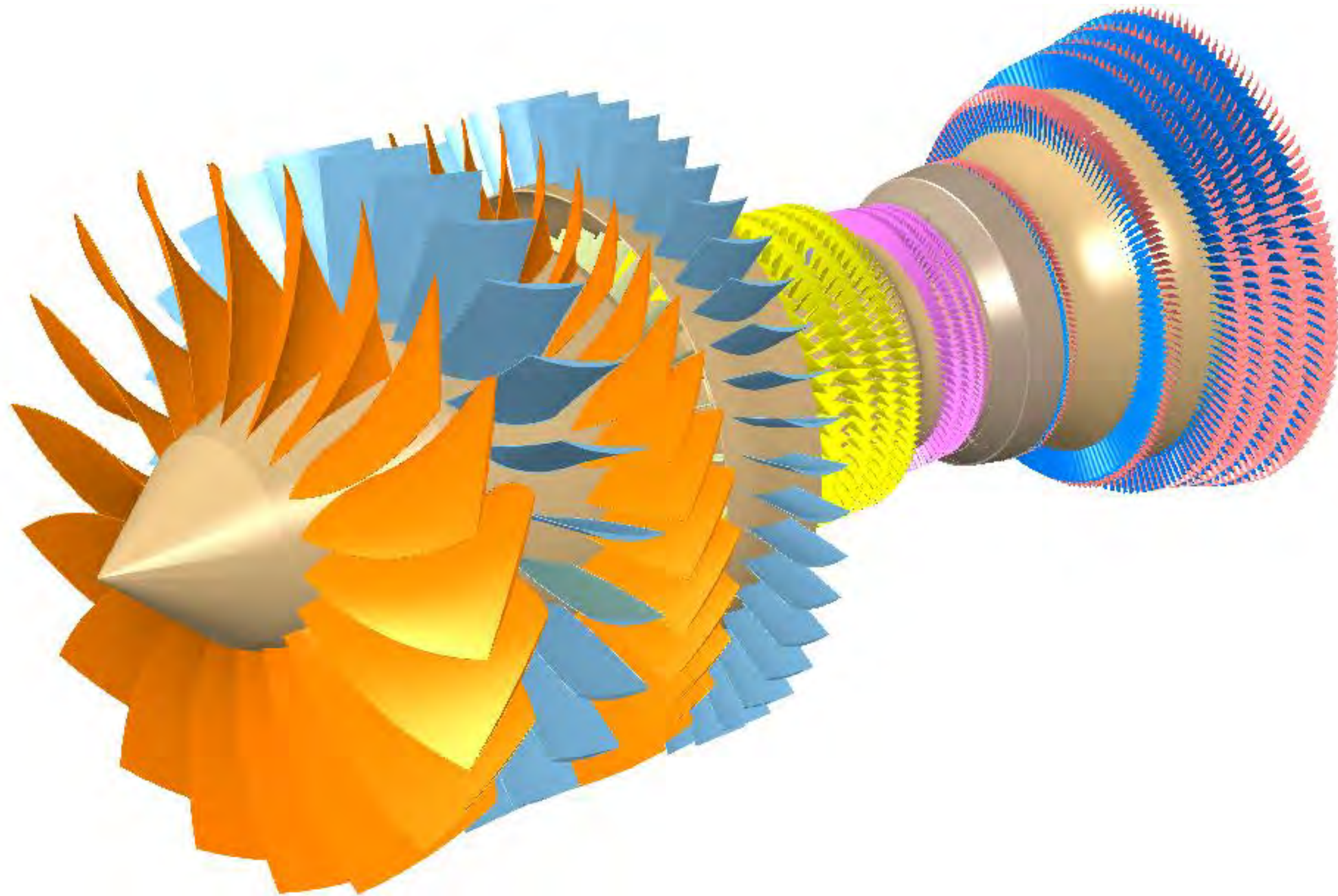Figure Appendix-B16 Horizontal View of Turbomachinery 3D model

Figure Appendix-B17 Isometric View of Turbomachinery 3D model

Appendix C –Detailed Design Output of Component Structure

Appendix C.1 Service Status of Advanced Materials

Table Appendix-C1 Material Properties of Advanced Materials

Engine Model	Material System	Application Area	Effect
M88-2	SPECARBINOX® A262 Cf/Sic Composites	External Regulation Film	Started batch production in 2002, and achieved the first application of ceramic matrix composites on engines in the world.
F110	SiCf/SiC	Adjustment Blade	Cumulative work time 500h, 1200°C / 100h, increased thrust 35%. Sampling performance Test results show no significant damage to SiCf/SiC
XTC76/3	SiCf/SiC	Combustion Chamber	Flame cartridge wall can withstand 1589K temperature
XTE76/1	SiCf/SiC	Low Pressure Turbine Stator Blade	Increased strength and durability, significantly reduced cooling air requirements
Trent800	SiC Composite Material	Fan-Shaped Turbine Outer Ring	Significant savings in cooling capacity, higher operating temperatures, lower structural weight and longer service life
F136(fitted on F35)	CMC	Turbine 3rd Guide Blade	Temperature resistance up to 1200, weight only 1/3 of nickel alloy. Probably the first commercial application of ceramic-based composites on jet engine hot-end components
Trent	CMC	Caudal	As of January 2013, no heat or structural stress problems occurred after 73 hours of operation.
Leap-X[29]	CMC	Low Pressure Turbine Guide Vane	The mass is only 1/2 or even lighter than traditional materials, but it can withstand high temperatures above 1200°C without cooling and is easy to process
GEnx	TiAl Intermetallic Compounds	Low Pressure Turbine	The GEnxTM uses the latest materials and design processes to reduce weight, improve performance, and reduce maintenance costs
XTC16/1A	SiCf/Ti6Al4V	High-Pressure Compressor 3rd/4th Stage Integral Leaf Ring	IHPTET (The Integrated High Performance Turbine Engine Technology) plan
XTC-76 JTDE	SiCf/TMMC	Low-Pressure Shaft and Low-Pressure Turbofan	
GE 90	8551-7/ IM7 Composite Material	Fan Blades	
YF 120	Carbon Fiber Reinforced PMR-15 Composite Material	Fan Blades	
F 119 and F 1 35	Resin-Based Composite Materials		
M88-2	PMR-15 Resin Based Compound Material	External Engine Casing	The external engine of the M8 8-2 engine developed by SNECMA was completely made of PMR-15 resin based compound material, which greatly reduced the weight

Appendix C.2 Support Stiffness - Critical Speed Sensitivity:

The stiffness of each bearing has an important influence on the characteristics of the critical speed. Changing the stiffness of the bearing is an effective way to adjust the critical speed away from the frequency band gap. Before attempting to optimize the CJ3000's support stiffness combinations, the ability of eleven stiffness values to affect the critical speed of the system will be evaluated. During the evaluation process, each stiffness value will change individually, taking 1/2, 2 times, and 3 times the original value in turn. The percentage change in critical speed is used to measure the effect of changing stiffness.

The following is the data in a calculation process:

Table Appendix-C2 Sensitivity of critical speed to support stiffness

%	Critical Speed rad/s	Supporting 1#	Supporting 3#	Supporting 8#	Supporting 2#	Supporting 4#	Supporting 7#	Supporting 5#	Supporting 6#	Rigid Coupling Point 1#	Rigid Coupling Point 2#	Rigid Coupling Point 3#
1st	150.933	-18.7/12.6/15.1	-1.08/0.77/1.07	-9.65/0.32/0.37	-0.70/0.46/0.64	-0.41/0.47/0.73	-0.57/0.18/0.23	-0.07/0.03/0.04	-0.09/0.04/0.05	-0.09/0.08/0.11	-0.04/0.05/0.07	0/0/0
2nd	185.133	-1.36/5.45/10.3	-0.54/0.41/0.58	-17.1/27.7/39.3	-0.37/0.25/0.35	-0.01/0.02/0.02	-4.55/1.49/1.89	-0.26/0.11/0.14	-0.30/0.12/0.16	-0.02/0.02/0.03	0/0/0	-0.50/0.26/0.35
3rd	298.168	0.79/0.79/0.792	-0.05/0.02/0.02	-1.24/4.06/9.51	-1.60/0.75/0.99	-1.20/1.21/1.81	-20.7/19.0/19.3	-3.63/0.91/1.14	-4.43/1.01/1.26	-0.01/0.01/0.01	-0.07/0.07/0.11	-0.57/0.29/0.38
4th	357.202	-5.1/12.2/18.46	-7.19/4.99/6.57	-0.09/0.26/0.69	-3.61/2.38/3.23	-1.10/1.36/2.14	-0.13/6.72/12.3	-5.55/1.47/1.79	-6.35/1.62/1.95	-0.08/0.06/0.09	-0.09/0.10/0.15	-0.12/0.06/0.08
5th	422.874	7.98/10.5/14.15	-1.75/2.71/4.26	-1.09/3.01/7.31	0/0/0	-0.17/0.20/0.32	-0.83/5.67/19.4	-8.46/10.6/15.5	-8.91/12.7/18.8	-0.22/0.17/0.24	-0.30/0.33/0.51	-0.69/0.35/0.47
6th	593.983	-0.11/0.88/1.71	-4.34/5.53/8.19	-0.01/0.02/0.05	-13.5/20.3/28.9	-5.23/8.97/16.1	-0.07/0.23/0.77	-0.16/0.25/0.43	-0.17/0.32/0.60	-0.08/0.06/0.08	-0.03/0.03/0.04	-0.02/0.01/0.01
7th	799.478	-1.19/2.74/5.94	-3.87/9.42/19.0	-0.05/0.11/0.22	-0.35/1.87/8.30	-0.09/0.23/0.57	0/0/0	0/0/0	0/0/0	-0.01/0.01/0.01	-0.01/0.01/0.01	0/0/0
8th	1342.812	0.17/0.257/0.32	0/0/0	-0.49/0.97/1.9	-0.05/0.11/0.23	-0.08/0.13/0.22	-0.35/0.74/1.54	0.33/0.26/0.36	-0.32/0.29/0.42	-9.99/0.52/0.58	-6.82/3.08/3.56	-24.5/6.94/7.16
9th	1470.801	0.09/0.23/0.342	0/0/0	-0.11/0.25/0.57	0/0/0.01	-0.51/1.02/2.01	0/0/0	-0.04/0.03/0.04	-0.23/0.19/0.28	-7.55/25.2/31.9	-2.97/12.8/25.3	-1.45/26.9/32.1
10th	1945.882	6.41/6.41/6.414	0/0/0	0/0/0	0/0/0	0/0/0.01	0/0/0	-8.14/12.9/23.1	-6.37/10.6/19.2	-0.03/0.33/10.6	-0.01/0.04/0.19	-0.02/0.26/14.7

Backgrounds marked with dark color indicate high sensitivity data.

Appendix C.3 CJ3000 Calculation Model of Transfer Matrix Method

Note that the international standard unit is used in this section. Backgrounds marked with black color indicate meaningless data.
Substructure number correspondence:
10 - low-pressure rotor, 20 - internal-pressure compressor, 30 - high-pressure rotor, 40 - core machine casing, 50 - by-pass casing.
At the same time, different substructures are also represented by different colors in the column of Young's modulus E.

Table Appendix-C3 CJ3000 Calculation Model of Transfer Matrix Method

E(N/m2)	I (m4)	L (m)	m (kg)	Jp (kg·m2)	Support Stiffness (N/m)	Substructure Number	Unknown State Parameter Type (Number)	Boundary Condition (Number)	Material Selection	Station Name
1.40E+11	2.7	0.00000001	0	0	0	10	2	0	TMMC	Free End
1.40E+11	9.94E-02	0.6	627.9098891	159.192838	0	10	0	0	PC	Fan R1
1.40E+11	1.82E-02	0.37	86.47450111	0	0	10	0	0	TMMC	1.5
1.40E+11	0.25	0.39	534.8362018	188.045971	0	10	0	0	PC	Fan R2
2.15E+11	6.12E-03	0.218	84.74501109	0	5.40E+07	10	1	1	TMMC	Supporting 1#
2.15E+11	5.50E-04	1.006	30.08274945	0	0	10	0	0	TMMC	2.5
2.15E+11	2.79E-05	0.18	4.27532767	0	2.10E+07	10	1	1	TMMC	Supporting 3#
2.15E+11	1.46E-05	0.82	13.82985437	0	0	10	0	0	TMMC	4.5
2.15E+11	4.57E-05	0.522	21.1565534	0	0	10	0	0	TMMC	4.5
1.71E+11	2.20E-01	0.05	777.2152913	187.663524	2.50E+07	10	1	1	CMC/NS	Supporting 8#
1.57E+11	1.97E-01	0.16	285.9293204	75.3939248	0	10	0	0	PST-TA	LPT R3
1.56E+11	1.74E-01	0.074	248.5258495	59.784551	0	10	0	0	PST-TA	LPT R4
1.60E+11	1.74E-01	0.0000001	0	0	0	10	0	2	NS	Free End
1.60E+11	3.65E-03	0.00000001	0	0	0	20	2	0	TMMC	Free End
2.15E+11	2.98E-04	0.1	8.441288506	0	1.20E+07	20	1	1	TMMC	Supporting 2#
2.15E+11	3.41E-02	0.105	46.40459964	10.0850971	0	20	0	0	TMMC	IP R1
2.15E+11	2.17E-03	0.085	4.766140777	0	0	20	0	0	TMMC	1.5
2.15E+11	4.04E-02	0.075	32.35281917	3.75706311	0	20	0	0	TMMC	IP R2
2.15E+11	2.35E-03	0.068	4.287160194	0	0	20	0	0	TMMC	2.5
2.15E+11	4.56E-02	0.055	31.00002914	3.2170267	0	20	0	0	TMMC	IP R3
2.15E+11	2.30E-03	0.052	3.148398058	0	0	20	0	0	TMMC	3.5
2.15E+11	5.11E-02	0.042	37.99663507	3.75162015	2.10E+07	20	1	1	TMMC	IP R4
2.15E+11	2.59E-03	0.04	2.390169903	0	0	20	0	0	TMMC	4.5
2.15E+11	5.26E-02	0.036	24.68027913	3.13845874	0	20	0	0	TMMC	IP R5
2.15E+11	9.44E-04	0.028	7.596953883	0	1.30E+07	20	1	1	TMMC	Supporting 4#
2.15E+11	9.44E-04	0.053	2.728580097	0	0	20	0	0	TMMC	5.5
2.15E+11	2.67E-05	0.885	15.40076636	0	0	20	0	0	TMMC	5.5
1.60E+11	5.69E-04	0.06	7.60623207	0	0	20	0	0	NS	5.5
1.60E+11	5.69E-04	0.05	6.4	0	1.05E+07	20	1	1	NS	Supporting 7#
1.67E+11	1.82E-01	0.05	301.7069874	55.0728155	0	20	0	0	CMC	IPT R1
1.60E+11	3.49E-03	0.0000001	0	0	0	20	0	2	NS	Free End

1.60E+11	1.82E-02	0.00000001	0	0	0	30	2	0	TMMC	Free End
1.65E+11	2.43E-02	0.028	23.78283161	1.92992718	0	30	0	0	TMMC	HP R1
1.60E+11	1.07E-03	0.05	3.389	0	0	30	0	0	TMMC	1.5
1.61E+11	2.78E-02	0.02	31.76503252	3.50010922	4.20E+07	30	1	1	TMMC	HP R2
1.60E+11	8.62E-04	0.04	2.192	0	0	30	0	0	TMMC	2.5
1.64E+11	2.89E-02	0.016	40.72460194	3.64949709	0	30	0	0	CMC	HP R3
1.60E+11	1.73E-04	0.079	1.64331232	0	0	30	0	0	NS	3.5
1.60E+11	1.21E-04	0.104	5.75288343	0	0	30	0	0	NS	3.5
1.60E+11	1.74E-04	0.15	10.6733784	0	0	30	0	0	NS	3.5
1.60E+11	3.67E-04	0.04	4.554	0	0	30	0	0	NS	3.5
1.69E+11	7.08E-02	0.08	145.5626335	16.5648841	0	30	0	0	CMC	HPT R1
1.80E+11	1.74E-04	0.1	7	0	4.50E+07	30	1	1	NS	Supporting 6#
1.80E+11	6.98E-02	0.0000001	0	0	0	30	0	2	NS	Free End
1.38E+11	1.65E-02	0.00000001	0	0	0	40	2	0	TMMC	Free End
1.38E+11	1.65E-02	0.356	14.46326578	0	0	40	0	0	TMMC	1
2.15E+11	1.25E-01	0.563	87.14938072	0	1.90E+08	40	1	1	TMMC	Rigid Coupling Point 1#
2.15E+11	1.41E-02	0.127	22.40793131	0	1.30E+07	40	1	1	TMMC	Supporting 4#
2.15E+11	2.02E-02	0.204	37.86407767	0	4.00E+08	40	1	1	TMMC	Rigid Coupling Point 2#
1.80E+11	2.02E-02	0.065	59.52348763	0	4.20E+07	40	1	1	NS	Supporting 5#
2.96E+11	1.88E-03	0.276	6.300175175	0	0	40	0	0	CMC	High Pressure Compressor Casing
2.96E+11	5.00E-03	0.188	21.43564219	0	0	40	0	0	CMC	Combustion Chamber
1.60E+11	5.15E-03	0.166	85.9223301	0	4.50E+07	40	1	1	GH/CMC	Supporting 6#
1.60E+11	1.70E-01	0.168	100.4854369	0	1.05E+07	40	1	1	GH/CMC	Supporting 7#
1.60E+11	1.70E-01	0.21	40.1140973	0	0	40	0	0	TMMC/CMC	1.5
2.15E+11	1.97E-02	0.1	37.65860838	0	2.50E+07	40	1	1	TMMC/CMC	Supporting 8#
1.60E+11	5.35E-02	0.4	94.62642807	0	0	40	0	0	CMC	Low Pressure Turbine Casing
2.96E+11	5.15E-02	0.142	21.60194175	0	4.50E+08	40	1	1	CMC	Lobed Mixer
1.80E+11	1.91E-03	1.351	14.68861701	0	0	40	0	0	CMC	Tail Cone
1.38E+11	1.91E-03	0.0000001	0	0	0	40	0	2	NS	Free End
1.38E+11	5.08E-02	0.00000001	0	0	0	50	2	0	PC	Free End
1.38E+11	5.08E-02	1.417	144.2257856	0	0	50	0	0	PC	Fan Casing
2.15E+11	8.27E-02	0.684	95.0142233	0	5.40E+07	50	1	1	TMMC	Supporting 1#
2.15E+11	1.85E-02	0.095	88.00084951	0	1.20E+07	50	1	1	TMMC	Supporting 2#
2.15E+11	1.85E-02	0.356	187.5545024	0	1.90E+08	50	1	1	TMMC	Rigid Coupling Point 1#
1.38E+11	1.01E-01	0.334	64.59629733	0	0	50	0	0	PC	1.5

2.15E+11	9.21E-02	0.191	66.77740035	0	4.00E+08	50	1	1	TMMC	Rigid Coupling Point 2#
1.38E+11	5.57E-02	0.738	33.74827076	0	0	50	0	0	PC	1.5
1.38E+11	5.35E-02	0.138	24.3997392	0	0	50	0	0	PC	1.5
2.15E+11	3.53E-02	0.528	63.12463902	0	0	50	0	0	TMMC	1.5
1.38E+11	1.63E-01	0.182	9.558704517	0	0	50	0	0	PC	1.5
2.96E+11	4.55E-02	1.597	87.27597087	0	4.50E+08	50	1	1	PC/CMC	Rigid Coupling Point 3#
1.38E+11	3.45E-02	2.24	66.05223786	0	0	50	0	0	PC/CMC	Tail Nozzle
1.38E+11	3.45E-02	0.0000001	0	0	0	50	0	2	PC	Free End